INFRARED ABSORPTION SPECTROSCOPY OF CARBON MONOXIDE ON NICKEL FILMS: A LOW TEMPERATURE THERMAL DETECTION TECHNIQUE

Robert Brian Bailey
(Ph. D. thesis)

November 1978

Prepared for the U. S. Department of Energy
under Contract W-7405-ENG-48

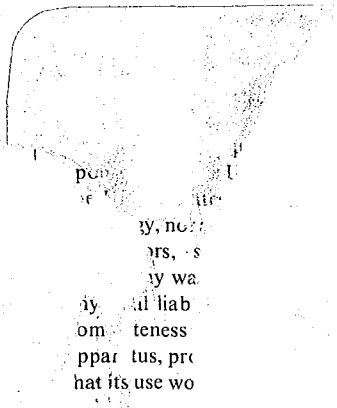

of wor
Neithe
artment
of their
ployees,
assumes
ccuracy,
mation;
presents
d rights.

INFRARED ABSORPTION SPECTROSCOPY OF CARBON MONOXIDE ON NICKEL FILMS: A LOW TEMPERATURE THERMAL DETECTION TECHNIQUE

Robert Brian Bailey

Materials and Molecular Research Division, Lawrence Berkeley Laboratory
and Department of Physics, University of California
Berkeley, California 94720

ABSTRACT

Sensitive vibrational spectra of carbon monoxide molecules adsorbed on evaporated nickel films have been measured by attaching a thermometer to the sample, cooling the assembly to liquid helium temperatures, and recording the temperature changes which occur when infrared radiation is absorbed. The measurements are made in an ultrahigh vacuum chamber in which the sample surface can be cleaned, heated, exposed to gas molecules and cooled to 1.6 K for the infrared measurements. The spectra of chemisorbed CO molecules are interpreted in terms of the linear and bridge adsorption sites on the nickel surface, and they show how the distribution of molecules among these sites changes when the CO coverage increases and intermolecular forces become important. The spectra of physically adsorbed molecules in both monolayer and multilayer films are also reported.

Absorptions as small as five parts in 10^5 of the incident radiation can presently be detected in spectra covering broad bands of infrared frequencies with a resolution of 2 cm^{-1}. This high sensitivity is attributable to the low noise and reduced background signal of the thermal detection scheme, to the stability of the rapid scan Fourier

transform infrared spectrometer, and to the automated computerized data acquisition electronics. Better performance is expected in future experiments on single crystal samples as well as evaporated films. This will make it possible to study molecules with weaker absorptions than CO and to look for evidence of chemical reactions between different adsorbed molecules.

Table of Contents

I. INTRODUCTION

The vibrational spectrum of a solid surface can reveal the identity and bonding configuration of adsorbed atoms and molecules. Recent experimental advances have made it possible to measure such spectra for single crystal samples. Electron energy loss spectroscopy[1] has detected surface vibrations over a broad range of energies with a resolution of approximately 10 meV (80 cm^{-1}). Infrared reflection spectroscopy[2-5] is capable of much higher spectral resolution, but its application has been limited to narrow regions of the vibrational spectrum. This thesis describes the development of a novel spectroscopic technique which achieves both the broad bandwidth of electron energy loss spectroscopy and the high resolution of infrared spectroscopy. A thermometer attached directly to the sample crystal measures the temperature changes which occur when infrared radiation is absorbed. Our initial measurements of carbon monoxide on evaporated nickel films demonstrate that the technique is sensitive enough to detect many different molecules and to study their properties in the adsorbed state.

A variety of experimental techniques have been used to study the interaction of gases with single crystal surfaces.[6] Photoemission spectroscopy, low energy electron diffraction, and Auger electron spectroscopy provide information on the structure and composition of the surface layer. Molecular beam techniques and mass spectroscopy have successfully monitored chemical reactions which occur at the surface. Work functions, heats of adsorption, and activation energies for diffusion, desorption, and bond formation are other important quantities

which can be measured. Of the available techniques, vibrational spectroscopy gives the most detailed information on chemical bonding. Surface spectra can be compared to the spectra of free molecules to determine what bonds are present and how they are changed by the adsorption process.

One of the earliest applications of infrared spectroscopy to surfaces was the work of Eischens,[7] who observed the transmission spectrum of carbon monoxide adsorbed on nickel samples chemically deposited on finely divided silica. High surface area metal samples of this type are used as catalysts in many industrial processes. Infrared spectroscopy is therefore an important technique for studying catalytic reactions, and this continues to be an active field of research.[8] The spectra however are often difficult to interpret. They depend not only on the metal and adsorbate being studied but also on the composition and structure of the supporting medium and other details of sample preparation. To eliminate the effects of the supporting medium and to avoid contamination, it is necessary to study single crystals or evaporated films under carefully controlled ultrahigh vacuum conditions.

A full monolayer of carbon monoxide, which has one of the strongest infrared active vibrational modes, absorbs only a few per cent of the incident infrared radiation at the peak of its resonance. Transmission spectra of supported metal samples rely on multiple reflections to build up a measurable signal. Multiple reflection geometries have been devised for evaporated films and metal foils with large surface

areas[9] but are not practical for single crystals whose surface areas are usually less than 1 cm^2. To study these samples it is necessary to detect small changes in the infrared power reflected from the surface. The lowest noise level achieved in experiments using reflection spectroscopy is approximately 0.02 per cent of the total incident power. These measurements scanned small regions of the infrared spectrum and employed either wavelength[4] or polarization modulation[5] to reduce the effects of fluctuations in the infrared beam. In only a few experiments have molecules other than carbon monoxide been detected.[4,9,10]

Energy loss spectroscopy (ELS) detects electrons scattered inelastically from the crystal surface. The energy lost by an electron is equal to the energy difference between vibrational states of the adsorbed molecule. Allowed vibrational excitations are governed by the same dipole selection rules which apply to infrared spectroscopy,[11,12] and only a small fraction of the incident electrons cause transitions. Since these inelastically scattered electrons differ in energy from the rest of the beam, they can be filtered out by the electron spectrometer and detected separately. The large background signals which occur in infrared reflection spectroscopy are therefore avoided.

Sensitive energy loss spectra have been reported for many molecules over the frequency range 300-4000 cm^{-1}.[12] One recent experiment detected an intermediate surface state in the dehydrogenation reaction of ethylene on a Ni(111) surface.[13] In addition to observing the internal vibrational modes of adsorbed molecules, ELS has detected the low frequency vibrations of the bonds linking the

molecule to the metal surface. These have not yet been seen in infrared experiments done in ultrahigh vacuum.

Although ELS has proved more sensitive than infrared spectroscopy, it has several limitations. One is that it cannot detect the high resolution features seen in an infrared spectrum. Another is that it cannot be used when the background pressure exceeds 10^{-3} torr because electron scattering by gas molecules then becomes important. Finally, the incident electron beam in ELS can induce changes in the surface layer.[14] These limitations provide an incentive for the development of more sensitive infrared and optical techniques for studying surfaces. Ellipsometry,[15] Raman scattering,[16] opto-acoustic spectroscopy,[17] and surface electromagnetic waves[18] have been mentioned as possibilities. Tunable laser sources also offer advantages; however, none are presently available which cover broad bands of infrared frequencies.

The infrared technique discussed in this thesis is called absorption spectroscopy since it detects only the fraction of the incident radiation which is absorbed by the sample and converted into thermal energy. For highly reflecting metal samples, absorption spectroscopy has the advantage that it does not detect the large reflected signal. It will therefore be less sensitive to fluctuations in the incident beam than reflection spectroscopy. Electron energy loss spectroscopy achieves the same advantage by detecting only the inelastically scattered electrons. Unfortunately, photons are not as surface sensitive as electrons. They penetrate hundreds of angstroms into a metal sample and interact with the conduction electrons. The result is an absorption spectrum with a broad background signal on top of

which appear the spectral lines from vibrational modes in the surface layer. Since the amplitude of the lines is the same as in the reflection spectrum, it is the size of the background signals detected in absorption and reflection spectroscopy which determines the relative sensitivity of the two techniques. For a noble metal like copper, the background signal in absorption spectroscopy can be as much as 20 times less than in reflection spectroscopy. For transition metals the advantage of absorption spectroscopy is significantly smaller especially at high frequencies where interband transitions occur.

Absorption spectra of solids have been measured using a variety of thermal detection techniques and infrared sources. When laser radiation is available, thermocouples are sensitive enough to detect the temperature changes.[19] In opto-acoustic spectroscopy[17] the thermal energy is converted into sound waves for detection by a microphone. The procedures which we use for sensing small temperature changes have been widely applied in the design of broad band radiation detectors called bolometers.[21,22] The principal requirements are a low heat capacity sample and a small thermal conductance linking the sample to its heat sink. Spectral measurements must be made at liquid helium temperatures in order to detect the small infrared absorptions from a monolayer of adsorbed molecules. A doped germanium resistance thermometer measures the sample temperature. Using similar low temperature techniques, Joyce and Richards[22] have measured the absorption spectrum of metal samples at far infrared frequencies.

The experiments described in Chapter V of this thesis clearly demonstrate the potential sensitivity of the low temperature thermal

detection scheme which we have developed. These measurements were made over a three week period after spending two and one half years designing, building, and optimizing the equipment. Our principal accomplishment has been to demonstrate that a practical spectroscopic system of this type can be built and that its sensitivity is adequate to study single crystal surfaces. Most of the thesis therefore focuses on experimental details. The contents of each chapter are briefly summarized in the following paragraphs.

In Chapter II we present a simple model for calculating the infrared absorption of a metal surface covered by a thin layer of molecules. The metal is treated as a homogeneous medium, and only dipole-dipole interactions between molecules are included. Such a model does not account for the complex chemical effects which are observed in an infrared spectrum. It does predict the approximate magnitudes of the absorption signals and determines the optimum experimental conditions for absorption spectroscopy.

Chapter III describes the vacuum system, thermal detection scheme, infrared spectrometer, and data acquisition electronics which we use to measure absorption spectra of surfaces. The sample crystal is maintained at a temperature of 1.6 K by a liquid helium cryostat. The bakeable sample chamber has a base pressure of approximately 10^{-10} torr and includes facilities for cleaning and heating the sample crystal, evaporating metal films, and making controlled gas exposures. It does not include any means for characterizing the surface other than the infrared technique being developed. The infrared beam is

incident on the sample from a rapid scan Fourier transform spectrometer. A mini-computer controls the data acquisition process, performs the Fourier analysis, and calculates spectral differences to isolate surface effects.

Chapter IV presents a detailed quantitative analysis of the performance of the system. Our best measurements have been made on evaporated nickel films samples at frequencies between 1000 cm^{-1} and 3000 cm^{-1} with a resolution of 2 cm^{-1}. The lowest rms noise levels on the spectra are equivalent to an absorption of 13 parts per million of the incident infrared power. We show that elimination of excess noise from the spectrometer, data acquisition electronics, and thermometer crystal will improve the performance by a factor of ten. Our calculations also show that comparable sensitivities can be achieved for single crystal samples with hundreds of times the heat capacity of the nickel films presently being studied. The analysis indicates that sensitive spectra can also be measured at lower infrared frequencies where much less power is available from the infrared source.

The results of our first experiments are presented in Chapter V. The data show the effects of systematically varying the temperature of an evaporated nickel film following exposure to carbon monoxide gas. Distinct absorption lines are detected for the CO molecules chemically bonded to one, two, and three nickel atoms on the film surface. The spectra show how the distribution of molecules among these adsorption sites changes when the surface coverage increases and intermolecular forces become important. Several distinct bonding configurations are

also detected in the spectra of monolayer films of physically adsorbed carbon monoxide which are stable on a surface only at low temperatures. For multilayer CO films we see evidence of a new low temperature crystal phase with very narrow infrared linewidths. These measurements demonstrate that surface states formed over a broad range of temperatures can be conveniently studied using our low temperature techniques and that precise control of the sample temperature allows us to measure activation energies for chemical and physical changes. Future experiments will focus on single crystal samples, on molecules other than carbon monoxide, and on the detection of vibrational modes at lower frequencies where the absorption technique has its greatest advantages.

II. INFRARED ABSORPTION BY SURFACE LAYERS

The oscillating dipole moment of a vibrating molecule interacts with the electric field of an incident plane wave and causes the infrared absorption which we detect in our experiment. In many cases this moment is only weakly perturbed when the molecule is adsorbed on a metal surface. It should then be possible to accurately calculate the absorption spectrum from the measured properties of the free molecule and of the clean metal surface. These calculations tell us what angles of incidence make the surface absorption signals most prominent and what signal to noise ratio is necessary to detect the presence of a given molecule. By comparing the magnitude of the calculated effects in the absorption and reflection spectra, we can predict the relative advantages of the absorption technique described in this work compared with conventional reflection spectroscopy.

Greenler[23] has shown that infrared absorptions on a metal surface are maximized when the radiation is incident at nearly grazing angles. He modeled the adsorbed molecules as a continuous dielectric film and solved Maxwell's equations to calculate the reflected and absorbed power. The results and applications of the thin film model are discussed in a recent review by McIntyre.[24] In our application we derive the dielectric constant of the surface layer from a simple dipole model of the adsorbed molecules. To properly account for dipole-dipole interactions in a monolayer film, we replace the standard Lorentz correction[29] to the local electric field with a direct sum of the dipole fields from all occupied lattice sites on the surface.

A. Dipole Model for Carbon Monoxide

Vibrational transitions in carbon monoxide gas are accompanied by changes in the rotational state of the molecule. The resulting infrared spectrum contains hundreds of sharp absorption lines. Free rotation does not occur when the molecules are bonded to a metal surface or condensed in the solid phase at low temperatures.[25] In our experiment we therefore expect a single absorption line associated with transitions to the first excited vibrational state, and we can use a simple harmonic oscillator model to predict the infrared absorption.

To characterize the vibrational mode of the oscillator, we need only know its resonant frequency ν_o, linewidth $\Delta\nu$, reduced mass μ, and effective charge q. For the free carbon-oxygen vibration, μ = 6.86 proton masses and ν_o = 2143 cm^{-1}. The observed linewidth varies from 50 cm^{-1} for carbon monoxide with a strong chemical bond to a metal surface to less than 1 cm^{-1} for a thick layer of molecules crystallized into a well ordered lattice. An expression for the molecule's dipole moment, deduced from measurements of the gas phase spectrum,[26] is $p = p_o + q\,\Delta r$ where p_o is -0.112×10^{-18} esu-cm, $q = 3.1 \times 10^{-10}$ esu, and Δr is the displacement of the interatomic distance from its equilibrium value of 1.13×10^{-8} cm.

If the electric field at the site of a molecule is $\vec{E}(t) = E\, e^{-i\omega t}$, then the induced dipole moment has the same time dependence and an amplitude $p = \alpha(\omega)E$ where the complex polarizability is[27]

$$\alpha(\omega) = \frac{q^2/\mu}{(\omega_o^2 - \omega^2) - i\omega\Delta\omega} + \alpha_E = \alpha'(\omega) + i\alpha''(\omega)\,. \qquad (1)$$

In this formula $\omega = 2\pi c\nu$ and $\Delta\omega = 2\pi c\,\Delta\nu$ where ν and $\Delta\nu$ are expressed in cm^{-1}. The contribution α_E is a real constant arising from the polarizability of the electrons in the molecule which have their resonances at visible and ultraviolet frequencies. The measured optical index of refraction for CO gas yields a value $\alpha_E = 2 \times 10^{-24}\ cm^3$.

The power absorbed by a single molecule is the product of its absorption cross section $\sigma(\omega)$ and the incident infrared power per unit area. The cross section is[27]

$$\sigma(\omega) = 4\pi \frac{\omega}{c} \alpha''(\omega).$$

It has a peak value at resonance of

$$\sigma(\omega_o) = \frac{2q^2}{\mu c^2 \Delta\nu} = \frac{1.95 \times 10^{-17}}{\Delta\nu}\ cm^2 .$$

The vibrational polarizability is significant only for electric fields parallel to the axis of the molecule. For randomly oriented molecules this means that one third of all the dipole moments are active in the absorption process. To illustrate the strength of the carbon monoxide absorption, we consider a layer of N_A molecules per unit area adsorbed on the surface of a transparent substrate. Radiation of frequency ω_o is incident at an angle ϕ to the surface normal. The layer absorbs a fraction $N_A\sigma(\omega_o)/3\cos\phi$ of the total incident power. For $\phi = 80°$, $\Delta\nu = 6\ cm^{-1}$ and for a single layer of molecules with $N_A = 7.6 \times 10^{14}/cm^2$, we calculate a fractional absorption of 0.5 per cent. This estimate assumes that the fields in the surface layer are those of the incident plane wave alone. To

improve the accuracy of the calculation we must include the effects of electric fields from dipole moments induced in the substrate and in neighboring molecules in the surface layer.

B. Dielectric Constant of the Surface Layer

To accurately calculate the infrared absorption of our sample we must treat the molecules on the surface as discrete dipoles rather than as a continuous dielectric film. Born and Wolfe[28] discuss the propagation of electromagnetic waves in such a medium. The total electric field is the sum of the fields from external sources and those produced by the individual dipoles. The polarizability α relates the dipole moment of a molecule to the local value of the electric field. The basic equations of this microscopic theory are obtained by requiring that the fields and moments within the medium be self-consistent.

For an electromagnetic wave incident on a polarizable medium from vacuum, the microscopic theory yields a reflection coefficient[28] which is equivalent to the one derived from Maxwell's equations for two homogeneous media. This is because the reflected field is evaluated far from the interface where it depends only upon the spatially averaged properties of the medium. For the same reasons we should be able to use the solution of Maxwell's equations for the thin film geometry of Fig. 1 to calculate the reflection coefficient of a metal surface covered by a layer of adsorbed molecules. The self-consistency requirement of the microscopic theory must be imposed to find the relationship between the average polarization P and the average

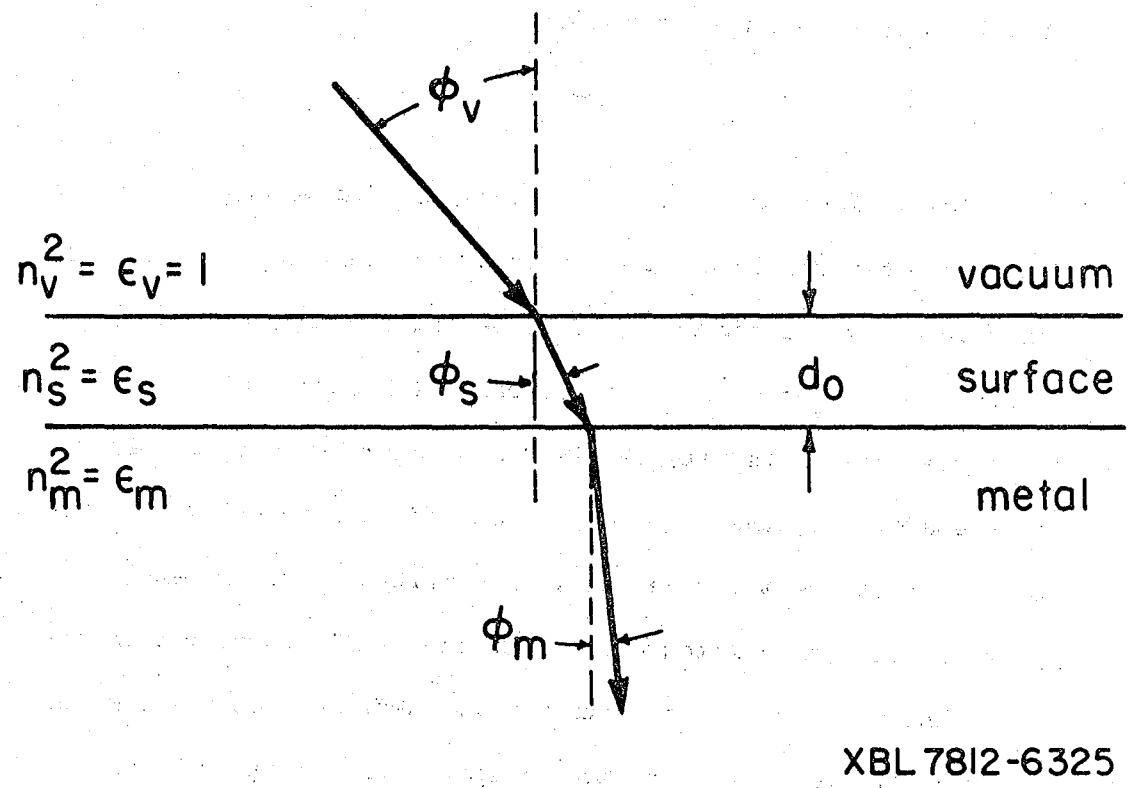

Fig. 1. Thin film surface geometry.

electric field E within the surface layer. This determines the effective dielectric constant of the molecules

$$\epsilon_s = 1 + 4\pi P/E. \tag{2}$$

The local electric field E_L at the site of a molecule is found by adding the externally applied field E_A to the total dipole field E_D contributed by all the other molecules in the medium. For bulk materials[29] molecules within a spherical shell surrounding the lattice site are treated as discrete dipoles, and their individual electric fields are added together. Molecules outside the sphere are assumed to form a continuous polarization with density P, and the electric field is calculated by integrating over the remaining volume of the crystal. The integral has a contribution $4\pi P/3$, called the Lorentz field, from the inside surface of the spherical cavity. The outer surface of the medium also contributes to the dipole field. For the thin film pictured in Fig. 1 and polarized perpendicular to its surface, the field is $-4\pi P$. The total local field is then

$$E_L = E_A + E_C + 4\pi P/3 - 4\pi P = E + E_C + 4\pi P/3$$

where E_C is the field from molecules within the spherical cavity, and $E = E_A - 4\pi P$ is the average field which appears in Maxwell's equations. The term E_C depends upon the lattice structure of a solid medium and vanishes for sites of cubic symmetry.

When the film consists of a single layer of adsorbed molecules, it cannot be treated as a continuous medium and E_D must be calculated by summing individual fields from all the surface dipoles. Two

dimensional lattice sums of this type have been used to estimate the heat of adsorption of molecules[30] and the work function change caused by adsorbed monolayers.[31] The results for square arrays and hexagonal arrays differ by only a few per cent. We perform the calculation for a square array of surface dipoles and consider only the electric field components perpendicular to the surface. Parallel fields are effectively canceled by the response of the conduction electrons of the metal substrate.

The real surface consists of an array of adsorption sites with lattice constant d_o. A fraction θ of the sites are occupied by adsorbed molecules. We model this surface as a square array of occupied sites with lattice constant $d_o/\sqrt{\theta}$. We use d_o as the thickness of the film in Fig. 1 and now proceed to derive the appropriate dielectric constant ε_s.

If p is the dipole moment of a single molecule, then there will be an image dipole p' induced in the metal substrate a distance d_o from each source dipole. Its magnitude is[32]

$$p' = \frac{\varepsilon_m - 1}{\varepsilon_m + 1} p,$$

if we use a continuum model for the response of the metal. Since $|\varepsilon_m| >> 1$ for good conductors at infrared frequencies we can assume $p' = p$.

The electric field at position $\vec{r} = 0$ produced by a dipole $\vec{p}$ at position $\vec{r}$ is

$$\vec{E} = \frac{3\hat{r}(\vec{p}\cdot\hat{r}) - \vec{p}}{|\vec{r}^3|} .$$

For dipoles oriented perpendicular to the surface we find the total fields for the array of source and image dipoles to be

$$E_{source} = -\frac{p}{(d_o/\sqrt{\theta})^3} \sum_{i,j\neq 0} \frac{1}{(i^2+j^2)^{3/2}} = -\frac{p\theta^{3/2}}{d_o^3} A$$

$$E_{image} = \frac{p}{(d_o/\sqrt{\theta})^3} \sum_{i,j} \frac{2\theta - i^2 - j^2}{(\theta + i^2 + j^2)^{5/2}} = \frac{p\theta^{3/2}}{d_o^3} B(\theta) .$$

Cutting off the series at 200 lattice constants, a computer calculation yields A = 9.005 and B(θ=1) = 0.113. The value of A agrees with the published result 9.035 for the infinite sum.[33] The infrared wavelengths of interest in vibrational spectroscopy are typically 10^4 lattice constants. The convergence of the lattice sums in a small fraction of this distance justifies the neglect of retardation effects in evaluating the dipole field from distant molecules.

The local field at each site in the surface layer is

$$E_L = E_A + \frac{p\theta^{3/2}}{d_o^3} [B(\theta)-A] = E + 4\pi P + \theta^{1/2} P[B(\theta)-A] \qquad (3)$$

where we have defined an average polarization density $P = p\theta/d_o^3$ and again used the relation $E = E_A - 4\pi P$ between the externally applied field E_A and the average field E within the surface layer. Self consistency between the fields and polarizations is achieved if we combine Eq. (3) with the defining relation for the molecular polarizability $p = \alpha E_L$ to obtain

$$P = \theta N_V \alpha E_L = \theta N_V \alpha [E + C(\theta)P] \tag{4}$$

where $N_V = 1/d_o^3$. The quantity

$$C(\theta) = 4\pi + \theta^{1/2} [B(\theta) - A] \tag{5}$$

determines the magnitude of the local field correction. Using Eq. (2), the self consistent dielectric constant is

$$\varepsilon_s(\theta) = 1 + 4\pi \frac{N_V \alpha \theta}{1 - N_V \alpha \theta C(\theta)} \tag{6}$$

We have focussed upon the problem of deriving an effective surface layer dielectric constant to be used with Maxwell's equations in calculating the reflection coefficient for the thin film goemetry pictured in Fig. 1. Sivukhin[34] obtains the amplitude of the reflected wave more directly by summing the scattered waves from individual molecules in the surface layer. His theory takes into account the lattice structure of the substrate as well as the surface layer, so it is potentially more accurate than our model which assumes a homogeneous substrate. Because Sivukhin's results are complicated, and his paper is in Russian, we have not attempted to use it in calculating infrared absorptions. However Bootsma[35] has compared Sivukhin's predictions for the phase shifts observed in optical ellipsometry with calculations based upon Maxwell's equations. The two approaches give very similar results for the coverage dependence of the phase shift, and the experimental data are not accurate enough to distinguish between them.

C. Optical Constants of Metals

The optical properties of a metal sample determine the surface sensitivity of infrared absorption spectroscopy. For metals with large infrared absorptions it is more difficult to detect the small signals contributed by molecules on the surface. At the high angles of incidence which maximize the surface sensitivity, the absorption coefficients of different metals range from 5 to 50 per cent and depend upon the frequency of the radiation and the temperature of the sample. In this section we consider the published measurements of the infrared optical constants of nickel and copper and use a free electron model to estimate the changes which occur when the sample is cooled to liquid helium temperature.

If we include a phenomenological scattering time τ for each electron, the standard result for the frequency dependent dielectric function of a free electron gas is[36]

$$\varepsilon_m(\omega) = 1 + \frac{4\pi i}{\omega}\left(\frac{\sigma_o}{1 - i\omega\tau}\right) \qquad (7)$$

where $\sigma_o = Ne^2\tau/m$ is the electrical conductivity, N is the number of electrons per unit volume, and m is the effective mass of the electrons. The value of σ_o deduced from optical and infrared measurements is generally less than the measured DC electrical conductivity. This is because optical measurements preferentially sample the disordered surface layers of a metal and also because photons cause interband transitions. It is generally found however that the best DC electrical conductors exhibit the lowest infrared absorption. The noble metals

copper, silver, and gold are therefore better prospects for absorption spectroscopy than transition metals such as nickel and platinum. The scattering time τ is the temperature dependent parameter in Eq. (7). At room temperature it is limited by electron-phonon collisions. At low temperatures phonon scattering becomes negligible; the conductivity increases, and we expect less absorption at infrared frequencies.

Two measurements[37,38] of the index of refraction $n_m = \sqrt{\epsilon_m}$ of evaporated nickel films have been reported in the infrared frequency range between 800 cm^{-1} and 5000 cm^{-1}. Both show substantial deviations from the free electron model. Beattie's results fit Eq. (7) fairly well below 1200 cm^{-1}, and here the expected increase in absorption due to phonon scattering is observed at elevated temperatures. From this low frequency data the free electron parameters are found to be $\sigma_o = 3.16 \times 10^{16}$ esu and $\tau = 1.02 \times 10^{-14}$ sec at room temperature. Above 2500 cm^{-1} the measured index of refraction is only weakly temperature dependent and indicates the presence of an additional absorption probably caused by interband transitions. Only the relatively small free electron contribution to the measured high frequency absorption is expected to decrease with temperature.

At infrared frequencies the mean free path of an electron in nickel at room temperature is 150 Å if we assume a Fermi velocity of 1.5×10^8 cm/sec and use Beattie's value for the scattering time. At very low temperatures phonon and electron scattering are no longer important, and the electron mean free path is determined by other scattering mechanisms. In polycrystalline evaporated films defects and grain

boundaries can limit the mean free path, and the optical constants are sometimes observed to vary with the conditions of evaporation. For annealed single crystals we expect the mean free path to be limited by more fundamental processes. When the mean free path becomes much greater than the penetration depth of radiation into the metal, scattering of electrons from the surface can become the dominant loss mechanism. The theory of the anomolous skin effect applies in this limit.[39] If surface scattering is inelastic, then the effective mean free path is approximately equal to the penetration depth δ which is given by[40]

$$\frac{1}{\delta} = \text{Im}\left[2\frac{\omega}{c}\sqrt{\varepsilon_m(\omega)}\right] .$$

At 1000 cm^{-1} using the free electron parameters for nickel, we find δ = 260 Å.

Another loss mechanism, predicted by Holstein,[41] involves the absorption of a photon and emission of a phonon by the scattered electron. The scattering time τ_H for this process is

$$\tau_H = \frac{5T\tau}{2\theta}$$

where τ is the electron-phonon scattering time measured at a temperature T greater than the Debye temperature θ. Using Beattie's measured value $\tau = 0.72 \times 10^{-14}$ sec at T = 520 K and using θ = 450 K for nickel we find $\tau_H = 2.1 \times 10^{-14}$ sec, so the mean free path is 315 Å. Surface scattering and the Holstein mechanism give similar scattering lengths which are approximately twice the measured room temperature mean free path. We

therefore expect no more than a factor of two increase in the optical conductivity and time constant when we cool a nickel sample.

Table 1 compares the measured room temperature complex index of refraction for nickel and copper with the expected low temperature values. The room temperature data are from Beattie's published measurements. The low temperature values assume a factor of two increase in σ_o and τ for the free electron contribution to the dielectric constant. To calculate nickel's low temperature index of refraction at 2000 cm^{-1} and 4000 cm^{-1} in the presence of temperature independent interband absorptions, we have separated the interband contribution to the dielectric function from the free electron contribution and corrected only the free electron part. Measured interband absorptions in copper are much smaller than for nickel. A free electron model with $\sigma_o = 1.54 \times 10^{17}$ esu and $\tau = 1.41 \times 10^{-14}$ sec was found by Beattie to be accurate at all four frequencies listed in Table 1.

D. Numerical Results

The electric field of the plane wave reflected from the interface pictured in Fig. 1 has an amplitude

$$r = \frac{r_{vs} + r_{sm} e^{2i\beta}}{1 + r_{vs} r_{sm} e^{2i\beta}} \tag{8}$$

relative to the incident amplitude.[42] The phase change across the surface layer for infrared wavelength λ is

$$\beta = 2\pi n_s \frac{d_o}{\lambda} \cos \phi_s .$$

Table 1. Index of Refraction of Metals

Nickel	500 cm^{-1}	1000 cm^{-1}	2000 cm^{-1}	4000 cm^{-1}
Warm	22 + 51i	7.6 + 29i	5.0 + 16i	3.6 + 9.0i
Cold	15 + 65i	4.3 + 33i	4.0 + 16i	3.4 + 9.0i
Copper				
Warm	36 + 106i	11 + 59i	2.9 + 31i	.77 + 16i
Cold	22 + 118i	5.8 + 61i	1.5 + 31i	.47 + 16i

The Fresnel coefficients r_{ij} give the reflected amplitude for the single interface between media i and j. For the polarization states parallel and perpendicular to the plane of incidence their values are

$$r_{ij}^{\parallel} = \frac{n_j \cos \phi_i - n_i \cos \phi_j}{n_j \cos \phi_i + n_i \cos \phi_j}$$

$$r_{ij}^{\perp} = \frac{n_i \cos \phi_i - n_j \cos \phi_j}{n_i \cos \phi_i + n_j \cos \phi_j}$$

where the angles ϕ_i are related by Snell's law

$$n_i \sin \phi_i = n_j \sin \phi_j \ .$$

Since no power is transmitted through the metal, the total absorption by the interface is $A = 1 - |r|^2$. We must evaluate A for different values of ϕ_v, n_s, and n_m in order to predict the power absorbed by our sample. The surface layer index of refraction n_s is calculated from the dielectric constant of Eq. (6) for different surface coverages θ and polarizabilities α. The polarizability α is given by Eq. (1) and is a function of the infrared frequencies ν and ν_o and the linewidth $\Delta\nu$. For absorbing media all the expressions involve complex numbers, and their forms reveal very little about the qualitative dependence of the absorption signal on the variables ϕ_v, n_m, θ, ν, ν_o, and $\Delta\nu$. We have done numerical calculations on a computer, and in this section we discuss the results.

The angular dependence of the metallic absorption is shown in Fig. 2a for a cold nickel sample using the index of refraction from Table 1 for $\nu = 2000$ cm^{-1}. The bulk absorption by the metal is given

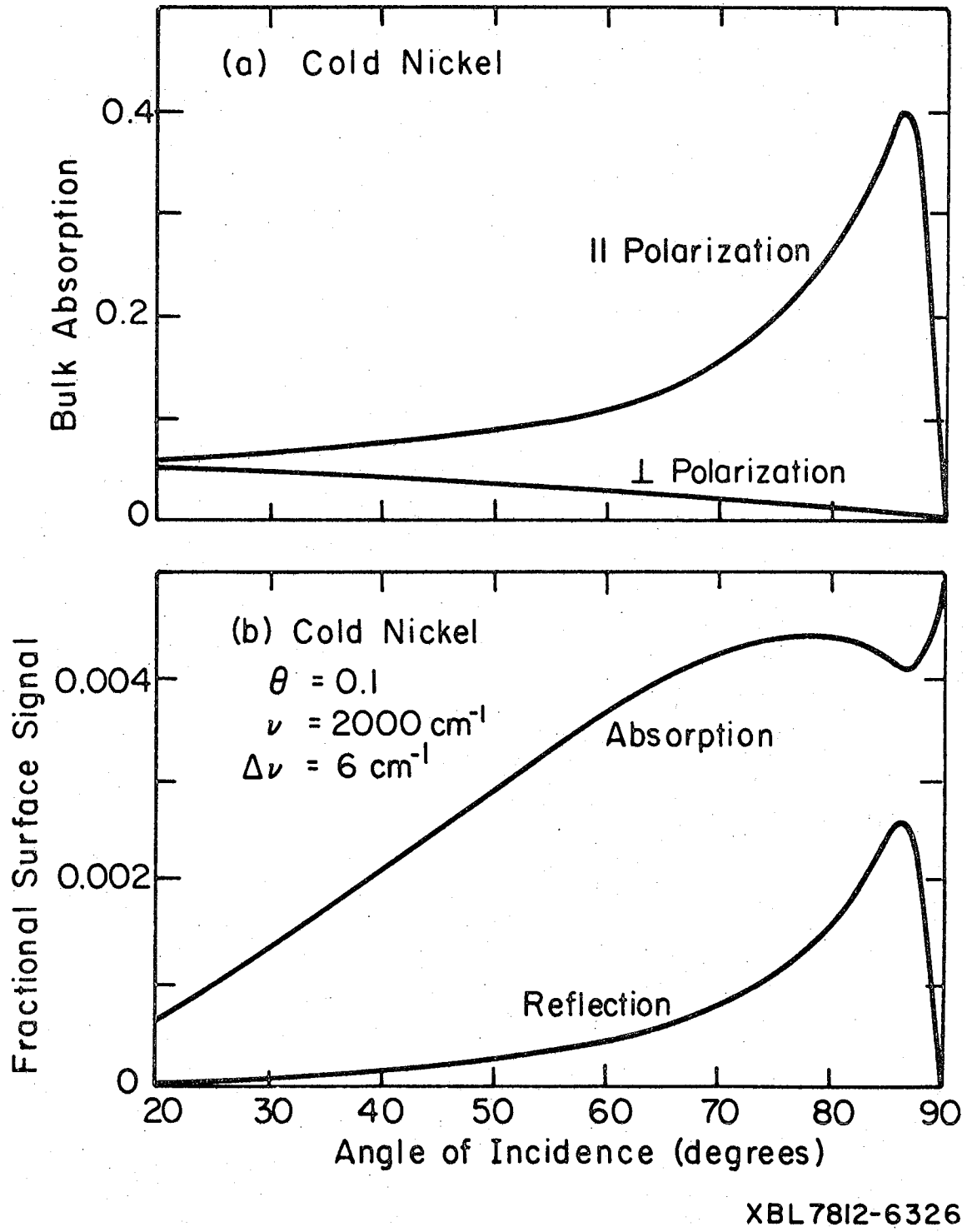

Fig. 2. Bulk and surface signal vs. angle of incidence.

as a fraction of the total incident power. Relatively little absorption occurs for radiation polarized perpendicular to the plane of incidence because for this case the incident electric field is parallel to the metal surface. The electrons in the metal respond to cancel such a field, and in the process they radiate a reflected wave of nearly equal amplitude and opposite phase. The result is a standing wave pattern with a minimum in the electric field amplitude at the position of the surface. Because the field is small, there can be very little absorption in the surface layer. Molecular dipoles oriented parallel to the surface are therefore difficult to detect using infrared spectroscopy.

For radiation polarized parallel to the plane of incidence, there is an electric field component normal to the metal surface which is not canceled by the conduction electrons. At large angles of incidence this field interacts strongly with both the metal and surface layer producing a maximum in the absorption by both media for angles between 85° and 90°. Below we consider only this parallel polarization component since effects from radiation polarized perpendicular to the plane of incidence are two to three orders of magnitude smaller.

The surface signal shown in Fig. 2b is for 0.1 monolayer of randomly oriented molecules with the dipole parameters q and μ of carbon monoxide and a resonant frequency $\nu_o = 2000\ cm^{-1}$. In calculating the index of refraction $n_s = \sqrt{\varepsilon_s}$ from Eq. (6), we use the measured density of solid carbon monoxide $N_V = 2.2 \times 10^{22}$ molecules/cm^3. We assume a linewidth $\Delta\nu = 6\ cm^{-1}$ to calculate the polarizability from Eq. (1). The surface signal is taken as the difference between the reflection coefficients

calculated for the two frequencies $\nu = \nu_o$ and $\nu = \nu_o + 10\ \Delta\nu$. In Fig. 2b, this quantity is ratioed to the total absorbed power and to the total reflected power to predict the fractional signal change we expect to observe in absorption and reflection spectroscopy due to the dipole resonance at frequency ν_o. For optimum sensitivity reflection spectroscopy must use a high angle of incidence. For the nickel surface at 2000 cm^{-1}, absorption spectroscopy sees twice the fractional signal and can use a broader range of angles.

Figure 3 shows that absorption spectroscopy achieves a larger advantage over reflection spectroscopy for infrared frequencies below 2000 cm^{-1} where the interband absorption by bulk nickel is reduced. The surface signal in Fig. 3b is for a molecule identical to carbon monoxide except for the frequency of its infrared resonance. The fractional absorption signal increases as the bulk absorption drops. For the cold nickel sample it is roughly six times the corresponding reflection signal at 1000 cm^{-1}. For a free electron metal like copper, an advantage of approximately 20 is achieved over the entire infrared spectrum if we use the dielectric constants in Table 1 for a cold sample. In all cases the surface absorptions are a small fraction of the total sample absorption. For a molecule with one tenth the dipole strength of CO and a linewidth of 60 cm^{-1}, we expect fractional absorption signals 100 times smaller than those of Fig. 3b. Detection of 0.1 monolayer of such a molecule on a nickel surface requires a signal-to-noise ratio on the measured absorption spectrum of between 10^4 and 10^5 depending on the infrared frequency.

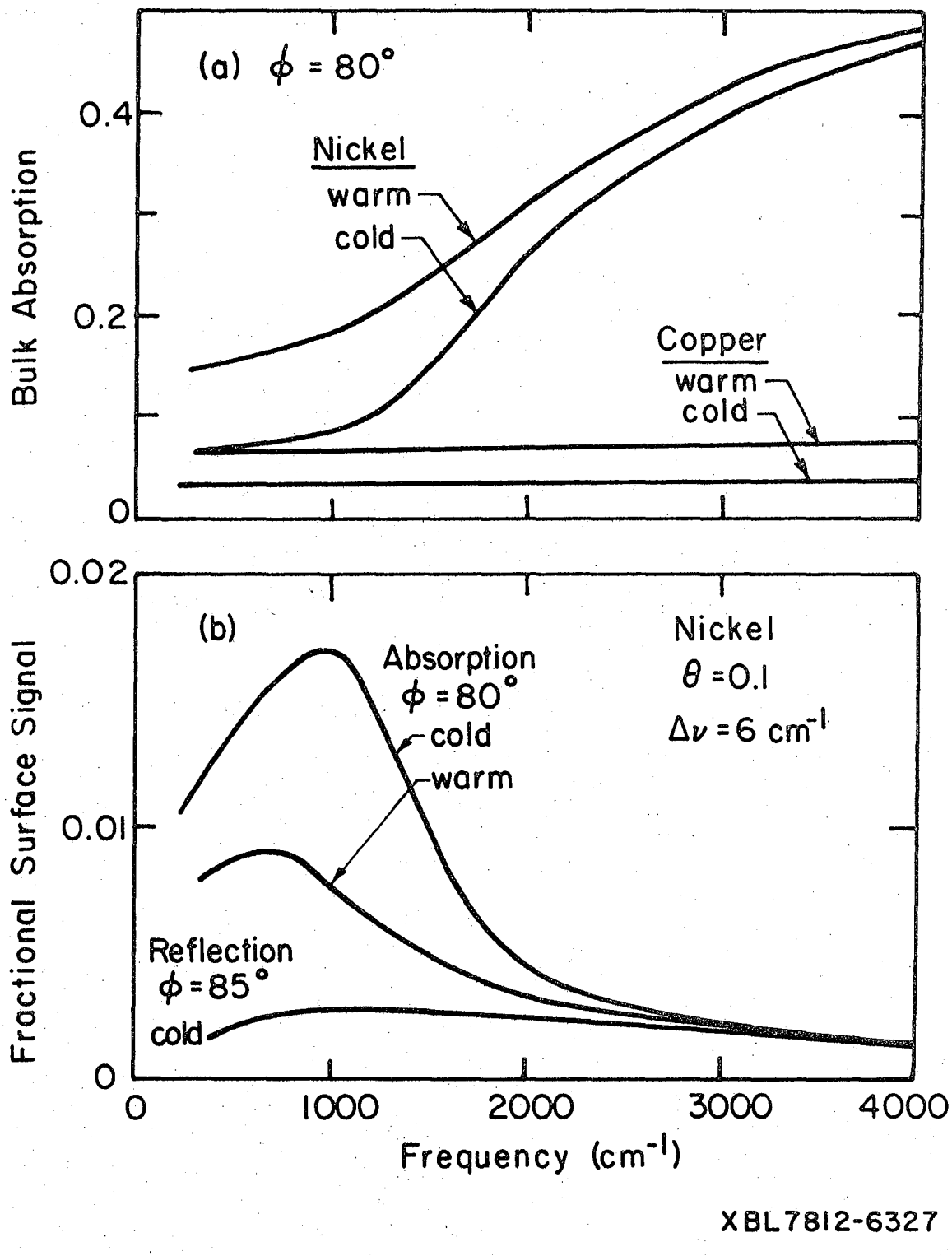

Fig. 3. Bulk and surface signal vs. infrared frequency.

Figure 4 shows the coverage dependence of the fractional absorption signal using different models to account for screening of the electric field within the surface layer. The factor $C(\theta)$ in Eq. (4) and (6) gives the size of the local field correction used in calculating the surface layer dielectric constant. For $C = 4\pi$ we subtract away the entire screening field $-4\pi P$ which is implicit in a solution to Maxwell's equation for a thin layer polarized perpendicular to its surface. This gives the unscreened absorption shown in Fig. 4. Also shown is the coverage dependence predicted by our model of a simple cubic surface lattice with $C(\theta)$ given by Eq. (5). The absorption strength begins to saturate at high coverage when the screening effect of neighboring dipoles becomes important. This saturation is also observed assuming a Lorentz local field with $C = 4\pi/3$ or assuming that the full screening field $-4\pi P$ is present in the surface layer with $C = 0$.

Another possible model of the surface layer assumes a dielectric constant which is independent of coverage and a film thickness which increases linearly with coverage.[24] Figure 4 shows the predictions of this variable thickness model using a Lorentz corrected dielectric constant calculated from Eq. (6) with $\theta = 1$ and $C = 4\pi/3$. The absorption strength is proportional to surface coverage. There is no saturation because the polarization density and screening fields are independent of θ. Even for very small surface coverages, the electric field within the film is reduced by a factor $1/\varepsilon_s$ from its value just outside the film, and this causes the variable thickness model to underestimate infrared absorptions. For a surface model to be accurate there must be no screening of the applied electric field in the limit of very small

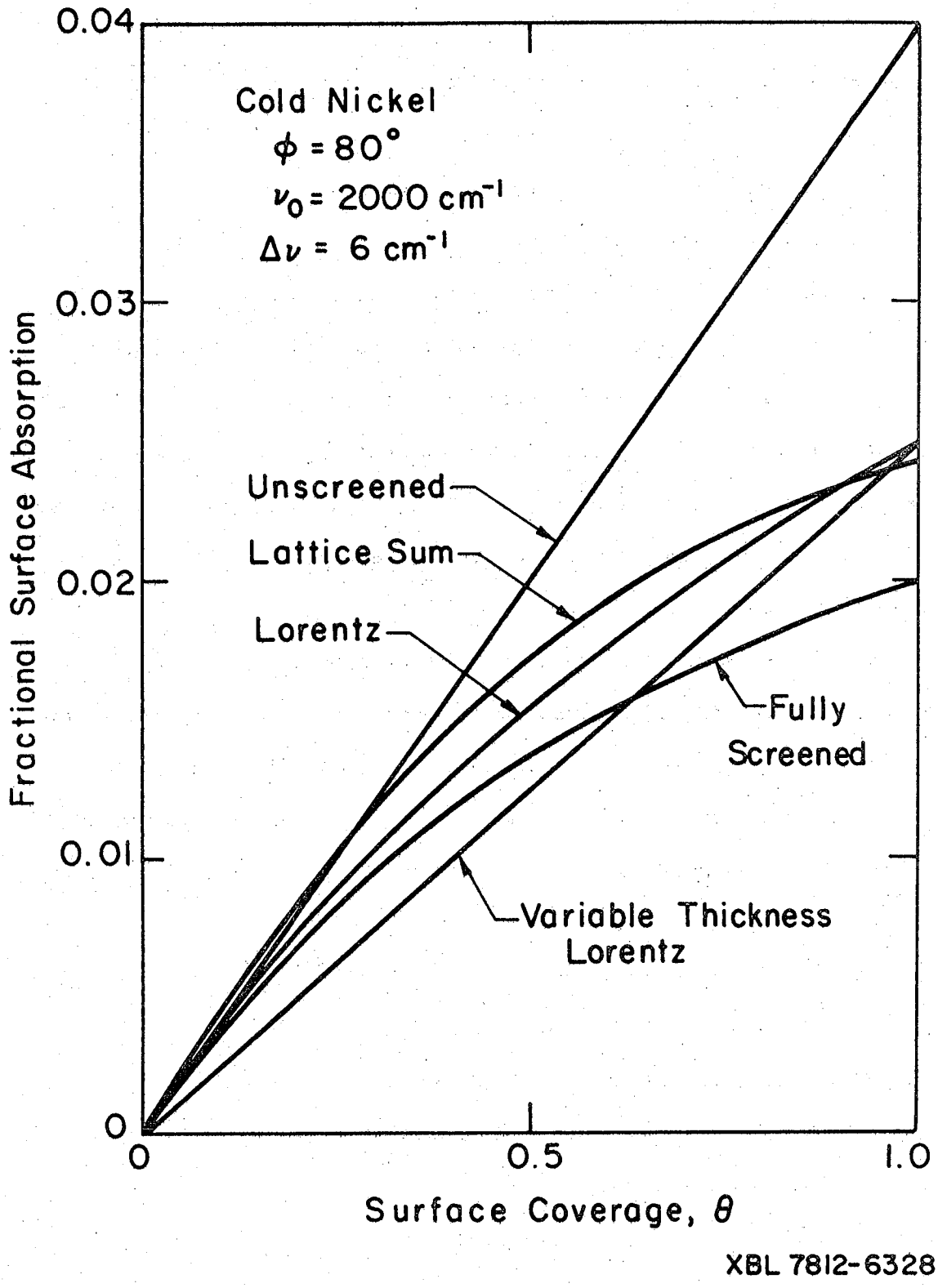

Fig. 4. Surface absorption vs. coverage calculated using different models for the dielectric constant.

coverages. This means that the dielectric constant must vary with θ and approach one as θ approaches zero.

The frequency dependence of the surface signal in the neighborhood of a molecular resonance at $\nu_o = 2000\ cm^{-1}$ is plotted in Fig. 5. The peak absorption is shifted from ν_o because the vibrational modes of neighboring dipoles and their images are coupled to each other through their electric fields. Because of the shift the surface signal calculated at the resonant frequency ν_o is less than its maximum value. In calculating the results shown in Fig. 3 and Fig. 4, we compensated for this shift by evaluating the surface absorption at the peak of the resonance rather than at frequency ν_o.

The peak absorption frequency of the coupled dipoles can be determined from the form of the resonance denominator which appears in the expression for the average polarization in the surface layer due to the applied electric field E_A. Neglecting the electronic contribution to the molecular polarizability we find from Eqs. 1, 3, 4, and 5 that

$$\frac{P}{E_A} = \frac{N_V\theta\ q^2/\mu}{\omega_o^2 + N_V\theta^{3/2}\ [A - B(\theta)]q^2/\mu - \omega^2 - i\omega\Delta\omega} \tag{9}$$

Comparing this equation to the polarizability of an isolated molecule given by Eq. (1), we find that the effective resonant frequency of the coupled oscillators is

$$\omega_{eff} = (\omega_o^2 + N_V\theta^{3/2}\ [A - B(\theta)]\ q^2/\mu)^{1/2} \tag{10}$$

Fields from neighboring dipoles are included in the lattice sum A.

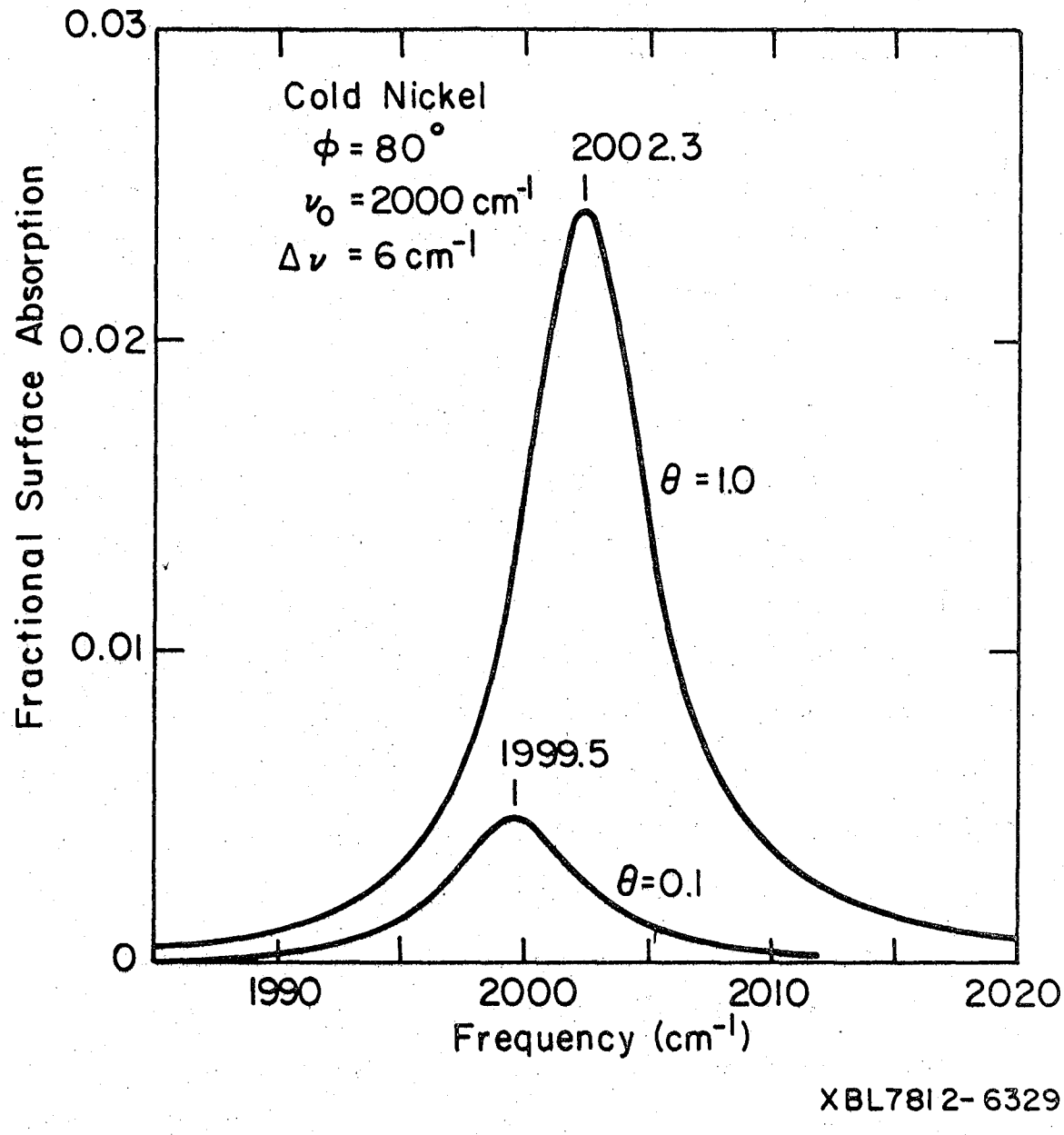

Fig. 5. Calculated absorption lineshape.

These fields oppose the externally applied field and act as additional restoring forces on the oscillating dipoles. This effectively raises the resonant frequency. The image dipoles produce an electric field of the opposite sign. For sufficiently small coverages the image contribution $B(\theta)$ exceeds the direct dipole contribution and the net frequency shift is negative as shown in Fig. 5 for $\theta = 0.1$.

E. Experimental Tests

The simple theory presented in this chapter includes only dipole-dipole interactions between molecules in the surface layer. Precise agreement with measured spectra cannot be expected since we have ignored the lattice structure of the metal substrate and the mechanism of the bond linking the molecules to the substrate. A few experiments have been performed which provide qualitative confirmation of our calculated results. Pritchard's infrared spectra[43] of carbon monoxide on copper confirm the angular dependence of the signal predicted by Greenler's original calculation[23] and by our model (Fig. 2b). The saturation of the absorption signal[44,45] predicted in Fig. 4 and the coverage dependent frequency shifts[46] predicted by Eq. (10) have also been observed in the spectra of chemisorbed CO. These effects may arise from the simple dipole electric fields of our surface model or from more complicated coverage dependent chemical interactions.[47] In Section V-A-7 we show that the intensities and frequency shifts in our spectra can be explained by dipole fields alone if we use a value for the dipole charge q of the chemisorbed CO molecule which is approximately 1.7 times that of the free molecule.

Physically adsorbed molecules provide a somewhat simpler system for testing our calculations. The linewidth measured in our experiments on physisorbed CO is approximately 6 cm^{-1} and the peak absorption strength per monolayer ranges from 1.5 to 2.8 per cent of the background absorption by the nickel film. The results of our lattice sum calculation (Fig. 4) are in good agreement predicting a 2.4 per cent signal for one monolayer. We have not yet measured the coverages and signal strengths accurately enough to verify the saturation effect. The measured frequency shifts are discussed in Section V-B-1.

III. APPARATUS AND TECHNIQUES

The thermal detection technique which we have developed makes surface absorptions more prominent than in conventional reflection spectroscopy for samples which reflect most of the incident radiation. With this advantage come two principal experimental difficulties. First, the required sensitivity and frequency response are achieved only at very low sample temperatures. This places constraints on the geometry of the vacuum chamber and limits the accessibility of the sample. It also means that we cannot study surfaces at high temperatures in equilibrium with molecules in the gas phase. Instead we must pump out the gas and cool the sample quickly to preserve the high temperature chemical state. The second problem is the intricate sample fabrication and mounting procedure required for sensitive temperature measurements. Only very thin, low heat capacity samples can be used. A tiny resistance thermometer with its electrical leads must be attached to each sample crystal, and the thermal conductance linking the sample to its low temperature heat sink must be carefully controlled.

Section A of this chapter describes the vacuum system, sample chamber, and cryostat which achieve the low temperature and ultrahigh vacuum (UHV) conditions required for infrared absorption spectroscopy of clean surfaces. In Section B we discuss the fabrication and mounting of thin Al_2O_3 single crystal samples used as substrates for the evaporated nickel films studied in our initial experiments. Section C describes the rapid scan Fourier transform infrared spectrometer which is the source of the infrared radiation. Section D

discusses the data acquisition techniques used to achieve high signal-to-noise ratios on the absorption spectra.

A. Ultrahigh Vacuum Optical Cryostat

1. Cryostat

Figure 6 shows a vertical cross section of the liquid helium cryostat and sample chamber built for our experiment. The sample mount is bolted to a liquid helium filled cold finger which extends into the sample chamber. A cryostat built onto the sample chamber's top flange supplies liquid helium to the cold finger and cools the radiation shields within the sample chamber to liquid nitrogen temperature. A minimum sample temperature of approximately 1.6 K is obtained when the pressure of the liquid helium is reduced to a few torr.

Quick sample access is achieved by disassembling the cryostat. The vacuum walls and liquid nitrogen jacket are removed first. The $4\frac{1}{2}$" flange coupling the outer wall of the cold finger to a mating flange on the sample chamber is then unbolted so that the cold finger and helium reservoir can be removed as a unit. These $4\frac{1}{2}$" flanges operate at liquid nitrogen temperature and isolate the ultrahigh vacuum of the sample chamber from the less critical cryostat vacuum space. An aluminum radiation shield is attached to the UHV side of these flanges. Mounted on this radiation shield is a cylindrical shutter which can be positioned to expose the sample to different vacuum feedthroughs mounted on the ports of the sample chamber. Electrical leads from the sample thermometer pass up along the cold finger and into the cryostat vacuum via feedthroughs in the $4\frac{1}{2}$" flange.

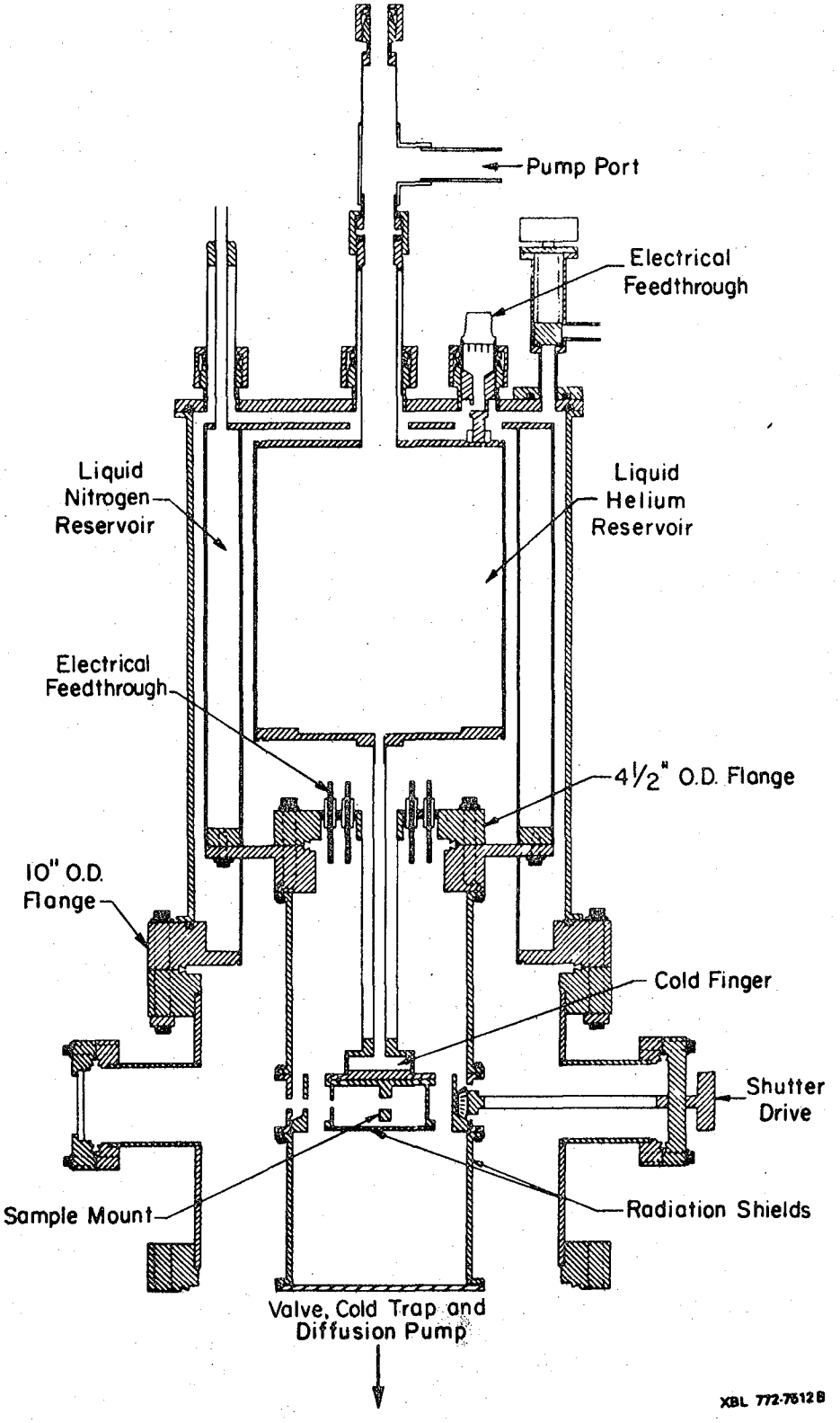

Fig. 6. Vertical cross section of sample chamber and cryostat.

They then exit the cryostat through another feedthrough mounted on the 10" diameter top flange of the sample chamber.

To cool the cryostat both the liquid nitrogen and liquid helium reservoirs are first filled with liquid nitrogen. The radiation shield extending into the sample chamber takes several hours to reach its equilibrium temperature. After this the liquid nitrogen is removed from the helium reservoir. Three to four liters of liquid helium are then required to cool and fill the two liter helium container. Next, the pump port is connected to a vacuum line and the helium pressure is reduced to a few torr. Typically the transfer takes five minutes and the pumpdown another twenty minutes. The liquid helium hold time after pumpdown is approximately eight hours.

2. Sample Chamber

The horizontal cross section of the sample chamber is shown in Fig. 7. The sample is mounted on the cold finger in a fixed position at the center of the eight inch diameter chamber and is surrounded by radiation shields at liquid helium and liquid nitrogen temperature. These cold surfaces block most of the room temperature thermal radiation which would heat up the sample and make it less sensitive to the radiation incident through the infrared window. Access to the sample by room temperature vacuum feedthroughs is through 4 mm diameter holes in the radiation shields. The cold shutter is positioned so that only the infrared port is left open during spectral measurements. For most experiments the thermal background radiation hitting the sample is then less than the radiation incident from the infrared source in our spectrometer.

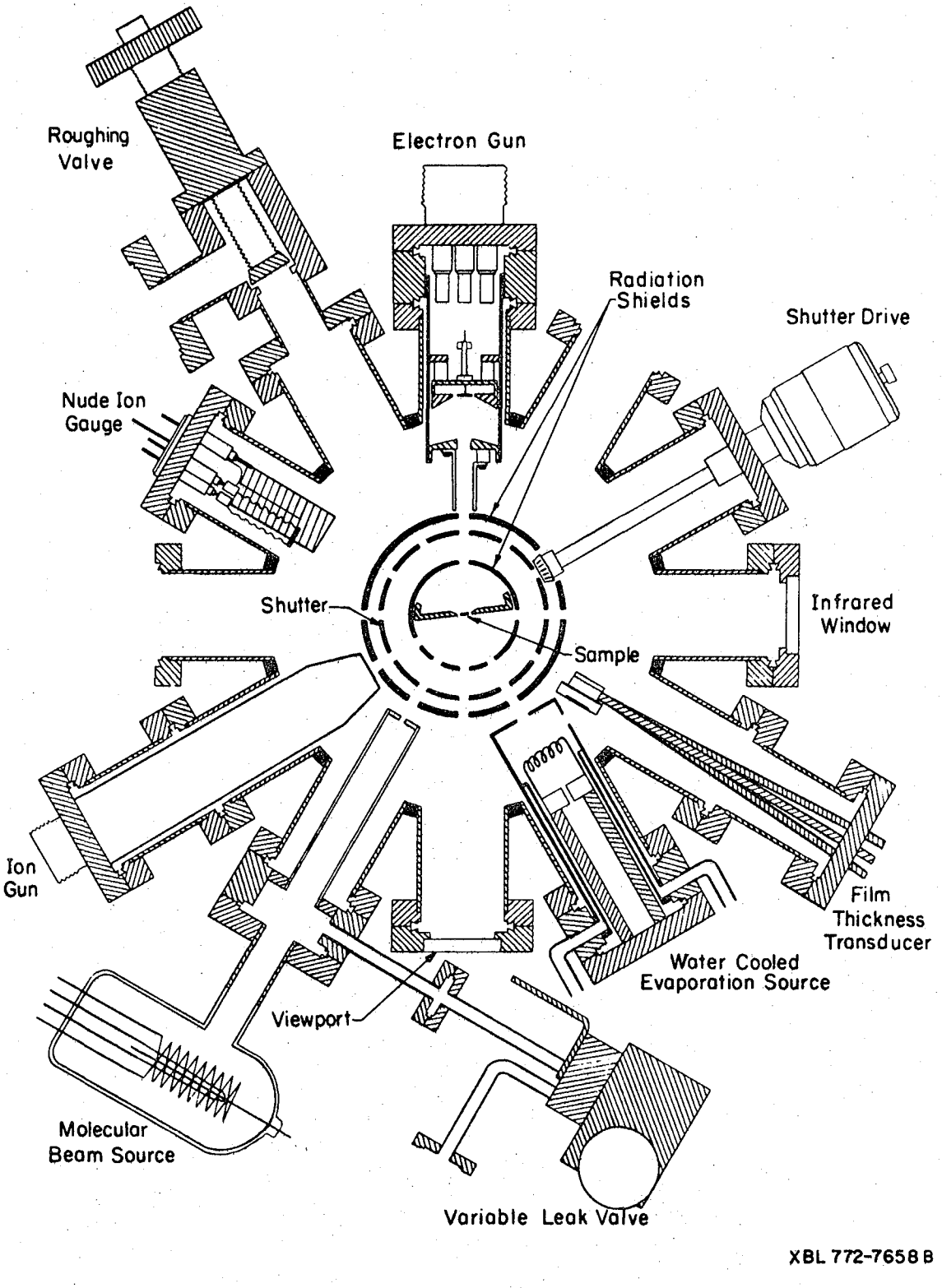

Fig. 7. Horizontal cross section of sample chamber.

By surrounding the sample with radiation shields we reduce the pumping speed in this region by orders of magnitude and expect the pressure there to be much higher than that measured outside the radiation shields. After bakeout and with the cryostat at room temperature, the gauge installed on a feedthrough port reads 1.5×10^{-10} torr. Near the sample the pressure is probably about 10^{-8} torr. This pressure is proportional to the outgassing rate of the warm metal surfaces within the radiation shields. When the cryostat is cooled to 77 K, the pressure at the sample should be much closer to that read by the gauge. With the cold finger at temperature 1.6 K, outgassing ceases, and the only source of sample contamination is the direct flux of molecules incident through the ports in the radiation shields. With only the infrared port left open, the solid angle exposed to room temperature surfaces is 5×10^{-3} steradians.

The sample chamber has twelve symmetrically placed feedthrough ports sealed by 2.75" diameter flanges. Below we give a brief description of each of the 10 devices installed on these feedthrough ports starting with the infrared window and proceding clockwise in Fig. 7.

a. Infrared window. A one inch diameter, 4 mm thick KRS-5 window fits into a seat machined in a blank flange. A metal ring bolts to the flange and compresses the window onto an indium foil gasket forming a reliable vacuum seal which has survived three bakeout cycles. KRS-5 is a composite alkali halide material (thallium bromide-thallium iodide) which transmits infrared frequencies greater than 200 cm^{-1}. It has a

relatively high insertion loss of 30 per cent due to dielectric reflections, and the sealed window assembly has a clear aperture of only 1.3 cm.

b. Film thickness transducer. A Kronos model FTT-300 bakeable film thickness transducer is installed adjacent to the evaporation source to monitor the deposition rate for the metal films evaporated on the sample crystal. The transducer element is a thin quartz crystal. Its mechanical oscillation frequency is monitored by an external circuit and shows a decrease proportional to the mass of the deposited film.

c. Water-cooled evaporation source. A cylindrical copper shroud brazed to a double sided flange is installed on this port to intercept most of the metal evaporated from the tungsten filament. Holes in the shroud allow beams of metal atoms to hit the sample and the film thickness transducer. Both the copper shield and the copper electrical feedthroughs which support the filament are water-cooled and dissipate a large fraction of the 500 watts required to evaporate a nickel film. Heating effects still increase the pressure in the sample chamber from 10^{-10} torr to 10^{-9} torr during the evaporation.

Electroplated tungsten filaments are used as sources for evaporating nickel films. Approximately 2000 Å can be deposited on the sample from a single filament. Copper requires a much lower evaporation temperature and has been deposited from an Al_2O_3 crucible source which is heated by a coil of tungsten wire.

d. Viewport. This window is useful for viewing the sample and in determining the position of the shutter.

e. Molecular beam source. A gas cell formed on this port provides a calibrated source of molecules for doping the sample surface. The orifice coupling the cell to the sample chamber is a 0.24 cm diameter hole drilled through a 0.32 cm plate and located 6 cm from the sample crystal. A variable leak valve and ion guage allow us to accurately control the cell pressure. For pressures less than 10^{-3} torr the mean free path of the molecules exceeds the cell dimensions, and the flux through the orifice can be calculated in the molecular flow limit.[49] The result for the number of molecules/sec incident on the sample per unit sample area is

$$F_c = 3.3 \times 10^{17} \frac{P_c}{\sqrt{W}} \qquad (11)$$

where P_c is the gas cell pressure measured in torr and W is the molecular weight of the incident particles. For $P = 10^{-3}$ torr of carbon monoxide with W = 28, the flux is 6.2×10^{13} molecules/sec cm^2. A monolayer is formed from roughly 10^{15} molecules/cm^2 so that the deposition rate in this example is approximately one monolayer every 16 seconds.

Whenever gas is introduced into the cell the pressure in the main vacuum chamber rises and contributes an indirect flux of molecules to the total direct flux incident upon the sample from the gas cell orifice. With the cold finger at liquid helium temperature this indirect flux is negligible due to the cryopumping action of the cold surfaces. If the cold finger is at liquid nitrogen temperature, then many gases

will not condense on its surfaces, and the pressure at the sample will equal the system pressure P_s. From kinetic theory[50] the flux of molecules incident upon the surface per cm^2 is

$$F_s = 3.5 \times 10^{22} \frac{P_s}{\sqrt{WT}}$$

where T is the gas temperature and P_s is measured in torr. This flux is usually comparable to the direct flux from the gas cell orifice so both contributions must be included when estimating the gas exposure.

Gases are introduced through the leak valve from Matheson lecture bottles connected to the appropriate system of valves and regulators. When not in use the gas handling manifold is kept evacuated by a small untrapped diffusion pump to reduce the level of contaminants present.

f. Ion gun. We use a Varian model 981-2043 ion bombardment gun in our thin film studies to remove adsorbed molecules after recording their infrared spectrum. A reference spectrum of the metal film without the molecules can then be measured. A background pressure of 10^{-6} torr of argon must be introduced into the vacuum system to provide a source of ions for the gun. The sample temperature is elevated to approximately 200 K during bombardment to prevent condensation of the argon gas.

g. Nude gauge. Varian model UHV-24.

h. Roughing valve. Granville Phillips model 204 gold sealed ultrahigh vacuum valve.

i. Electron gun. For heating the sample crystal we have built a simple electron gun[51] designed to operate with up to 20 A filament

current and 3 kV accelerating voltage. Electrostatic deflection plates adjust the position of the beam. For the measurements described in this thesis, sample temperatures never exceeded 450 K. In this temperature range resistive heating of the sample, described in Section III-B, was found to be more efficient and more easily controlled than electron bombardment heating. The filament of the electron gun did prove useful as a light source when inspecting the sample through the viewport.

j. Shutter drive. A rotary vacuum feedthrough turns a gear which positions the cylindrical shutter.

3. Vacuum Techniques

The pumping station which evacuates the sample chamber consists of a gate valve (Huntington model GVA-800), a cold trap (Granville Phillips model 278), and a diffusion pump (Varian model VHS-6). A sorption pump (Varian model 941-6501) reduces the sample chamber pressure to a few microns before the gate valve to the diffusion pump is opened. A molecular sieve trap (Ultek model 232-1102) located between the diffusion pump and its mechanical forepump prevents migration of the forepump oil into the diffusion pump.

All the seals between ultrahigh vacuum and atmospheric pressure are made with metal gaskets except for the viton sealed flanges connecting the diffusion pump and cold trap. Within the ultrahigh vacuum there is a viton O-ring which forms the gate valve seal. All other materials are either metals or vacuum grade ceramics which have been degreased and chemically cleaned using standard techniques.[52]

Bakeout of the system is accomplished by lowering an oven into place over the sample chamber and gate valve and by wrapping the cold trap with heater tape and fiberglass insulation. The procedure followed is to heat the cold trap to 70 C and the sample chamber to 100 C for one day. The trap is then allowed to cool to room temperature before filling it with liquid nitrogen. The sample chamber and valve are then baked for two more days before removing the oven and beginning a series of experiments. A pressure of 1.5×10^{-10} torr is maintained as long as the liquid nitrogen trap is kept cold. The pressure drops to 9×10^{-11} torr when the cryostat is cooled. The limit on the bakeout temperature for the current system is 155 C. This is the melting point of the indium metal used in sealing the infrared window and in fabricating the sample assembly.

B. Sample Assembly

1. Design Philosophy

In our experiment the optimum sample assembly is one which is sensitive to the smallest fractional change in the absorbed infrared power. A similar optimization problem occurs in the design of bolometers for the detection of infrared radiation in laboratory and astronomical experiments.[20,21] We show in Chapter IV that the sample's heat capacity and temperature should be as low as possible. The optimum value for the thermal conductance linking the sample to its low temperature heat sink will then depend on the spectrometer's modulation frequency and the amount of incident infrared power. In addition to achieving a high sensitivity, the design must provide a

convenient means for heating the sample, and it must allow access to the sample by the various sample preparation feedthroughs described in Section III-A. Finally all materials used in fabricating and mounting the sample assembly must be low vapor pressure metals or ceramics appropriate for use in a bakeable ultrahigh vacuum system.

Figure 8 is a simplified drawing of the sample assembly used in our experiments on evaporated nickel films. The thin polished Al_2O_3 single crystal substrate is mounted in a vertical plane at the center of the sample chamber and faces the viewport shown in Fig. 7. It is rotated slightly toward the infrared window so that the infrared beam strikes the crystal at an angle of incidence 82° from the normal to the surface. In this orientation the ion gun, molecular beam source, and evaporation source all have access to the sample face which is exposed to the infrared beam.

The sample crystal is shown suspended between pairs of thin tungsten wires which are anchored to the cold surfaces of the sample mount. Current can be passed through these wires to resistively heat the crystal. Only 300 mW of electrical power is required to warm the sample from 1.6 K to 400 K. This approximately triples the liquid helium consumption by the cryostat, but for brief heating cycles the effect on the total liquid helium hold time is small.

The gallium doped germanium thermometer crystal has dimensions 0.8 mm × 0.5 mm × 0.2 mm and a temperature dependent resistance $R = 1320 \exp(9.43/T)$ ohms for the temperature range 1.5 K to 2.0 K. The copper electrical leads used to measure this resistance are brought

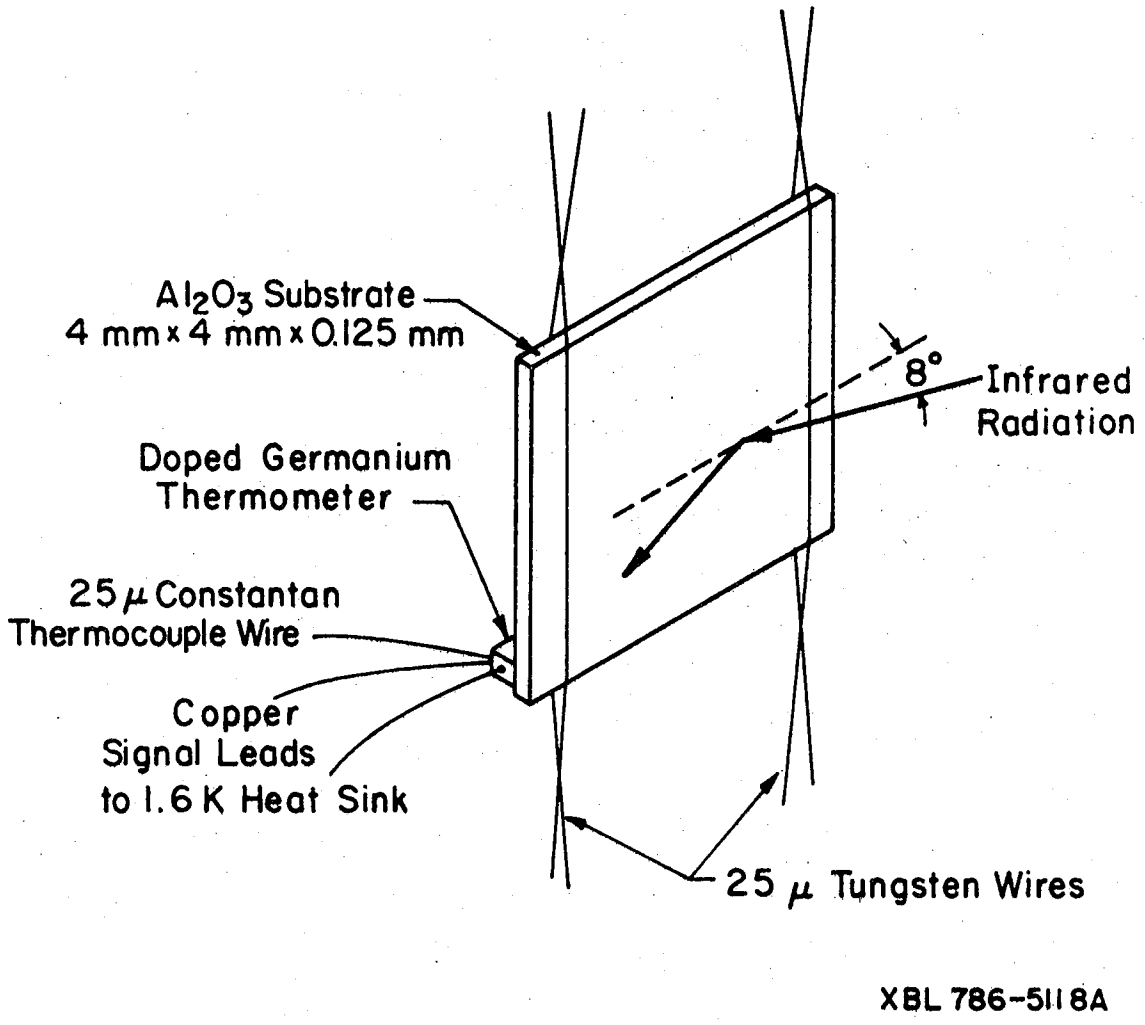

Fig. 8. Sample assembly for evaporated film experiments.

into contact with electrically insulated heat sinks on the sample mount before passing out of the vacuum system. The length and diameter of the wires are chosen to produce the optimum value of the thermal conductance between the sample and the 1.6 K reference temperature of the cold finger. The constantan wire shown in Fig. 8 forms a thermocouple junction with one of the copper signal leads and measures the sample temperature during heating cycles.

2. Sample Fabrication

The sample assembly is fabricated in three steps. A pair of nickel plated molybdenum contacts approximately 0.5 mm in diameter and 1 mm apart are first formed on the Al_2O_3 substrate. Copper and constantan electrical leads are then attached to these contacts using lead-tin solder. Finally, indium metal is used to connect opposite ends of the germanium thermometer crystal to the two contacts. The melting point of indium is 155 C, setting an upper limit on the operating temperature of this assembly. By replacing the low melting point solders with appropriate brazing alloys or by utilizing spot welds or compression bonds, a sample of this type can be fabricated for use at much higher temperatures.

To form the metallic contacts on the Al_2O_3 crystal we use a standard process developed for metallizing ceramics.[53] A paint (Western Gold and Platinum #598) consisting of finely divided grains of molybdenum and manganese is first applied to the crystal where the contacts are to be formed. After the paint dries, the crystal is placed on the tungsten boat of a vacuum evaporator and heated slowly

to 1400 C in a hydrogen atmosphere. The temperature is measured with an optical pyrometer. After an hour at 1400 C the sample is cooled slowly to room temperature. The contacts are then sanded down to a few microns thickness and appear bright and metallic. Before soldering to the contacts they must first be nickel plated. A relatively thick electroplated deposit is made and then sanded down. The thinnest possible layers of molybdenum and nickel are used in order to minimize the sample's heat capacity.

The next assembly step is to solder the electrical leads to the outside edges of the nickel plated contacts. A single 50 μm diameter copper wire is soldered to one contact, while 25 μm wires of copper and constantan are soldered to the other. These operations are carried out while viewing the sample with a stereo microscope. The quantity of solder used is kept to a minimum.

Finally the germanium thermometer is attached to the substrate in a position bridging the two contacts. The procedure adopted is to first form indium contacts on the ends of the germanium crystal and then solder it in place on the substrate. After cutting the germanium crystal to the desired size, it is etched for a few minutes in a 5:1 solution of HNO_3:HF and rinsed in methanol. It is then clamped on a heatable ceramic stage and viewed under magnification. Tiny pieces of indium metal are placed on opposite ends of the crystal. An airtight cover is then installed over the assembly stage and flushed with dry nitrogen to prevent heavy oxidation as the crystal is heated. Above its melting point the indium forms a spherical bead without

wetting the germanium. By elevating the temperature further and introducing a dose of HCl from a gas cylinder, the indium is made to flow onto the crystal surface. Using the same technique at a somewhat lower temperature, the metallized germanium is then bonded to the nickel contacts of the sample crystal. Care is taken not to allow mixing of the indium and lead-tin solders because alloys with undesirable properties may form.

3. Sample Mounting

The mounting hardware pictured in Fig. 9 consists of a stainless steel sample holder bolted to a two inch diameter copper baseplate which is in turn bolted to the cold finger. The sample holder supports the thin tungsten wires which suspend the sample crystal. One end of each wire is attached to a ceramic insulator forming an electrical terminal for heating the sample. A current of approximately 0.4 A passed through the support wires is necessary to warm the sample from liquid helium temperature to room temperature. The optical baffles shown bolted to the sample mount are sections of razor blades which mask the edges and rear surface of the sample from the infrared beam. These baffles are in direct contact with the sample crystal but do not contribute substantially to the total thermal conductance between the sample and mounting hardware.

The rear view of the sample mount shows that the signal and thermocouple leads from the thermometer crystal are soldered to electrical terminals mounted on ceramic heat sinks. The ceramic is metallized using the procedures described in the previous section and

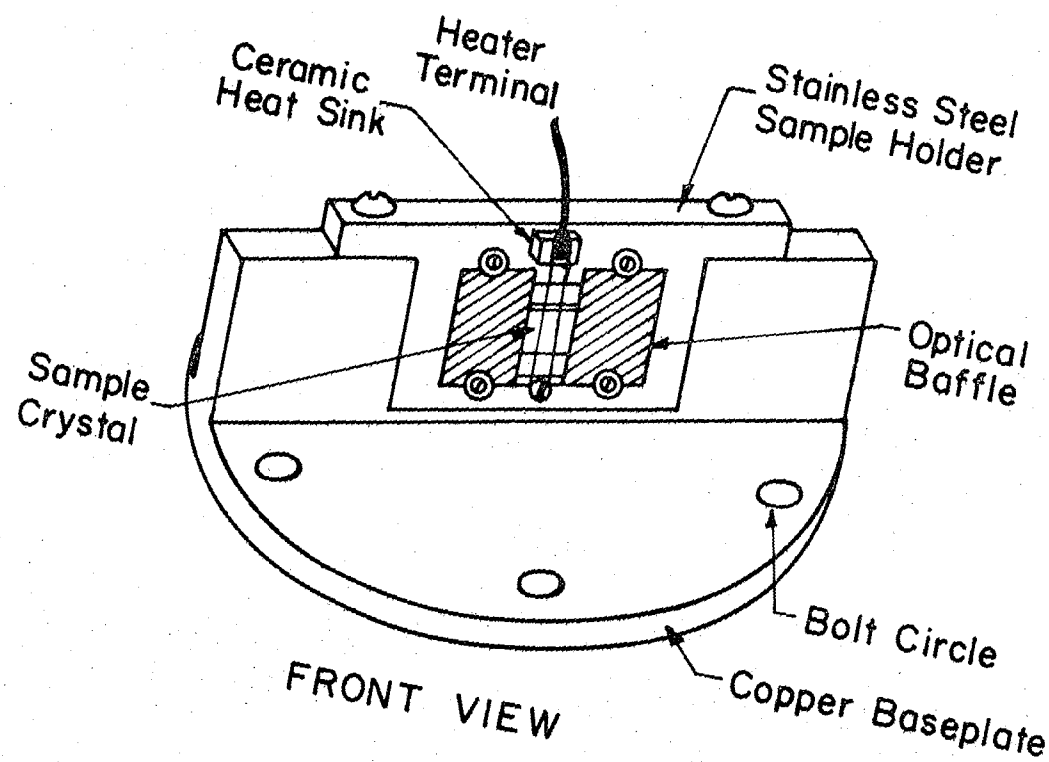

Fig. 9. Mounting hardware for sample crystal.

XBL 7812-6330

then soldered to the copper baseplate. The copper signal leads are approximately 0.6 cm long and provide the largest thermal conductance between the sample and the baseplate. The electrical connections to the vacuum feedthroughs on the $4\frac{1}{2}$" liquid nitrogen temperature flange (Fig. 6) are made with thin-walled sections of sixteenth inch diameter stainless steel tubing. These have low thermal conductivity and sufficient mechanical rigidity to prevent vibrations, which are a source of noise in high impedance electrical circuits.

C. Spectrometer

In our measurements we have used an EOCOM 7001P rapid scan Fourier transform spectrometer. The principles of Fourier spectroscopy have been reviewed extensively,[54-56] and only the essential details will be discussed here. The optical components of the spectrometer, shown in Fig. 10, include a Michelson interferometer, the appropriate input and output optics, and a blackbody infrared source. Broad band radiation from the source is filtered and collimated and then divided into two beams by the beamsplitter. The waves interfere when they recombine to form the output beam which is focused onto the sample by a lens. Interference modulations are produced in the output beam intensity when the mirror in one of the arms of the interferometer is moved. These modulations are characteristic of the spectrum of the radiation in the beam. The interference pattern is called an interferogram, and its Fourier transform is the infrared spectrum. The interferogram has its maximum value when the two mirrors are at the same distance from the beamsplitter and all the wavelengths interfere constructively.

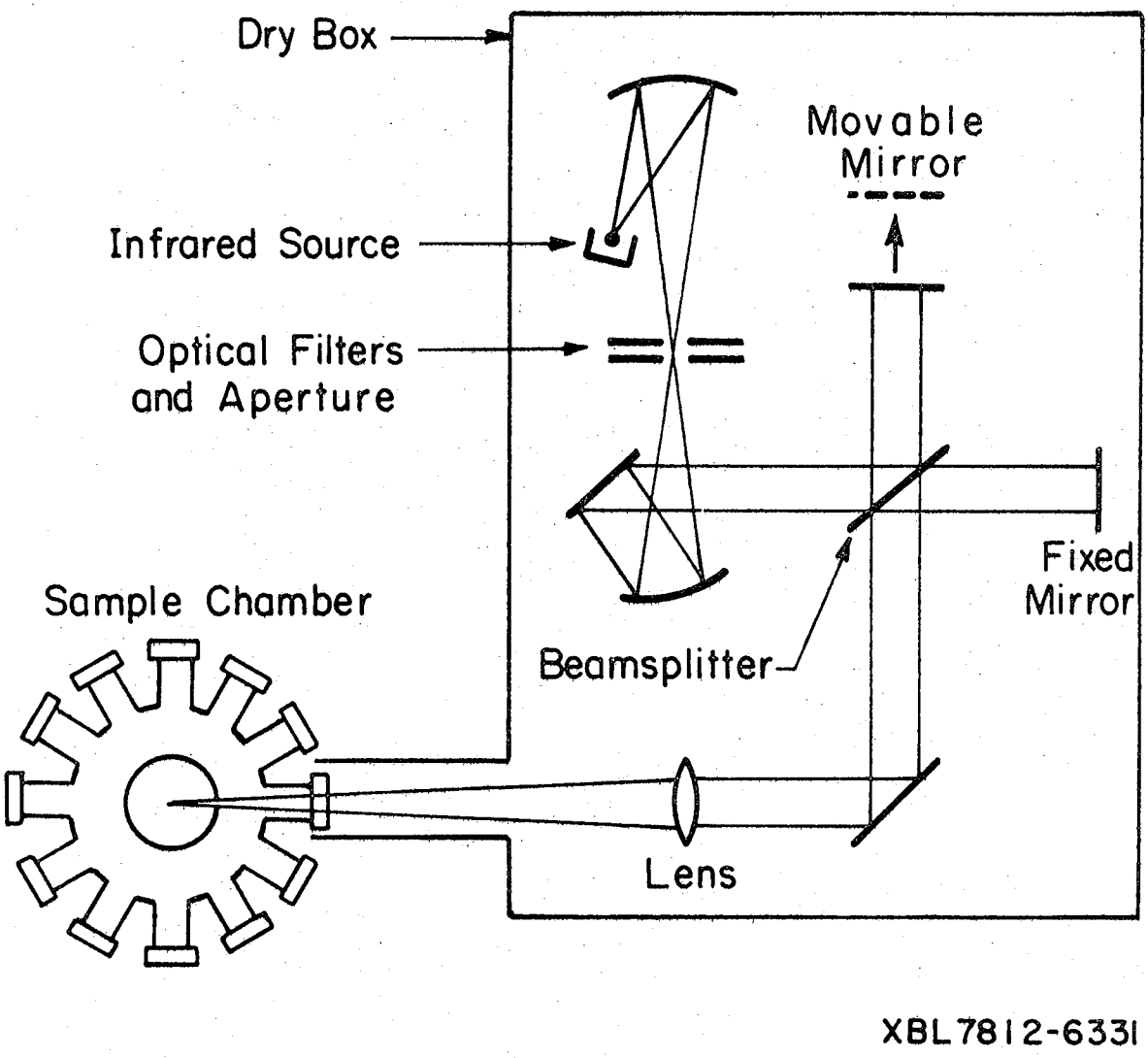

Fig. 10. Optical components of rapid scan Fourier transform spectrometer.

This is the point of zero optical path difference.

A rapid scan Fourier spectrometer translates the movable mirror at a constant velocity v and repeats a scan through the zero path point every few seconds. For radiation of wavelength λ the electric field amplitude of the transmitted radiation is modulated sinusoidally and goes through a full cycle of constructive and destructive interference in a time t such that $vt = \lambda/2$. Its intensity modulation is given by

$$I \propto 1 + \cos(4\pi vt/\lambda)$$

Each spectral component of the infrared beam contributes an intensity modulation on the interferogram at the audio frequency

$$f = 2\frac{v}{\lambda} = 2v\nu \qquad (12)$$

where ν is the infrared frequency in cm^{-1}. It also produces a constant unmodulated baseline intensity. The audio frequency spectrum of the interferogram gives the infrared spectrum of the detected radiation.

The major advantage of the rapid scan spectrometer in our application is its ability to do long integrations automatically and its insensitivity to low frequency noise sources and drift. The integrations are accomplished by averaging the interferograms produced by successive scans of the spectrometer mirror. Because each scan lasts only a few seconds, the effect of slowly drifting signal levels is only to shift the scale of successive spectra.

Separate light beams from a helium neon laser and an incandescent bulb are directed through the EOCOM spectrometer along with the infrared signal beam. The sinusoidal interference signal from the

laser light determines the relative position of the moving mirror. The zero path peak from the incandescent white light source provides a reference signal at the beginning of each mirror scan. The length L of the mirror scan determines the spectral resolution 1/4L. The ultimate resolution is 0.065 cm^{-1}. The mirror velocity is variable from 0.03 to 4.0 cm/sec producing modulation frequencies from 120 Hz to 16 kHz for the infrared frequency 2000 cm^{-1}.

Figure 11 shows the interference modulations near the zero path mirror position and the calculated infrared frequency spectrum for the radiation absorbed by a nickel film covered with 2.7 monolayers of physically adsorbed carbon monoxide. The frequency spectrum is that of the blackbody source as modified by the transmission function of the spectrometer and the absorption spectrum of the sample. The structure observed between 500 cm^{-1} and 1400 cm^{-1} is caused by phonon absorptions in the Al_2O_3 sample crystal. These occur because a small amount of infrared power is incident on the unmetallized portions of the sample. Atmospheric water vapor absorption in the spectrometer reduces the intensity of the incident radiation and causes the bands of sharp structure centered at 1600 cm^{-1} and 3800 cm^{-1}. The spectrometer is enclosed in a lucite box and flushed with dry nitrogen gas to decrease the water vapor absorptions. Further improvement can be achieved by sealing the box more tightly and by maintaining the gas flow for longer periods before measuring the spectrum. The peak in the absorption spectrum at 2140 cm^{-1} is the carbon monoxide signal. By subtracting the spectrum of a clean metal surface, this molecular absorption can be

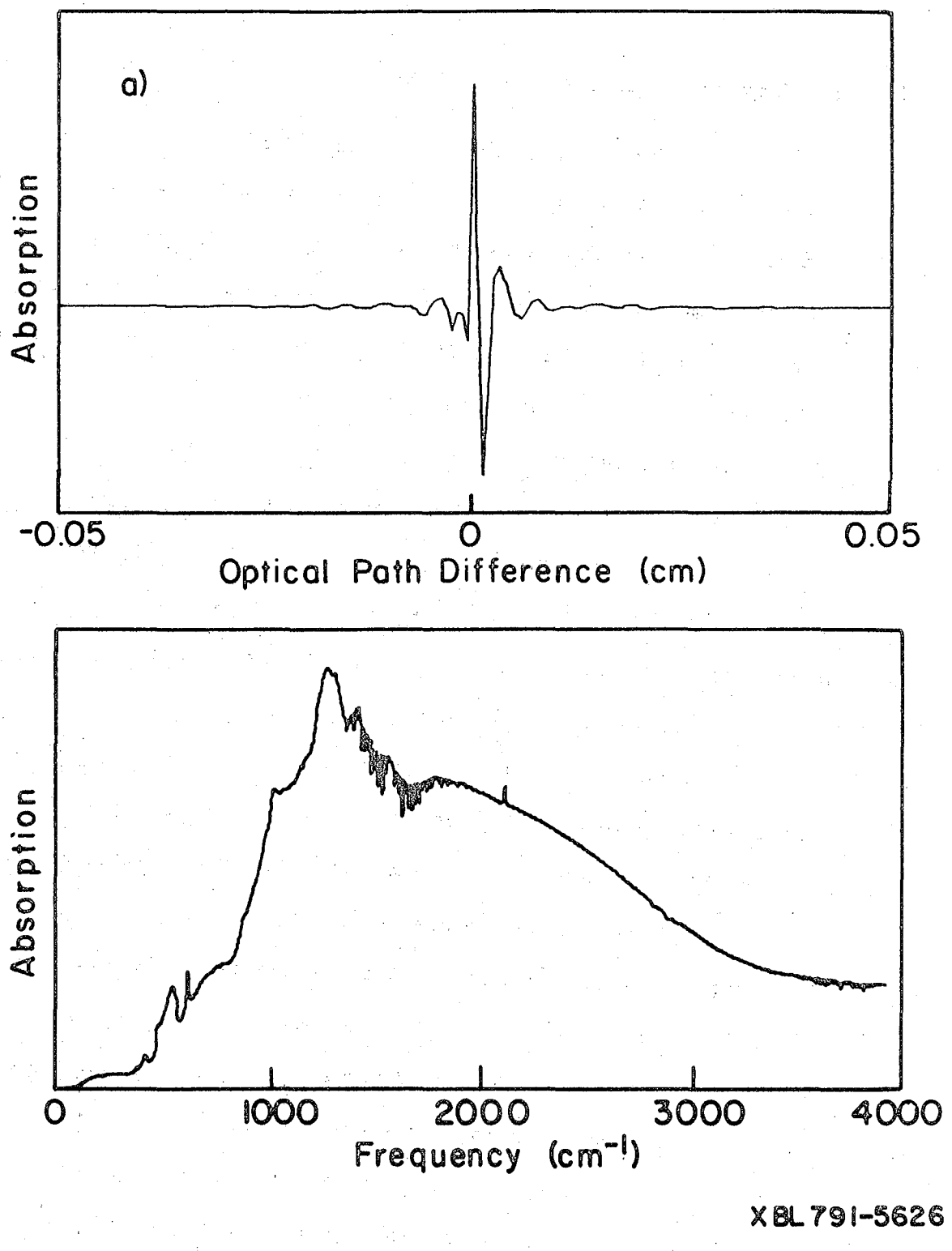

Fig. 11. (a) Interferogram and (b) calculated spectrum for CO molecules physisorbed on a nickel film.

isolated from the other spectral features.

D. Data Acquisition and Analysis

Our data acquisition electronics must record the resistance of a thermometer crystal at thousands of equally spaced positions of the scanning spectrometer mirror. The data from thousands of these mirror scans must be averaged and stored for later analysis. Figure 12 shows a block diagram of the system which performs these tasks.

The thermometer resistance, typically 250 kΩ, is measured by biasing it with a constant current and amplifying the resulting voltage signal. The current is adjusted by varying the voltage applied to a 9.2 MΩ wirewound resistor in series with the thermometer. To reduce its Johnson noise,[60] this load resistor is kept cold by mounting it on the base of the liquid helium reservoir of the cryostat. For the present detector and optical system, bias currents of a few microamps produce peak interferogram signals of approximately 25 mV. This signal is amplified to 10 V by a low noise preamplifier (Princeton Applied Research model 185) and passed through an electronic filter (Kron-Hite model 3750) to remove modulation frequencies outside the range of interest.

The sample clock signal from the spectrometer is a series of pulses derived from the laser interference fringes. The pulses begin when the white light interferometer zero path signal is detected and stop when the mirror reaches the end of its scan. The arrival of a pulse indicates that the infrared signal should be digitized. The output of the sample-and-hold amplifier is then held constant while the anolog-to-digital converter (Phoenix Data model 1251) converts the voltage into a 16-bit

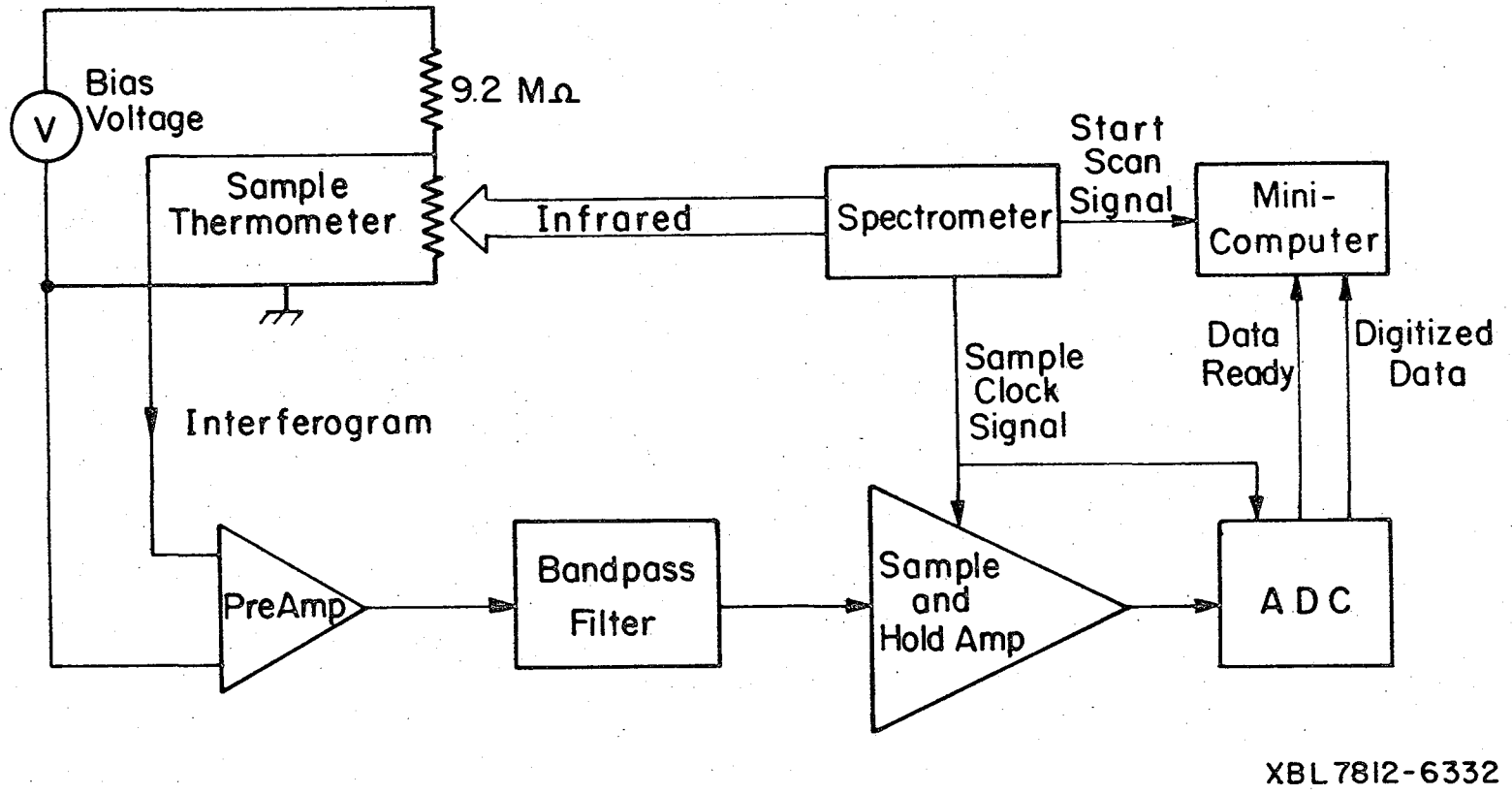

Fig. 12. Data acquisition system.

binary number and stores the result in its output register. The ADC accepts input voltages between -10 V and +10 V and has a resolution of 305 μV. The conversion requires 10 μsec and a DATA READY signal is sent to the minicomputer (Digital Equipment Corporation PDP11-20) when the new data is available.

A limit of 4096 data points per scan is set by the size of the computer memory. Because the noise on the data from a single scan occurs in the last few bits of a 16-bit computer word, we must store the accumulated result of many scans in a two word format. This is done by adding successive interferograms and using double precision arithmetic to obtain a 32-bit result. Computer controlled data acquisition is initiated by entering a teletype command specifying the number of data points to measure in a single scan and the number of scans to add together. The computer then uses the START SCAN signals from the spectrometer and the DATA READY signals from the ADC to synchronize the process of reading in and adding together the data from successive spectrometer scans.

The minicomputer is programmed to do only single word Fourier transforms so our double precision data must be truncated to 16-bit accuracy for on-line analysis. The 32-bit data are recorded on tape and transferred to a CDC 7600 computer, which does 64-bit arithmetic, to produce more accurate spectra. The 4096 point interferograms recorded in our experiments contain 700 points before the zero path mirror position. Two sided amplitude Fourier transforms[66] are used to calculate the frequency spectrum. The on-line computer is

also programmed to calculate the rms noise spectrum of an electrical signal making it possible to accurately determine the noise contributions from different elements of our system.

IV. SYSTEM PERFORMANCE

A primary goal of our experiments is to study hydrocarbons chemisorbed on metal surfaces. These molecules have smaller peak absorptions than carbon monoxide, and further improvements in our sensitivity are required to detect them in small surface concentrations. In this chapter we present a detailed quantitative analysis of the performance and limitations of our experimental apparatus in its present state. The measured properties of our nickel film sample serve as a numerical example. We develop an expression for the fractional noise on an absorption spectrum as a function of the different experimental variables and use it to predict the sensitivity of experiments involving different sample heat capacities and different infrared frequency bands. The principal findings are that excess noise from the spectrometer, digitizing electronics, and thermometer crystal presently limit our sensitivity. It should be possible to reduce these noise contributions and to approach the fundamental photon noise limit giving us a factor of 10 improvement in sensitivity.

A. Optical System

Both the signal and noise levels in our thermal detection scheme depend on the amount of infrared power incident on the sample. The total power P is the sum of three terms

$$P = P_s + mP_s + P_b$$

where P_s is the unmodulated component of the spectrometer output beam, and P_b is the thermal background radiation from room temperature surfaces

which leaks through the radiation shields and strikes the sample crystal. The term mP_s is the peak interference modulation produced by the spectrometer. It is present only when the mirror passes through its zero path position. The modulation factor m has its maximum value of one for a perfectly aligned interferometer.

Figure 13 is a schematic diagram of the optical system. The spectrometer has 5 cm diameter optical components, and the input collimator is a 23 cm focal length parabaloidal mirror pictured as a lens. The output beam is focused onto the sample by a 41 cm focal length KRS-5 infrared lens. The angle of incidence $\phi = 82°$ is close to the value for which adsorbed molecules produce the maximum fractional absorption change. The sample accepts radiation from the spectrometer within a cone of half-angle $\gamma = 2.3°$. This angle is defined by the 1.3 cm diameter vacuum window positioned 16.4 cm from the sample and by the 4 mm diameter aperture in the liquid nitrogen temperature radiation shield located 5 cm from the sample.

The total unmodulated signal power at the spectrometer output, measured with a calibrated thermocouple detector (Scientech model 360001), is $P_s = 16$ mW. For a blackbody source of area A_s and temperature T_s the power emitted into a cone of half angle α in the forward direction is

$$P = \sigma T_s^4 A_s \sin^2 \alpha$$

where $\sigma = 5.67 \times 10^{-12}$ W/K^4 cm^2. Using the estimated temperature T = 1300 K, the source aperture diameter of 0.64 cm, and the collection

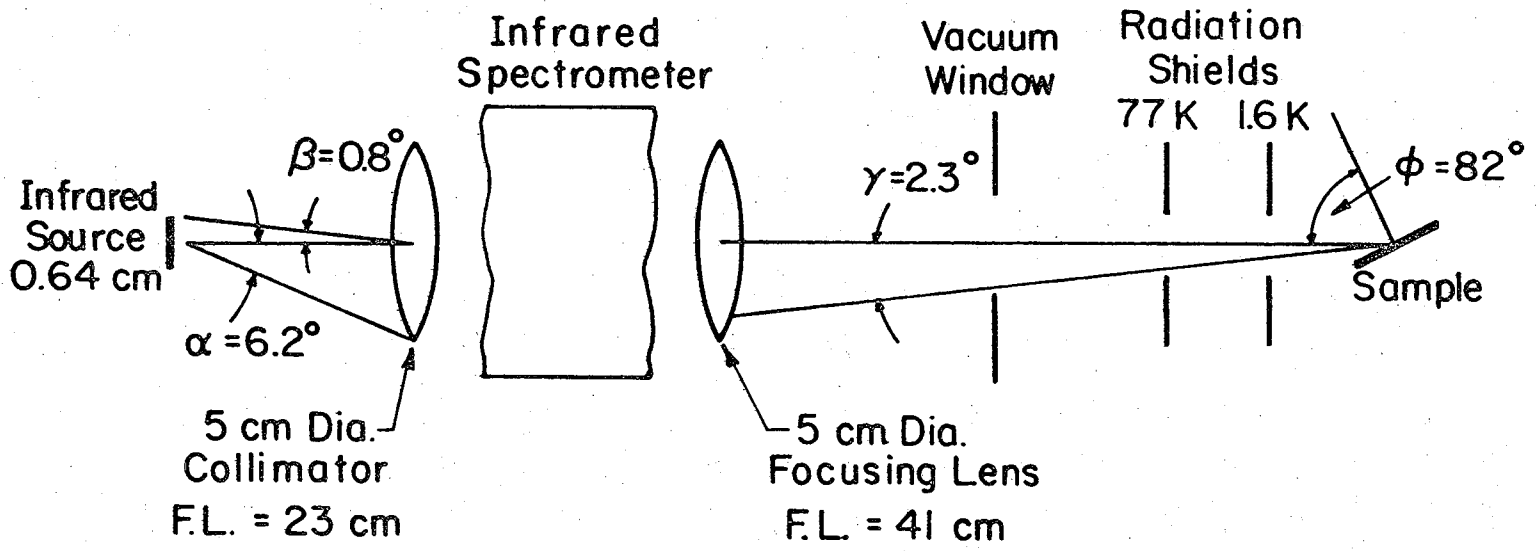

Fig. 13. Optical system.

angle $\alpha = 6.2°$, we calculate P = 61 mW. This is four times the measured output power and indicates that the spectrometer efficiency is roughly 25%. Using the 0.64 cm source aperture and detecting the entire infrared spectrum, the spectrometer's modulation factor is found to be m = 0.44. Values approaching one are obtained only if we filter out short wavelength radiation and reduce the source aperture to eliminate off axis rays.

Next we estimate the fraction of the available infrared power which is incident on the sample. With the focusing lens removed, the beam divergence angle β is less than the sample's acceptance angle γ. The power hitting the sample should then be the total power of 16 mW reduced by the ratio of the sample area to the beam area. An additional attenuation factor of 0.7 must be included to account for the dielectric reflection losses at the KRS-5 infrared window. We estimate that a 4 mm × 4 mm sample mounted at an angle of 82° to the beam will intercept 13 μW of power. Of this only 6.5 μW is polarized parallel to the plane of incidence so that it can interact with the surface layer. The observed signal increases by a factor of 2.5 when the lens is installed in the output beam. The total infrared power incident on the sample in each polarization state is therefore 16 μW.

The optical system of Fig. 13 uses only 0.2% of the total power in the spectrometer beam. An improved optical system with an 8 cm focal length lens mounted between the vacuum window and the radiation shields has been designed for future use. With this lens twenty times more power can be focused on the sample if the radiation shield apertures

are widened to allow an acceptance angle of 9°.

The thermal background power P_b is estimated to be several microwatts in the present optical system with the cold shutter blocking all but the infrared port. Some of this power arrives at the sample after making multiple reflections from the surfaces of the shutter and radiation shields.

B. Absorption Signal

1. Small Signal Calculation

Energy conservation requires that the temperature of our sample assembly obey the equation

$$C\frac{dT}{dt} + G(T-T_H) = \eta(P_s + P_b + P_f e^{2\pi i f t}) + I^2 R_o e^{\Delta/T}. \qquad (13)$$

The left hand side is the power required to raise a body of heat capacity C to a temperature T greater than the heat sink temperature T_H. Power flows from the sample into the heat sink through a thermal conductance G. In our sample assembly G is determined by the thermal conductivity and dimensions of the thermometer's electrical leads. The right hand side of the equation gives the total power dissipated in the sample. The incident source power P_s and thermal background power P_b were estimated in the previous section. P_f is the component of the total spectrometer power modulated at frequency f. Its integral over frequency gives mP_s. The sample absorbs a fraction η of the incident radiation. In Chapter II we considered the dependence of η on the properties of the metal and surface layer. The final term in Eq. (13) is the joule heating in the thermometer crystal which has a

temperature dependent resistance $R = R_o e^{\Delta/T}$ and is biased with a current I from an external circuit.

Writing the temperature as the sum of a constant and a modulated term

$$T = T_o + T_f e^{2\pi i f t}$$

and expanding the exponential $e^{\Delta/T}$ to first order in $T-T_o$, we find that T_o and T_f obey the equations

$$G(T_o - T_H) = \eta(P_s + P_b) + I^2 R_o e^{\Delta/T_o} \tag{14}$$

$$T_f = \frac{\eta P_f}{G + \frac{I^2 R_o \Delta}{T_o^2} e^{\Delta/T_o} + 2\pi i f C} .$$

For low frequencies and bias currents the modulated temperature change T_f is the absorbed power ηP_f divided by the thermal conductance G. The amplitude of the temperature change decreases at high modulation frequencies falling to $1/\sqrt{2}$ of its DC value at the thermal relaxation frequency

$$f_o = \frac{G'}{2\pi C} , \tag{15}$$

where we have defined an effective thermal conductance

$$G' = G + \frac{I^2 R_o \Delta}{T_o^2} e^{\Delta/T_o} .$$

The signal voltage is the product of the bias current with the resistance modulation which arises from T_f. Keeping only the first order terms in T_f, the voltage amplitude is

$$V_f = S_f \eta P_f \ . \tag{16}$$

The responsivity S_f relates the signal voltage to the absorbed power ηP_f and is given by

$$S_f = \frac{IR_o \Delta e^{\Delta/T_o}}{T_o^2 G' (1 + f^2/f_o^2)^{1/2}} \ . \tag{17}$$

It is largest at low temperatures and for small thermal conductances. It increases with I for low bias currents and then falls for large I when the joule heating becomes excessive. Samples with large heat capacities have small relaxation frequencies and will not respond to fast infrared power modulations. To increase their frequency response, G must be made larger, and this reduces the signal amplitude. The sensitivity and frequency response required to detect surface absorptions can only be obtained at liquid helium temperature where heat capacities are much less than their room temperature values.

We have kept only first order terms in the derivation of the signal voltage and the result is valid only for small signals such that $T_f << T_o^2/\Delta$. For the data points recorded very near the spectrometer's zero path position, the changes in the absorbed power $\Delta P = m\eta P_s$ are too large for this condition to hold. A more accurate expression for the signal voltage takes the form

$$V = S\Delta P + S'(\Delta P)^2 + S''(\Delta P)^3 + \ldots .$$

The nonlinear terms generate sum and difference frequencies on the detected signal for every combination of frequencies present in the modulated spectrometer beam. The computed infrared spectrum can therefore contain false signals in regions of the spectrum where no absorption is expected. We do in fact observe such signals and their relative magnitude increases with applied power as expected.

The spectrum of the signal produced by detector nonlinearities is flat and contains none of the high resolution structure of the linear signal. This is because appreciable nonlinearities only occur very close to the zero path mirror position, and this effects only the low resolution features of the computed spectrum. High resolution features such as the atmospheric water vapor absorptions seen in Fig. 11 can be detected only if data are recorded far from the zero path point. In this region the response is quite linear.

2. Numerical Results and Measurement Procedures

Numerical values for the parameters which determine the signal amplitude in Eq. (16) are listed in Table 2 for the thin nickel film sample assembly used in our experiments. A few simple measurements are sufficient to obtain these approximate values.

The sample assembly is first immersed in a bath of liquid helium to calibrate its thermometer resistance. The bath pressure is reduced to produce the necessary range of sample temperatures. Between 1.5 K and 2.0 K values of R_o and Δ in the formula $R = R_o e^{\Delta/T}$ can be chosen to accurately fit the measured resistances. The calibrated sample assembly

Table 2. Sample Parameters

R_o	= 1320 Ω
Δ	= 9.43 K
T_H	= 1.688 K
I	= 2.0 μA
G	= 13 $(T_o+T_H)/2$ = 23.8 μW/K
R	= $R_o e^{\Delta/T_o}$ = 154.2 kΩ
T_o	= 1.955 K + I^2R/G = 1.981 K
ηP_b	= 0.69 μW
ηP_s	= 5.6 μW
f_o	= 265 Hz
C	= 1.5×10^{-8} J/K
S_f	= $\frac{2.9 \times 10^4}{(1+f^2/f_o^2)^{1/2}}$ V/W
f	= 500 Hz
m	= 0.29
V_{500}	= $\eta m P_s S_{500}$ = 22 mV

is then installed in the sample chamber and cooled to 1.6 K for the remaining measurements.

With all the feedthrough ports blocked by the cold shutter, the radiation incident on the sample is negligible and the measured sample temperature equals the heat sink temperature T_H. We use a 0.1 μA bias current in measuring the thermometer resistance and ignore an increase in the sample temperature of approximately 10^{-3} K caused by joule heating.

For larger bias currents the temperature change due to the bias current cannot be ignored, and its magnitude gives us an estimate of the thermal conductance G. With no incident radiation Eq. (14) reduces to

$$T_o - T_H = \frac{IV}{G} = \frac{\Delta}{\ln(V/IR_o)} - T_H \qquad (18)$$

where $V = IR_o e^{\Delta/T_o}$ is the voltage measured across the thermometer crystal. For the copper electrical leads which dominate the thermal conductance, we expect the linear temperature dependence $G = G_1 T$.[58] Since the conductivity varies with temperature along the length of the wire we substitute the average value $G = G_1 (T_o + T_H)/2$ into Eq. (18) and find

$$IV = \frac{G_1}{2} \left(\frac{\Delta^2}{\ln^2(V/IR_o)} - T_H^2 \right) .$$

With our measured values of R_o, Δ, and T_H we can calculate G_1 for each pair of measured currents and voltages. The result is found to increase with current and approach a constant value $G_1 = 13\ \mu W/K^2$ for

currents greater than 5 μA. For low currents G_1 approaches zero, and this indicates that our model of the thermal detection system is incomplete. It is thought that the thermometer resistance should include a current dependent contribution from the electrical contacts as well as a temperature dependent term from the germanium crystal. This contact resistance is only important at low bias currents and prevents us from accurately measuring G_1 in this range. The published thermal conductivity of the oxygen free high conductivity copper used for the thermometer's electrical leads is 1.3 μW/cm K at T = 2 K.[59] This gives a value for G_1 of 17 $\mu W/K^2$ which is in satisfactory agreement with our measurement.

The measured sample temperature rises from 1.688 K to 1.719 K when the infrared port in the radiation shield is opened and to 1.955 K when the unmodulated spectrometer beam is turned on. Using our value for G at these temperatures we calculate that 0.69 μW of thermal background radiation and 5.6 μW of infrared power from the spectrometer are absorbed. These are the values quoted for ηP_b and ηP_s in Table 2. The operating temperature T_o = 1.981 K for bias current I = 2 μA is found by adding a joule heating contribution I^2R/G to the temperature measured at I = 0.1 μA in the presence of the infrared beam.

Finally we determine the thermal relaxation frequency f_o by placing a rotating chopper blade in the infrared beam and measuring the amplitude of the sinusoidal absorption signal as a function of modulation frequency. We choose a value for f_o in Eq. (17) to fit the measured signals over the frequency range 50 Hz to 700 Hz. Our

values of f_o and G then determine the total sample heat capacity $C = G'/2\pi f_o = 1.5 \times 10^{-8}$ J/K.

By estimating the volume of each material in the sample assembly and using published heat capacities, we obtain a value of C which is almost twice as large as our measured value. This suggests that the measured value of G_1 may be too small. As a final test of the consistency of our measurements we calculate the sample's average absorption coefficient $\eta = 0.35$ from the measured value $\eta P_s = 5.6$ μW and the estimated value of incident power $P_s = 16$ μW. Figure 3a shows that this is the approximate value of η expected for nickel in the frequency band above 2000 cm^{-1} which includes 80 per cent of the radiation from our blackbody source.

The responsivity S_f calculated from the measured values of R_o, Δ, I, T_o, G, and f_o is 2.9×10^4 V/W at low modulation frequencies and falls to half that value at about 450 Hz. For our spectra covering the infrared frequency range 0-4000 cm^{-1} we use a mirror velocity of 0.12 cm/sec which produces modulation frequencies from 0 to 1000 Hz. We take 500 Hz as the average modulation frequency of our spectrum and calculate the interference signal V_{500} as if all the light were being modulated at this frequency. The modulation factor m = .29 is a third less than the measured value m = .44 because a third of the infrared radiation from our source lies above 4000 cm^{-1} (1000 Hz) and is electronically filtered from our signal. The calculated signal of 22 mV agrees with the measured signal voltage.

C. Random Noise Sources

To predict the sensitivity of our detection scheme, we need to know the amplitude of the noise which accompanies the signal voltage calculated above. Table 3 lists seven noise sources which are present in the system and gives the functional form of the mean square voltage for a one hertz detection bandwidth. The rms voltages are calculated from the numerical values in Table 2. They tell us the relative magnitudes of the different noise contributions for the detector and electronics described in Chapter III. Not included is noise introduced on the infrared signal by the spectrometer. This is discussed in Section IV-E.

The fundamental noise sources in Table 3 are inherent in a system which uses a resistance thermometer to detect power fluctuations.[60] The Johnson noise term gives the amplitude of the thermally induced voltage fluctuations present in any resistance R at finite temperature T_o. The thermal conductance noise arises from the mean square power fluctuations of magnitude $4kT_o^2G$ which occur when a body is coupled to a heat sink by a thermal conductance G. We multiply the expected power fluctuations by the responsivity S_f to find the noise voltage.

The radiation incident on the sample also fluctuates, and this accounts for the photon noise terms in Table 3. The standard results[60] for the power P and rms power fluctuations ΔP emitted in the forward direction by a blackbody source of area A are:

$$P = \frac{2A\Omega(kT)^4}{c^2h^3} \int_{x_1}^{x_2} \frac{x^3}{e^x-1}\, dx$$

Table 3. Noise Sources

Fundamental Noise Sources	Mean Square Voltage	RMS Voltage ($nV/\sqrt{Hz}$)
Johnson	$4kT_o R$	$V_{nj} = 4.1$
Thermal Conductance	$4kT_o^2 G S_f^2$	$V_{nG} = 1.0$
Source Photons	$8kT_s \eta P_s M_s S_f^2$	$V_{ns} = 10.4$
Background Photons	$8kT_b P_b M_b S_f^2$	$V_{nb} = 2.1$
Excess Noise Sources		
Thermometer	$7.8 \times 10^{-18} \frac{IR^2}{f(1+2.7\ 10^{10} I^2)}$	$V_{nt} = 25.8$
Amplifier	$9 \times 10^{-18} + 2.5 \times 10^{-35} f^2 R^2$	$V_{na} = 3.0$
Digitizer	$4.65 \times 10^{-10} \frac{(S_f m \eta P_s)^2}{f}$	$V_{nd} = 21.3$
Total Noise		$V_N = 35.5$

Numerical Values			
	$T_o = 1.981$ K	$M_s = .73$	$I = 2.0$ μA
	$R = 154$ kΩ	$\eta P_s = 5.6$ μW	$m = .29$
	$G = 23.8$ μW/k	$M_b = 1.0$	$S_f = 1360$ V/W
	$T_s = 1300$	$\eta P_b = .69$ μW	$f = 500$ Hz

$$(\Delta P)^2 = \frac{4A\Omega(kT)^5}{c^2h^3} \int_{x_1}^{x_2} \frac{x^4 e^x}{(e^x-1)^2}\, dx$$

where Ω is the solid angle collected from the source, c is the speed of light, and h is Planck's constant. The integration variable is $x = h\nu c/kT$ where ν is the infrared frequency in cm^{-1}. The integration limits correspond to the upper and lower frequency limits of the radiation being measured. Combining the two equations we get

$$(\Delta P)^2 = 8kTPM$$

where

$$M = \frac{\int_{x_L}^{x_H} \frac{x^4 e^x}{(e^x-1)^2}\, dx}{4\int_{x_L}^{x_H} \frac{x^3}{e^x-1}\, dx} .$$

In this chapter we evaluate the sensitivity of absorption spectroscopy in the two infrared spectral bands 0-1000 cm^{-1} and 0-4000 cm^{-1}. For the low frequency band the integral has the value $M_s = 0.36$ for the source radiation and $M_b = 0.77$ for the room temperature thermal background radiation. For the high frequency band we get $M_s = 0.73$ and $M_b = 1.0$. Radiation from the cold surfaces in the sample chamber contributes very little to the photon noise, so we have not included the additional terms in Table 3.

The fundamental noise sources determine the ultimate limit to the sensitivity of our experiment. In the present system excess noise from the thermometer element and the digitizing electronics prevent us from reaching this limit. Figure 14 shows the measured audio frequency

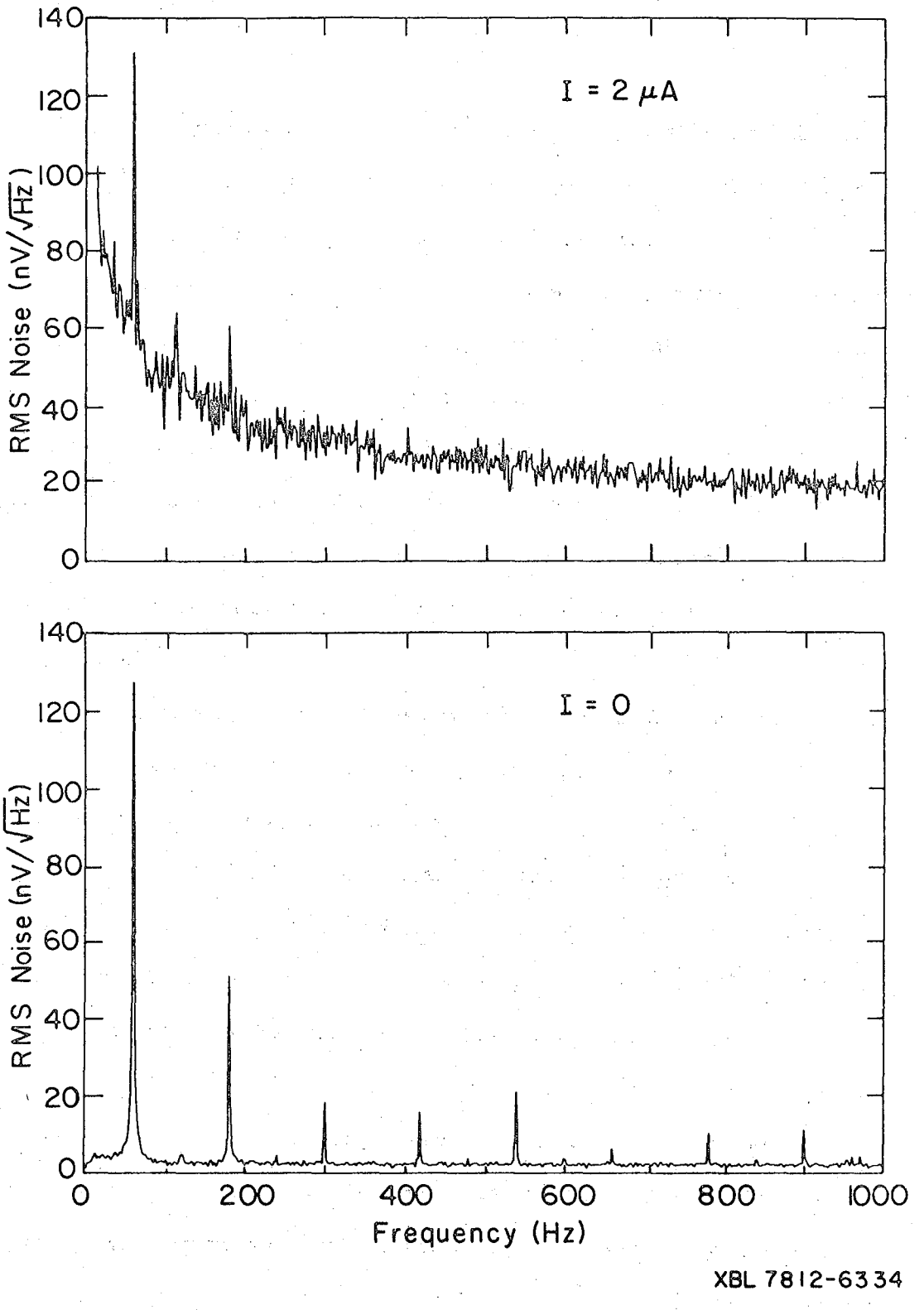

Fig. 14. Noise spectra of sample thermometer.

noise spectrum of the thermometer signal for two different bias currents with no radiation incident on the sample. For I=0 the responsivity S_f vanishes, and the Johnson noise and amplifier noise produce a frequency independent noise spectrum. Sharp peaks at the harmonics of 60 Hz measure the amount of electrical pickup from AC power lines. For I=2 μA a frequency dependent noise appears. It is too large to come from any of the fundamental sources so we conclude that there is an extra noise mechanism associated with current flow through the thermometer or its contacts. The empirical expression in Table 3 for the mean squared thermometer voltage noise is accurate to about 30% for the range of currents 0-10 μA and resistances 0.1 to 0.5 MΩ encountered in our experiments with this detector.

To the noise voltages on the detector signal we must add contributions from the amplifier and digitizing electronics shown in Fig. 12. Our expression for the amplifier noise in Table 3 is the equivalent input noise for the PAR 185 preamp. It fits the published noise data[61] for the frequencies and resistances of interest. The amplifier gain is set to the value $10/V_f$ to give a 10 volt output signal when the input signal has its peak value $V_f = m\eta P_s S_f$.

To determine the effect of the sample-and-hold amplifier and analog-to-digital converter (ADC) on the noise level, we reduce the input signal to zero. The computed noise spectrum then approaches a constant value, independent of the input signal, which we call the digitizing noise. Each point in the digitized data record is uncertain by approximately 305 μV, the voltage resolution of the ADC. In effect

the ADC has added a random noise voltage of rms value 305 μV and bandwidth Δf to the input signal. The frequency spectrum of this excess noise should then be flat and have magnitude $305/\sqrt{\Delta f}$ μV/$\sqrt{Hz}$. The measured spectrum in the absence of an input signal confirms this simple picture of ADC noise. To compare it with the other noise voltages, which were all evaluated at the input of the preamplifier, we divide this digitizing noise by the gain and get

$$V_{nd} = \frac{30.5\ m\eta P_s S_f}{\sqrt{\Delta f}}\ \mu V/\sqrt{Hz}\ .$$

If the infrared frequencies of interest are modulated at frequency f, then we typically detect a band of frequencies of width Δf = 2f. Our formula for the digitizing noise in Table 3 is for this case.

D. Calculated Noise

In Chapter II we calculated the fractional change in the absorption signal produced by different surface coverages of carbon monoxide molecules. To estimate the minimum detectable coverage we now derive an expression for the fractional noise on an absorption spectrum.

Consider a spectrum covering the infrared band 0 to 2ν where ν is the frequency of primary interest. A rapid scan Fourier spectrometer will modulate this radiation at audio frequencies from 0 to 2f where f = 2vν and v is the mirror velocity. We use the average modulation frequency f to calculate the peak interferogram voltage $V_f = m\eta P_s S_f$ which is a measure of the total power in the infrared beam. If this power is distributed uniformly over the spectrum, then the signal voltage in the narrow frequency band Δν is $V_f\ \Delta\nu/2\nu$. The noise in

the band is $V_N\sqrt{\Delta f}$, where V_N is the sum of all the noise terms in Table 3 and $\Delta f = f\,\Delta\nu/\nu$. The fractional noise on the spectrum is

$$F = \frac{V_N\sqrt{\Delta f}}{V_f\,\Delta\nu/2\nu} = \frac{V_N}{V_f}\sqrt{\frac{4f\nu}{\Delta\nu}}\,.$$

This noise increases as we decrease $\Delta\nu$ and look for high resolution features. It also increases with modulation frequency because for high mirror velocities less time is spent measuring an interferogram. Taking the signal V_f and noise V_N from Tables 2 and 3 and using f = 500 Hz, ν = 2000 cm^{-1}, and $\Delta\nu$ = 2 cm^{-1}, we calculate a fractional noise of 0.0023 for a single spectrometer scan.

To improve the sensitivity we average many interferograms before calculating the frequency spectrum. The time required for the spectrometer mirror to complete a cycle of motion and produce a new interferogram is

$$t_s = \frac{L}{v} + \frac{L}{v'} + t_r\,,$$

where L is the distance traveled by the mirror, v is the mirror velocity during data acquisition, v' is the velocity in the reverse direction, and t_r is the time required to change directions twice. In Fourier spectroscopy the scan length L required for a spectral resolution $\Delta\nu$ is $L = 1/4\Delta\nu$.[54] Using this expression and the measured values v' = 2 cm/sec and t_r = 0.8 sec we get

$$t_s = \frac{\nu}{2\Delta\nu f} + \frac{1}{8\Delta\nu} + 0.8 \text{ sec.}$$

In a one hour measurement the number of interferograms accumulated is $3600/t_s$, and the noise is reduced by the square root of this number. The resulting expression for the fractional noise is

$$F = \frac{V_N}{30V_f}\left(\frac{f\nu t_s}{\Delta\nu}\right)^{1/2} = .012\,\frac{V_N\nu}{V_f\Delta\nu}\left(\frac{4\nu + f + 6.4f\,\Delta\nu}{\nu}\right)^{1/2}. \qquad (19)$$

In our numerical example 1900 interferograms are averaged in an hour and the fractional noise is 5.2×10^{-5} or 52 parts per million (ppm).

The independent parameters entering Eq. (19) for the fractional noise are R_o, Δ, T_H, C, G, η, P_b, P_s, m, I, f, ν, and $\Delta\nu$. For each set of variables, Eq. (14) is first solved for the operating temperature of the sample, and then F can be evaluated from Eqs. (16) and (19) and the formulas in Table 3. For even a single set of parameters this is a lengthy procedure. We therefore resort to computer calculations to systematically vary the parameters and minimize the fractional noise for a particular experiment.

There are two important limiting cases in which the fractional noise is independent of the properties of the sample and therefore easy to calculate. Table 3 shows that the digitizer noise is proportional to the modulated infrared power $m\eta P_s$. For sufficiently large signals it will be the dominant term. Ignoring all other contributions we find that the digitizing noise limit is

$$F_d = 7.2 \times 10^{-7}\left(\frac{\nu t_s}{\Delta\nu}\right)^{1/2}.$$

Again we use $\nu = 2000\ cm^{-1}$, $\Delta\nu = 2\ cm^{-1}$, and f = 500 Hz and find that the fractional noise is 31 ppm. If excess noise from the thermometer and electronics can be eliminated, then for large infrared signals source photon noise will be the only important term. The source noise limit is

$$F_s = \frac{.096}{m} \left(\frac{kT_s M_s f \nu t_s}{\eta P_s \Delta\nu} \right)^{1/2}$$

and is 15 ppm in our example. In Section IV-A we noted that improved optical efficiency could increase the absorbed power by a factor of 20 to approximately 100 μW. The source noise limit is then 3.5 ppm.

Our computer calculations using all the noise contributions in Table 3 show that the present detector is nearly optimum for an experiment with 5.6 μW of absorbed power in the spectral band 0-4000 cm^{-1}. If the absorbed power increases to 100 μW the thermal conductance parameter G_1 must be raised from 13 to 500 $\mu W/K^2$ to keep the sample cold and to minimize its fractional noise. This power level is adequate to achieve the digitizing noise limit of 31 ppm. If excess noise from the thermometer and electronics are eliminated, the source noise limit of 3.5 ppm is approached. This high thermal conductance, low heat capacity sample has a relaxation frequency f_o = 13 kHz which is 20 times larger than the modulation frequencies produced by the spectrometer. If we increase the sample's heat capacity to 10^{-6} J/K, corresponding to a 30 μm thick nickel crystal, then the relaxation frequency drops to 200 Hz. The total noise is then only 10 per cent larger than for the present low heat capacity sample. This demonstrates

that the thermal detection technique is not limited to thin evaporated film samples. A nickel sample 30 μm thick can probably be ground from a thicker single crystal. Thinner single crystals have been grown epitaxially on alkali halide substrates.[62,63]

In Chapter II we found that infrared absorption by a nickel sample is smallest in the spectral region below 1000 cm^{-1}, and it is here that the absorption technique has its greatest advantage over reflection spectroscopy. Our calculations show that for 2 μW of absorbed power, a 2 cm^{-1} resolution, and a 30 μm thick sample, the total fractional noise is 35 ppm. The sensitivity is virtually the same as in the high frequency band in spite of the fact that only five per cent of the total infrared power from our source lies below 1000 cm^{-1}.

E. Measured Noise

Our estimates of the sensitivity of absorption spectroscopy have so far included only those noise sources known from theoretical arguments to be present or those actually observed on noise spectra measured with the spectrometer modulation turned off. In the presence of spectrometer modulation there may be additional noise, and the only way to detect it is to compare noise levels on the measured absorption spectra with the predictions of the previous section.

Our data analysis program, in addition to computing and plotting each spectrum, calculates the average signal and the rms deviations fom the average for a specified band of frequencies. The absorption spectrum of Fig. 11 shows that the variations will be large in spectral regions where there are atmospheric water vapor absorptions or other

structure on the transmission function of the spectrometer. Focusing on the spectral region 2400-2500 cm^{-1}, where the structure is smallest, we find after subtracting away the slope that there remains a fractional rms variation of approximately 500 ppm on a typical spectrum measured with a resolution of 2 cm^{-1}. Some of this structure is reproducible and cancels when a reference spectrum of the clean metal surface is subtracted. The lowest rms noise observed in a difference spectrum was 87 ppm. Usually however, it was several times larger and often it increased or decreased monotonically in a sequence of spectra recorded on the same day. The random component of the noise on the signal and reference spectra is less by a factor $\sqrt{2}$ than what we measure in their difference. Our best spectra therefore had rms variations of about 62 ppm of the baseline signal, and this is only slightly larger than the estimate of 52 ppm made in the previous section. We attribute the additional noise to instabilities in the output signal of the spectrometer. In the quietest spectra these instabilities contribute a noise voltage which is only a fraction of the total noise calculated from Table 3. However in most spectra the spectrometer noise is larger and is the factor which limits the sensitivity of an experiment.

Some of the structure in the frequency spectrum of the spectrometer signal may be interference effects caused by multiple reflections in the beamsplitter and other optical components. Variations in this structure will occur if the optical alignment is sensitive to slow temperature changes or to vibrations. This could account for some of the observed noise. More experimentation will be required to determine

the exact source of the excess spectrometer noise and to reduce it to a consistently low level.

F. Sensitivity of Absorption Spectroscopy

The peak-to-peak variations on our measured spectra are roughly four times larger than the calculated rms noise. An absorption line must therefore have a peak amplitude of about 350 ppm to be detected in a difference spectrum having an rms noise of 87 ppm. The calculated and measured peak height for a monolayer of randomly oriented, physically adsorbed CO with a 6 cm^{-1} linewidth was shown in Chapter II to be about 2.5 per cent of the background absorption by the nickel film. This is 71 times larger than the minimum detectable signal. Chemisorbed CO molecules are oriented perpendicular to the surface, and we show in Chapter V that their infrared absorption appears to be enhanced by the interaction with nickel atoms. Both factors lead to a larger total signal, however the absorption by chemisorbed molecules is spread between several broader spectral lines so that the peak height and signal-to-noise ratio are comparable to those observed for physically adsorbed molecules.

The signal and noise amplitudes discussed above are expressed as a fraction of the background absorption signal from the metal surface. To compare them with the amplitudes reported in reflection spectroscopy, we multiply by the absorption coefficient of the metal and express them as a fraction of the total incident radiation. The calculated absorption by a cold nickel film at an angle of incidence of 82°, a frequency of 2000 cm^{-1}, and averaged over the two polarization states is shown in

Fig. 2a to be about 0.15 of the incident power. The lowest peak-to-peak noise level seen in a difference spectrum therefore corresponds to an absorption of 53 ppm of the unpolarized incident beam. The best published infrared reflection spectra of metal surfaces are those of Bradshaw and Hoffman,[64] and they show peak noise levels of approximately 200 ppm or larger. These spectra appear to have been recorded more quickly than ours but at lower resolution and over a narrower band of frequencies. Direct comparison of the sensitivity in the two experiments is therefore difficult. However, the potential of the absorption technique is clearly demonstrated. In the early stages of its development, it has produced vibrational spectra of metal surfaces with greater sensitivity, higher resolution, and a broader bandwidth than any previous infrared measurement.

The first priority in the future development of our apparatus is to stabilize the intensity and spectral characteristics of the radiation incident on the sample from the spectrometer. The sensitivity will then be limited by the thermometer and digitizing noise. We believe that the excess thermometer noise can be reduced by improving the electrical contacts to the germanium crystal or by using thermometer elements of another type. Digitizing noise can be reduced by switching the amplifier gain to a larger value after the interferogram signal has passed through its maximum amplitude at the position of zero optical path difference. Elimination of all the excess noise sources was shown in Section IV-D to reduce the total noise by a factor of 10.

V. EXPERIMENTS ON NICKEL FILMS

A. Chemically Adsorbed Carbon Monoxide

In this section we present a series of infrared spectra of evaporated nickel films which show how the adsorption state of carbon monoxide changes with temperature and surface coverage. For small CO concentrations our results are consistent with recent electron energy loss and infrared spectra of room temperature single crystal samples. By extending our measurements to lower temperatures and higher coverages than have previously been studied, we observe new effects which demonstrate the importance of repulsive forces between neighboring molecules in determining the distribution of molecules among the available adsorption sites.

1. Experimental Procedures and Results

The construction and mounting of the sample assembly for metal film experiments and the design of the evaporation source are described in Chapter III. The films studied must be several thousand angstroms thick to prevent infrared radiation from being transmitted to the strongly absorbing Al_2O_3 substrate. Approximately 2000 Å of copper were first deposited from the crucible source. The nickel plated tungsten filament source was then installed in the vacuum chamber and thoroughly outgassed before baking the system and beginning the series of infrared measurements described in this chapter.

For each experiment on chemisorbed carbon monoxide a thin nickel film was first evaporated over the existing thick deposit. The evaporation was begun with the cryostat at liquid nitrogen temperature

and the system pressure at 9×10^{-11} torr. The filament was heated over a one hour period to the evaporation temperature. During this interval the sample was masked by the cold shutter and could be maintained at any temperature between 77 K and 400 K by adjusting the heater current. Five minutes were required to deposit approximately 200 Å of nickel on the sample. The system pressure during the evaporation rose to 10^{-9} torr. The pressure increase at the position of the sample was probably smaller since this region is screened from the heated surfaces of the evaporator by cold radiation shields. When the evaporation ended, carbon monoxide gas (Matheson, 99.5% purity) was immediately introduced through the leak valve to maintain a constant system pressure on the order of 10^{-5} torr. The liquid helium transfer then began. As soon as the cryostat temperature dropped below 77 K, the leak valve was closed to end the gas exposure, and the sample heater was turned off. The system pressure then decreased immediately to 10^{-9} torr and over a period of hours to 10^{-10} torr.

By maintaining a high CO gas pressure during the five minute interval between the end of the evaporation and the beginning of the liquid helium transfer, we achieve a high equilibrium surface coverage of carbon monoxide. The gas is pumped out as the temperature of the cryostat begins to drop in order to prevent multilayer condensation which occurs on surfaces below 40 K. When the heater is turned off, the sample cools to 77 K in a few seconds and reaches liquid helium temperatures a few minutes later. Desorption and surface diffusion rates for adsorbed molecules fall very rapidly as the sample temperature

decreases. The chemical state formed on the sample surface during the gas exposure therefore changes very little during the helium transfer and not at all during the infrared measurements made at 2 K.

Figure 15 shows four infrared spectra of a nickel film evaporated and then exposed to 2×10^{-5} torr of CO at a sample temperature of 77 K. The initial spectrum, labeled T = 77 K, is characteristic of the surface state formed during the gas exposure. Three more spectra of the same sample were measured after heating the crystal to successively higher temperatures for one minute intervals. Each measurement is the average of 1000 spectrometer scans and required approximately one hour to complete. The temperature was monitored by the copper-constantan thermocouple soldered to the sample crystal. The CO molecules were removed from the metal film via argon ion bombardment (Section III-A-2), and a spectrum of the clean nickel surface was then recorded. In Fig. 15 this background spectrum has been subtracted from each of the CO spectra to distinguish the molecular absorptions from other spectral features. Sharp water vapor lines appear in the difference spectra because the concentration of water vapor in the spectrometer changed during the course of the measurements. Comparison with published high resolution water vapor spectra[67] show that the calibration derived from the wavelength of the reference laser is accurate to 0.5 cm^{-1} and that the resolution is approximately 2 cm^{-1}.

The carbon monoxide absorptions labeled A, B, and C are due to molecules bonded on the surface to one, two, and three nickel atoms respectively. The identification of these spectral lines is based

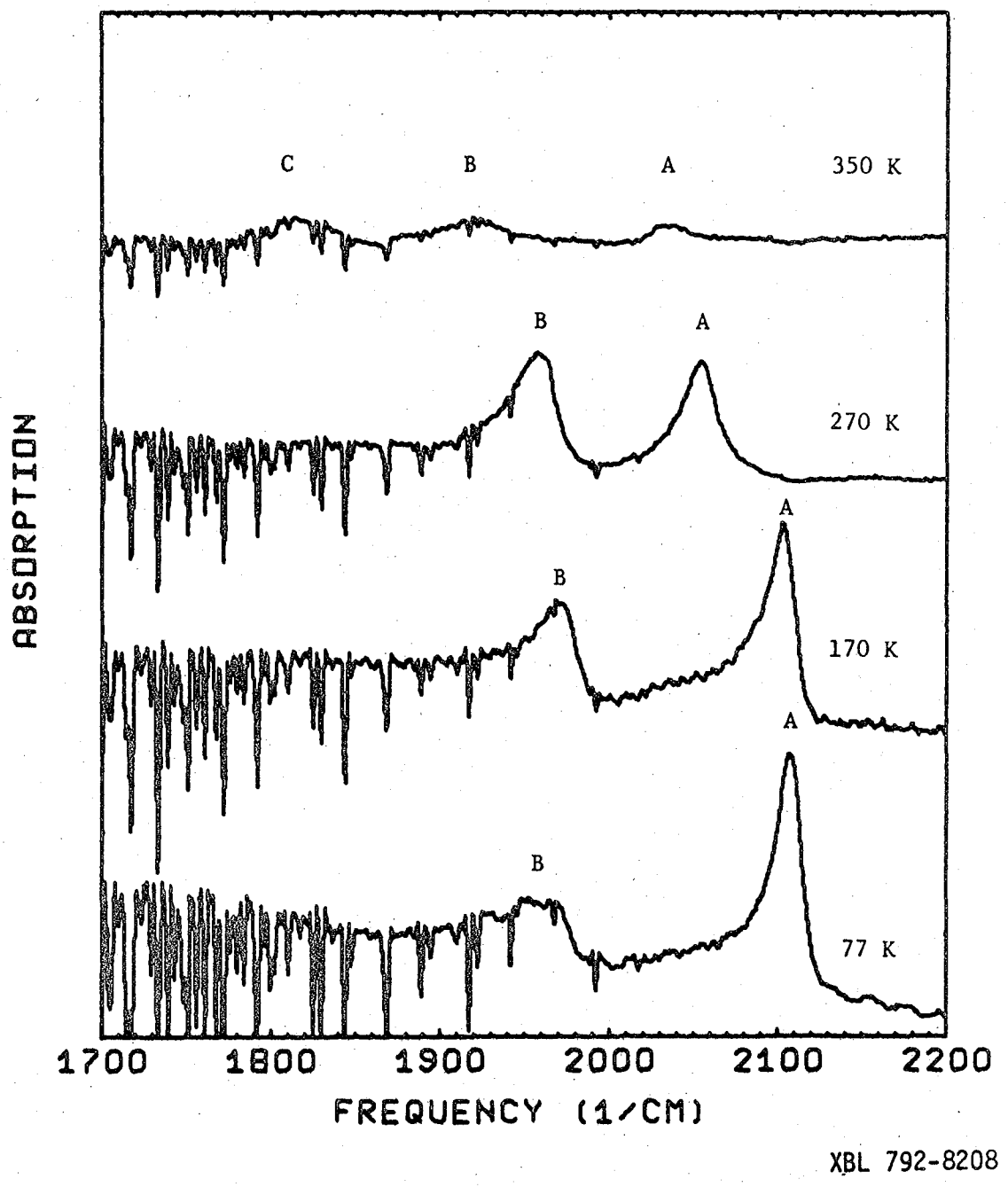

Fig. 15. Spectra of CO adsorbed on a nickel film at 77 K and then heated to successively higher temperatures.

upon the results of previous experiments which are summarized in the next section. Bonds involving one nickel atom are called linear bonds while those linking the CO molecule to two or more nickel atoms are called bridge bonds. The integrated strength of the three lines decreases as the sample is heated and molecules desorb from the surface. The dependence of the spectrum on temperature and surface coverage is shown in more detail in Fig. 16 which combines the results of experiments on three different nickel films. The spectra labeled (a), (c), (e), and (f) are from Fig. 15. Spectrum (d) is for a film evaporated and exposed to 5×10^{-6} torr of CO at 290 K. The same film heated to 310 K for three minutes produced spectrum (b). The sample in spectrum (g) is a film cleaned by ion bombardment at 300 K, exposed to a total flux of 1.5×10^{16} molecules/cm^2 at 2 K, and then heated to 29.3 K for two minutes to remove most of the physically adsorbed CO. The spectra are arranged from (a) to (g) in order of increasing surface coverage. Gas exposures made at the lowest sample temperatures were assumed to produce the highest coverages. Spectra (b) and (d) are positioned relative to (a), (c), and (e) by assuming that the frequency of line A increases monotonically with coverage. The frequency ν, linewidth $\Delta\nu$, peak signal F, and integrated strength $I = \int F \, d\nu$ for each line are listed in Table 4. The signal strength F is taken as the ratio of the peak carbon monoxide absorption to the baseline absorption from the clean nickel film. The vertical scale in Fig. 16 is calibrated by assuming that the metal absorbs 15 per cent of the total incident unpolarized radiation (Section II-D).

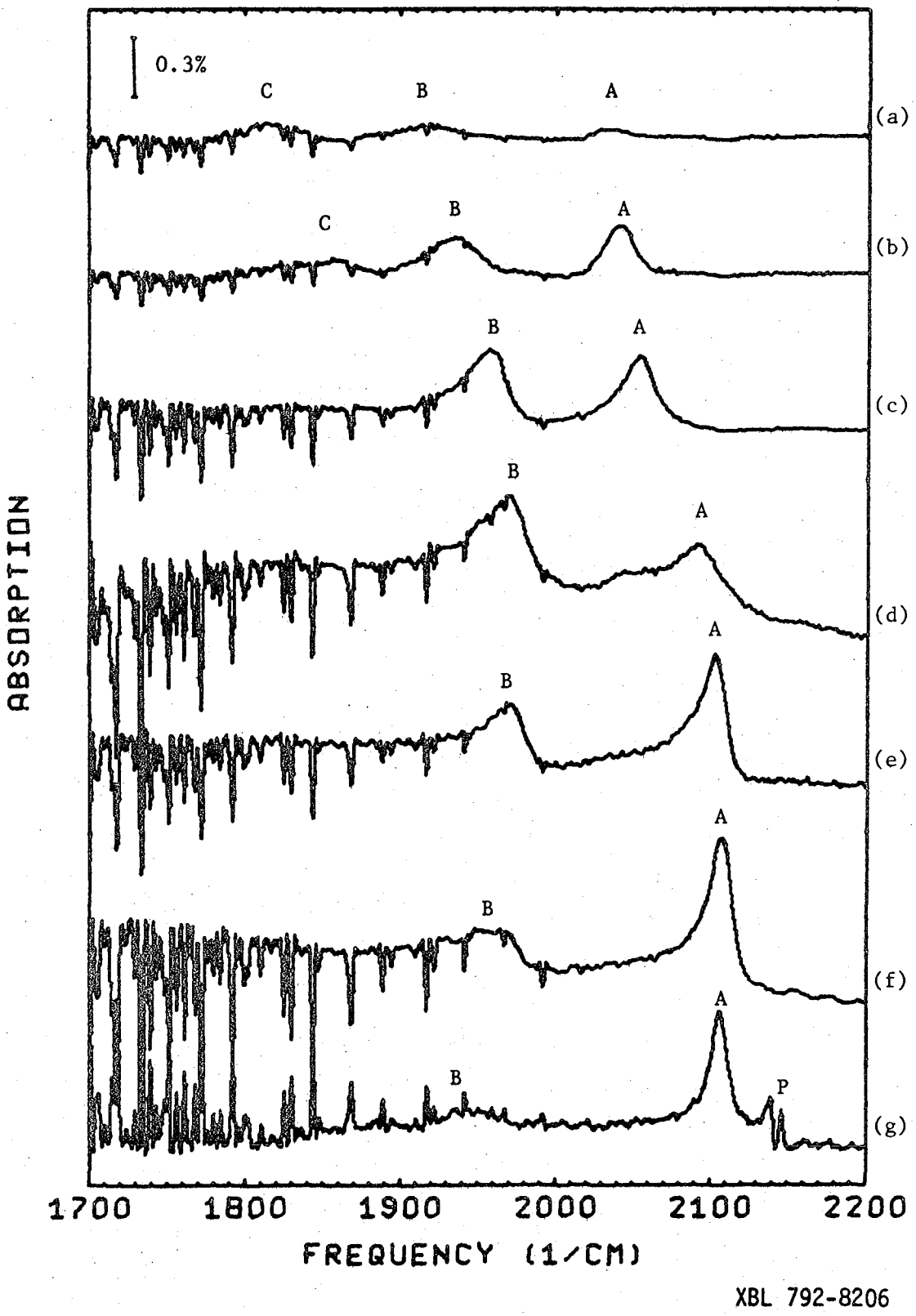

Fig. 16. Compilation of spectra of CO adsorbed on three different nickel films.

Table 4. Line Strengths, Positions, and Widths from Fig. 16.

Spectrum	(a)	(b)	(c)	(d)	(e)	(f)	(g)
Line A							
ν	2036	2041	2054	2092	2103	2107	2106
$\Delta\nu$	26	22	24	33	22	20	14
F	.0024	.0119	.0173	.016	.031	.038	.030
I	.062	.26	.42	.76	.87	.98	.42
Line B							
ν	1919	1937	1958	1970	1971	1964	1949
$\Delta\nu$	43	34	26	37	28	30	23
F	.0031	.0093	.0173	.021	.0138	.0090	.0032
I	.13	.32	.61	.84	.55	.46	.07
Line C							
ν	1815	1858					2000
$\Delta\nu$	43	43					270
F	.0041	.0038					.0048
I	.18	.16					1.28
I_{Total}	.37	.74	1.03	1.60	1.42	1.44	1.77

In the sections which follow we will analyze in detail the sequence of spectra in Fig. 16. First we review the results of previous experimental and theoretical investigations of carbon monoxide adsorption and identify the absorption lines in our spectra with those detected on both single crystal and polycrystalline samples. We then discuss the structure of our evaporated film sample, the thermally activated transitions which can occur between different bonding states, and the effects of intermolecular repulsion on the distribution of molecules among the available adsorption sites. Finally we compare the measured intensities and frequency shifts with those predicted by the simple dipole model of Chapter II.

We will find that most of the features of our spectra can be explained in terms of the fairly well established picture of linear and bridge bonded molecules. Spectra (a) through (d) are consistent with published results for room temperature single crystal and catalyst samples. The absorption lines shift to higher frequencies with increasing surface coverage because of the dipole-dipole interactions between adsorbed molecules. Because only molecules with the same vibrational frequency are coupled together by this effect, line B shifts back to lower frequencies in spectra (d) through (g) as the number of molecules at bridge sites decreases. The relative intensities of lines A and B change as molecules make transitions to different bonding sites. We will consider three effects which might cause these transitions. First, there is the possibility that the surface states formed at low temperatures do not represent equilibrium distributions of

molecules and that thermally activated transitions between linear and bridge sites occur when the sample temperature is raised. Next, we will show that interactions between adsorbed molecules can change the relative energies of the two bonding configurations and make linear bonds more stable at high coverage. Finally we will discuss direct intermolecular repulsion which can force molecules to occupy less stable sites of intermediate bond character. Future experiments in which the temperature and surface coverage are varied independently of each other will be necessary to determine the relative importance of each effect.

2. Summary of Previous Work

The infrared spectra of polycrystalline metal samples are discussed in more detail elsewhere.[8,68] Catalyst samples consist of metal crystals between 20 and 200 Å in diameter which are chemically deposited on high surface area silica or alumina. Common features of most spectral measurements of CO on nickel catalysts are strong absorptions at the approximate positions of lines A and B in Fig. 16. The lines are generally broader than we observe with measurable absorption occurring out to 1800 cm^{-1}. At low coverages the absorption below 1900 cm^{-1} appears as a distinct band (line C) whose intensity is comparable to that of the two high frequency bands. The details of the measured spectra are effected by the structure and chemical pretreatment of the metal particles,[69,70] by the composition of the supporting medium,[71] and by impurities. Previous infrared experiments on nickel films evaporated in ultrahigh vacuum detected the principal

absorption lines but were not sensitive enough to record spectra over a range of different coverages.[72]

The spectra of adsorbed carbon monoxide were first interpreted by Eischens, et al.,[7] on the basis of the measured spectra of carbonyl compounds in which CO groups are bonded through their carbon atoms to one or more transition metal atoms. Absorptions above 2000 cm^{-1} occur for "linear" bonds linking the CO molecule to a single metal atom. The low frequency lines arise from "bridge" bonds to two or more metal atoms. Photoemission experiments have confirmed that the axis of the CO molecule is oriented perpendicular to the (100) and (111) nickel faces and that the carbon atom is closest to the surface.[73] Recent measurements of the saturation magnetization of nickel catalyst samples support the picture of linear and bridge bonds on surfaces.[69] In these experiments a single nickel conduction band electron was found to participate in the linear chemical bond associated with the 2070 cm^{-1} infrared absorption. Two electrons participated in the bridge bond producing the signal at 1930 cm^{-1}. Studies of compounds of the form $Ni_n(CO)_m$ assign the absorption near 1930 cm^{-1} to a two center bond Ni_2CO while lower frequencies are associated with three and four center bonds.[74]

Blyholder[75] has proposed an alternative interpretation of the spectra of adsorbed carbon monoxide in which linear bonds to metal atoms located at the edges and corners of crystal planes account for the absorptions below 2000 cm^{-1}. Evidence for this is found in the spectra of nickel catalysts.[70] Samples with the smallest metal

particles have the highest concentration of edge and corner sites and the most prominent infrared absorption near 1800 cm^{-1}. It has also been found that CO molecules adsorbed on the edge sites of stepped single crystals are the first to dissociate as the temperature is increased.[76] The weakened C-O bond at these adsorption sites is indirect evidence for a low vibrational frequency.

Although edge and corner sites may produce some of the low frequency absorptions seen in polycrystalline samples, their concentration is too small to account for the strong lines detected below 2000 cm^{-1} on well ordered single crystal surfaces. These lines must be attributed to the bridge bonded molecules proposed by Eischens. For small coverages of CO on Ni(100) at 173 K, Andersson[77] has observed electron energy loss vibrations at 1930 cm^{-1}, 656 cm^{-1} and 358 cm^{-1}. The low frequency modes are identified as the symmetric and asymmetric Ni-C stretching vibrations expected for the Ni_2CO surface species. The C-O stretching vibration at 1930 cm^{-1} is in the expected position for a molecule bonded to two nickel atoms. Warming the sample to 293 K caused the vibrations of linearly bonded CO to appear at 2062 cm^{-1} and 479 cm^{-1} along with the bridge bond modes. Apparently the energy difference between the two bonding configurations is small enough that excitations into the linear state are possible at room temperature. This is inconsistent with calculations done on Ni(100) which predict a much larger energy difference on the order of an electron volt.[78,79]

When the surface coverage on Ni(100) is increased to $\theta = 0.5$ (one CO for every two Ni), a c(2×2) LEED pattern develops,[80] and the

energy loss spectrum shows only the presence of linearly bonded carbon monoxide.[77] Intensity analysis of the LEED data also favors the linear bonding site.[81] Adsorption energies are apparently modified to favor the linear bond when the spacing between molecules decreases, and an ordered array is formed.

The CO vibration at low coverage on Ni(111) has been detected near 1815 cm^{-1} in both ELS[82] and infrared experiments.[83] The low frequency is evidence that molecules occupy the hollow sites on the close packed lattice and are bonded to three nickel atoms. The energy loss signal shifts to 1911 cm^{-1} at $\theta = 0.41$,[82] suggesting that a conversion from three center to two center adsorption sites has occurred. More detailed infrared spectra have been reported by Bradshaw and Hoffman[64] for CO on Pd(111), a system which shows virtually the same LEED patterns and vibrational frequencies as Ni(111). The spectral line is observed to broaden during the transition between sites and to narrow again when the transition is completed. The large frequency shift due to bond conversion occurs over a narrow range of surface coverages. Additional shifts to higher frequencies occur continuously as the coverage increases. These shifts have been attributed to dipole-dipole interactions between molecules,[46] to the overlap of molecular wavefunctions,[64] and to indirect interactions between molecules due to their competition for bonding electrons from the substrate.[47,75,84] Theoretical work on interactions mediated by the substrate show that such effects can contribute to the stability of the ordered structures observed at high coverage.[85]

3. Identification of Spectral Lines

The results of ELS and infrared experiments outlined in the previous section demonstrate that lines A, B, and C in our low coverage spectra are due to molecules occupying linear, two center, and three center adsorption sites respectively. Bonds formed at four center sites may also be stable on certain planes and contribute to either line B or line C. In spectra (a) and (b) of Fig. 16, line C corresponds to the vibrational mode observed at low coverage on Ni(111).[82,83] For the room temperature saturation coverage achieved in spectrum (d), the (111) absorptions are expected at 1915 and 2045 cm^{-1} where they account for some of the intensity in lines B and A.[83] Energy loss peaks on Ni(100)[77] were found at 1930 and 2062 cm^{-1} and can be identified with lines B and A in spectra (a) through (d). The ELS experiments indicate that most of the (100) signal should be in line B at low coverage, in line A at $\theta = 0.5$, and spread between the two at $\theta = 0.61$. Since this behavior is not apparent in our spectra, we conclude that the surface of our polycrystalline sample cannot be treated as a collection of perfectly ordered (111) and (100) faces. Data on other nickel surfaces are not available.

The spectral lines in Fig. 16 shift to higher frequencies as the surface coverage increases. We show below that dipole-dipole coupling between molecules vibrating at the same frequency accounts for most of the observed effect. The frequency shift increases approximately linearly with surface coverage. The splitting of line A in spectrum (d) is evidence that linear bonds are present in different concentrations

on the different crystal faces of our sample. For example, the weak low frequency component of line A might arise from a small concentration of linear bonds on the (111) faces, which are expected to contain mostly bridge bonds.[82] The stronger high frequency component could then be attributed to the large concentration of linear bonds expected on (100) faces.[77]

Spectra (e), (f), and (g) in Fig. 16 represent high surface coverage states which have not been studied in previous experiments. Because intermolecular repulsion greatly reduces the net binding energy of the molecules for surface concentrations greater than approximately 10^{15} molecules/cm^2 (θ = 0.53 on Ni(111) or θ = 0.69 on Ni(100)),[92] such states are stable only at low sample temperatures. Spectra (e) and (f) show that as the coverage increases line A shifts to higher frequencies and grows at the expense of line B. Spectrum (g) shows, in addition to lines A and B, a broad absorption between 1850 and 2150 cm^{-1}. We attribute it to molecules adsorbed at random positions relative to the nickel lattice. These high coverage spectra will be interpreted below in terms of the bonding forces exerted on the CO molecules by the nickel lattice and the repulsive forces between neighboring molecules.

4. Structure of the Nickel Film

Metal films deposited on most substrates at or below room temperature consist of randomly oriented crystal domains having the lattice structure of bulk single crystals.[86] Grain sizes between 60 and 300 Å have been measured for nickel films,[87,88] and most of the exposed

surface area is expected to consist of low index faces. The surface structure therefore resembles that of catalyst samples. Poor vacuum conditions and smaller domain sizes probably account for the broader linewidths observed in experiments on nickel catalysts.[8,70] There is no evidence in our high coverage spectra of the broad absorption band below 1900 cm^{-1} which has been attributed to CO molecules bonded at the edges and corners of crystal faces in nickel catalyst samples.[70] The only effect of substrate disorder which we observe is a slight broadening of the CO absorption lines on ion bombarded surfaces relative to the lines seen at similar coverages on freshly evaporated films. This is evidence that the CO stretching frequency is determined primarily by the number of nickel atoms directly bonded to the molecule and not by the arrangement of the nickel atoms surrounding the adsorption site.

The spectra of molecules adsorbed on polycrystalline samples are more complicated than those of single crystals because a larger variety of different adsorption sites are present. A further difficulty with evaporated nickel films is that the samples are porous so that the surface area available for the adsorption of gases is larger than the geometrical area of the film.[88,89] The interior surfaces occur at the boundaries between crystal domains and are oriented approximately perpendicular to the plane of the film. CO molecules chemisorbed on these faces will therefore have their axes parallel to the plane of the film, and they will not interact with the electric fields of the incident infrared radiation which are polarized perpendicular to the film and penetrate into the film due to the skin effect.[40] Radiation

does not propagate directly into the cracks in the film because their widths are much smaller than the infrared wavelengths. Consequently, only the molecules adsorbed on the outer faces of the sample should contribute significantly to the measured absorption signal. Prolonged annealing at temperatures above 300 K is required to reduce the porosity of a nickel film and increase its average grain size.[89,90] This tells us that nickel atoms diffuse across the surface much more slowly than the adsorbed carbon monoxide molecules, which are highly mobile at room temperature.[80] The changes in our measured spectra which occur after brief intervals of sample heating are therefore due to changes in the CO layer rather than changes in the structure of the nickel surface. Structural effects will be investigated in future experiments by comparing the spectra of films evaporated at different sample temperatures and by extending our measurements to single crystal samples.

5. Thermally Activated Transitions

The energy diagrams in Fig. 17 are helpful in analyzing the distribution of molecules formed on the surface at different temperatures. Figure 17a shows an approximate form for the energy of an isolated carbon monoxide molecule as a function of the distance from the surface as it approaches a linear bonding site X_L, a bridge site X_B, and an intermediate site X_I located between the linear and bridge positions. The well depth determines the strength of the chemical bond and is approximately 1 eV for the most stable sites.[92] The bond energy as a function of position parallel to the surface is shown in Fig. 17b.

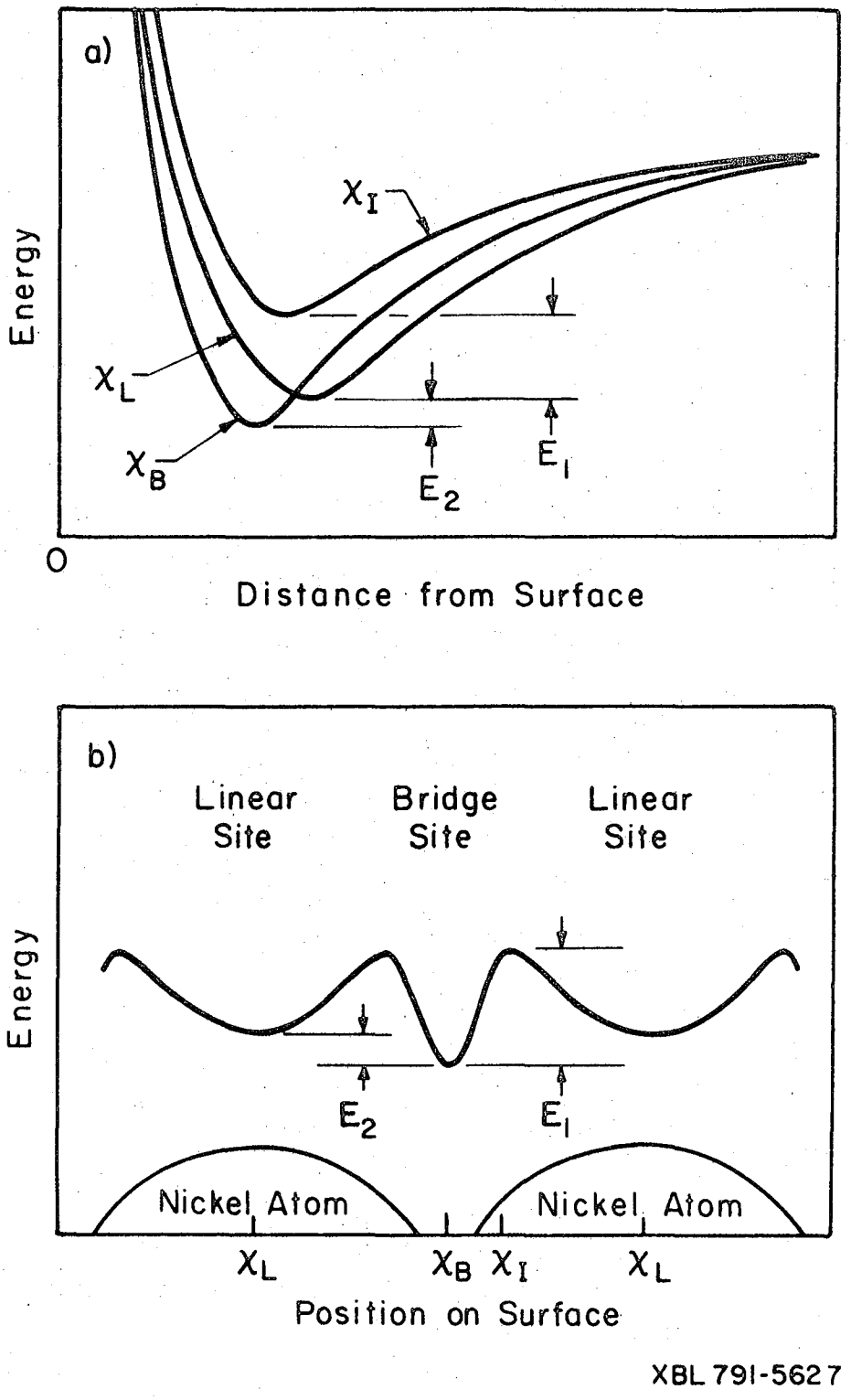

Fig. 17. Qualitative bonding energy of a CO molecule as a function of (a) distance from nickel surface, (b) position on surface.

Energy minima at the linear and bridge positions explain the tendency of molecules to be localized at sites of high symmetry rather than at random positions on the surface. If the energy minimum at the bridge site is approximately 0.02 eV below that of the linear site, then both sites will be populated at room temperature while bridge bonds will be favored on a cooled sample. This is the behavior detected in ELS for Ni(100).[77]

If we assume a small surface coverage so that there is no interaction between molecules, then in thermal equilibrium at a temperature T the ratio of the populations in the energy wells at the linear and bridge sites is proportional to the Boltzman factor $e^{-E_2/kT}$, where E_2 is the difference between the adsorption energies at the two sites. An equilibrium distribution is achieved only if the molecules possess sufficient thermal energy to overcome the energy barrier E_1 and switch to a neighboring adsorption site. An approximate transition rate for such a process is given by the equation

$$R = \nu_R \, e^{-E_1/kT} \tag{20}$$

where ν_R is the vibrational frequency for motion of the molecule parallel to the surface.

The first explanation which we propose for the high intensity of line A in spectra (e) through (g) is that for gas exposures made well below room temperature, molecules remain bonded at the site where they are first adsorbed and cannot switch positions to achieve a thermal equilibrium state. In Fig. 17b a broader energy well has been drawn for the linear site to suggest that linear bonds are more likely to

be formed when a molecule strikes the surface. An approximate value for E_1 can be found by noting in Table 4 that 10 per cent of the linear bonds detected in spectrum (f) converted to bridge bonds when the sample was heated to 170 K for 60 seconds to produce spectrum (e). Using $\nu_R = 10^{13}$ Hz, R = 0.0016 sec, and T = 170 K in Eq. (20), we find E_1 = 0.54 eV which is about half the measured adsorption energy. This energy barrier permits virtually no bond conversions to occur at 77 K, the temperature at which the gas exposure for spectrum (f) was made. Spectra (a) through (d) were all measured after heating the samples to 270 K or higher. These temperatures are sufficient to achieve a rapid equilibrium state for a barrier height of 0.54 eV. The approximately equal intensities measured for lines A and B in these spectra are consistent with an energy difference E_2 in Fig. 17 of only a few hundredths of an electron volt.

6. Intermolecular Repulsion

In our high coverage spectra the average spacing between molecules on the surface is comparable to the 3 Å molecular diameter determined from gas phase measurements.[65] Intermolecular repulsion limits the surface coverage on these samples and must be included in our analysis of the relative populations on linear and bridge sites. We first argue that interactions between molecules can change the relative strengths of the different chemical bonds formed with the nickel surface. This effect may explain the shift toward linear bonding sites at high coverage. Then we consider the direct repulsive forces which can force molecules out of the energy wells pictured in Fig. 17b and onto

lattice sites intermediate between the linear and bridge positions.

According to the accepted picture of CO chemisorption,[75] electrons donated by the metallic substrate into the antibonding π^* orbitals of the molecule serve to strengthen the Ni-C bond, weaken the C-O bond, and lower the C-O stretching frequency. Molecules bonded at three center sites must have the highest density of π^* electrons since their vibrational frequencies are farthest from those of the free molecule. Molecules at linear sites have the smallest π^* density. Electrons in π^* orbitals are concentrated away from the molecular axis and experience the strongest coulomb interaction with electrons of neighboring molecules. At high coverages the repulsive coulomb interaction may force these electrons back into the metal. This has been proposed as one reason for the continuous shifts to higher frequencies observed for each spectral line as the surface coverage increases.[64] Coulomb repulsion should also raise the energy of the bridge bonds relative to linear bonds and lead to a continuous increase in the equilibrium population of linear sites as more molecules are adsorbed. Such changes will be most evident in our spectra if molecules are able to freely convert from one bonding configuration to another at 77 K. This requires an energy barrier E_1 in Fig. 17 which is less than about 0.2 eV.

For sufficiently large surface coverages the direct repulsive forces between nearest neighbors become comparable to the lateral forces exerted by the nickel lattice. To minimize their energy, the molecules tend to form a close-packed hexagonal array[80,91] with a lattice constant which is larger than the 2.49 Å nearest neighbor

distance of the nickel atoms. Distortions in the CO array must take place to localize the molecules on linear and bridge sites and give the distinct lines observed in vibrational spectra. The forces causing these distortions are determined from the shape of the energy curve of Fig. 17b. Molecules will be displaced toward either a linear or a bridge site to form bonds which are stretched and distorted versions of the bonds formed at low coverage. Distorted linear bonds may produce the low frequency tail of line A observed in spectra (e) and (f). The broader energy well shown in Fig. 17b for the linear site means that more molecules in the close-packed array will form linear bonds than bridge bonds. The width of the potential energy well may be a more important factor favoring linear bonds at high coverage than their low density of π^* electrons.

As additional molecules are adsorbed, coulomb repulsion grows stronger and it becomes more difficult to distort the CO lattice. We then expect less localization of the CO molecules on the linear and bridge sites of the nickel lattice. Spectrum (g) of Fig. 16 illustrates this case. Seventy per cent of the total carbon monoxide signal appears in a broad absorption band between 1850 and 2150 cm^{-1}. Evidently the molecules causing this absorption occupy a continuous range of adsorption sites. Molecules are held on the less stable sites of intermediate bond character by strong repulsive forces from their nearest neighbors. The high surface coverage necessary to see this effect was achieved by exposing a clean surface to carbon monoxide gas at 2 K and then warming the sample to 29.3 K to induce ordering and

to remove molecules physically adsorbed on top of the chemisorbed layer. The peaks labeled P are due to the remaining physisorbed molecules and are discussed in Section B of this chapter. The strength and sharpness of line A in spectrum (g) is evidence that molecules do not have to be localized exactly over a nickel atom to form a linear bond. A tipping of the C-O axis might accompany the lateral displacement of the molecule to preserve the linear character of the Ni-C-O species.

We have argued that the large number of linear bonds detected in our high coverage spectra may be due to the formation at low temperatures of nonequilibrium surface states or to the effects of repulsive interactions between molecules. Evidence from other experiments favors the explanation in terms of intermolecular repulsion. First, Tracy's LEED measurements[80] indicate that the energy barriers are small for surface diffusion of CO molecules on Ni(100) and that thermal equilibrium can be achieved at sample temperatures as low as 77 K. Second is the fact that infrared experiments[64] on Pd(111) show that CO molecules switch from three center to two center adsorption sites at relatively low surface coverages. This transition occurs on a room temperature sample in equilibrium with gas phase molecules and is clearly caused by the interactions between adsorbed molecules. The changes in the spectrum which we observe at higher coverages seem to be the second step in the conversion from three center to linear bonds which occurs on (111) faces as molecules are packed together more closely.

To obtain quantitative information on the strengths of the various forces and the shapes of the energy curves in Fig. 17b, additional

measurements must be made in which the sample temperature and surface coverage are varied independently of each other. For example, we can eliminate the effects of intermolecular repulsion by studying the temperature dependence of low coverage states. The initial spectrum obtained after a gas exposure at 2 K determines the relative cross sections for the formation of each type of bond, and this gives the widths of the energy wells. The energy barriers for bond conversion can be calculated from the intensity shifts observed after heating this sample to a series of higher temperatures. The equilibrium populations reached at a given temperature determine the relative well depths. The effects of interactions between molecules can be studied by repeating this series of measurements and starting each sequence with a higher CO coverage. Our apparatus is ideal for these measurements because of its ability to vary the sample temperature precisely and to preserve nonequilibrium chemical states at low temperature during spectral measurements.

7. Intensities and Line Shifts

Finally we compare the line strengths and frequency shifts observed in Fig. 16 with the predictions of the dipole model developed in Chapter II. There we found that the absorption signal saturates at high coverages due to the screening effects of neighboring molecules. Therefore it cannot be used as a linear measure of surface coverage. In spectrum (d) the measured value of the integrated absorption strength is 1.6 cm^{-1} and the coverage should be approximately 1.1 x $10^{15}/cm^2$, the maximum attainable for a room temperature gas exposure.[92] Using

the dipole parameters of a free CO molecule and a linewidth of 30 cm^{-1}, the calculated integrated absorption strength for molecules arranged in a square array on the surface is 0.50 cm^{-1}. The measured infrared absorption by chemisorbed molecules is enhanced by a factor of approximately three relative to that of the free molecules. No such enhancement is observed in our experiments on physisorbed CO. To explain the observed line intensities we must assume that the molecular wave functions are modified by chemisorption such that the matrix element for the transition or the effective dipole charge q in Eq. (1) is increased. A bridge bonded molecule, whose vibrational frequency lies farthest from that of the free molecule, is more strongly perturbed by chemisorption than a molecule on a linear site and probably has a larger value of q. This may explain why the integrated strength in spectrum (d), which shows a larger number of bridge bonds, is greater than in spectrum (f) even though the total surface coverage in (f) is higher.

Equation (10) shows that the dipole-dipole frequency shift depends upon the charge q and will be increased by the same factor as the absorption strength. Numerical calculations based upon the model of Chapter II predict a 45 cm^{-1} shift for a coverage of $1.1 \times 10^{15}/cm^2$ and a linewidth of 30 cm^{-1}. The shift observed between spectra (a) and (d) is 50 cm^{-1} for line B and 55 cm^{-1} for line A. Precise agreement is not expected since the relative populations on linear and bridge sites and their arrangement on the surface are uncertain and because other mechanisms can contribute to the measured shifts.[47,64,75] It

is clear however that dipole-dipole coupling accounts for a major fraction of the observed effect. The same conclusion was reached for CO on Pt(111) based upon the spectra of different isotopic mixtures of CO.[46]

B. Physically Adsorbed Carbon Monoxide

Physical adsorption is the result of the attractive van der Waals interaction between atoms and molecules.[93] The weak dipole electric fields which produce these bonds have little effect on the molecular wave functions, and vibrational frequencies occur very close to those of the free molecule. In a series of experiments we have used the high sensitivity and spectral resolution, and the precise temperature control of our apparatus to investigate the different states of physically adsorbed carbon monoxide in both monolayer and multilayer films. The procedures of Section V-A-1 were followed in preparing a clean metal film covered with a layer of chemisorbed CO. This provided a homogeneous, chemically inert substrate on which physical adsorption could be studied. The first layer of physisorbed molecules is found to consist of molecules bound to the substrate in several configurations. Successive layers form a crystal lattice whose structure appears to change when the sample is annealed at approximately 22 K.

1. Monolayer Films

Figure 18 shows three spectra of a nickel film evaporated and initially exposed to 5×10^{-6} Torr of CO at 300 K and then exposed to a total flux of 1.9×10^{15} CO molecules/cm^2 at 2 K. The strong absorption line at 2142.5 cm^{-1} in the initial spectrum (T = 2 K) splits

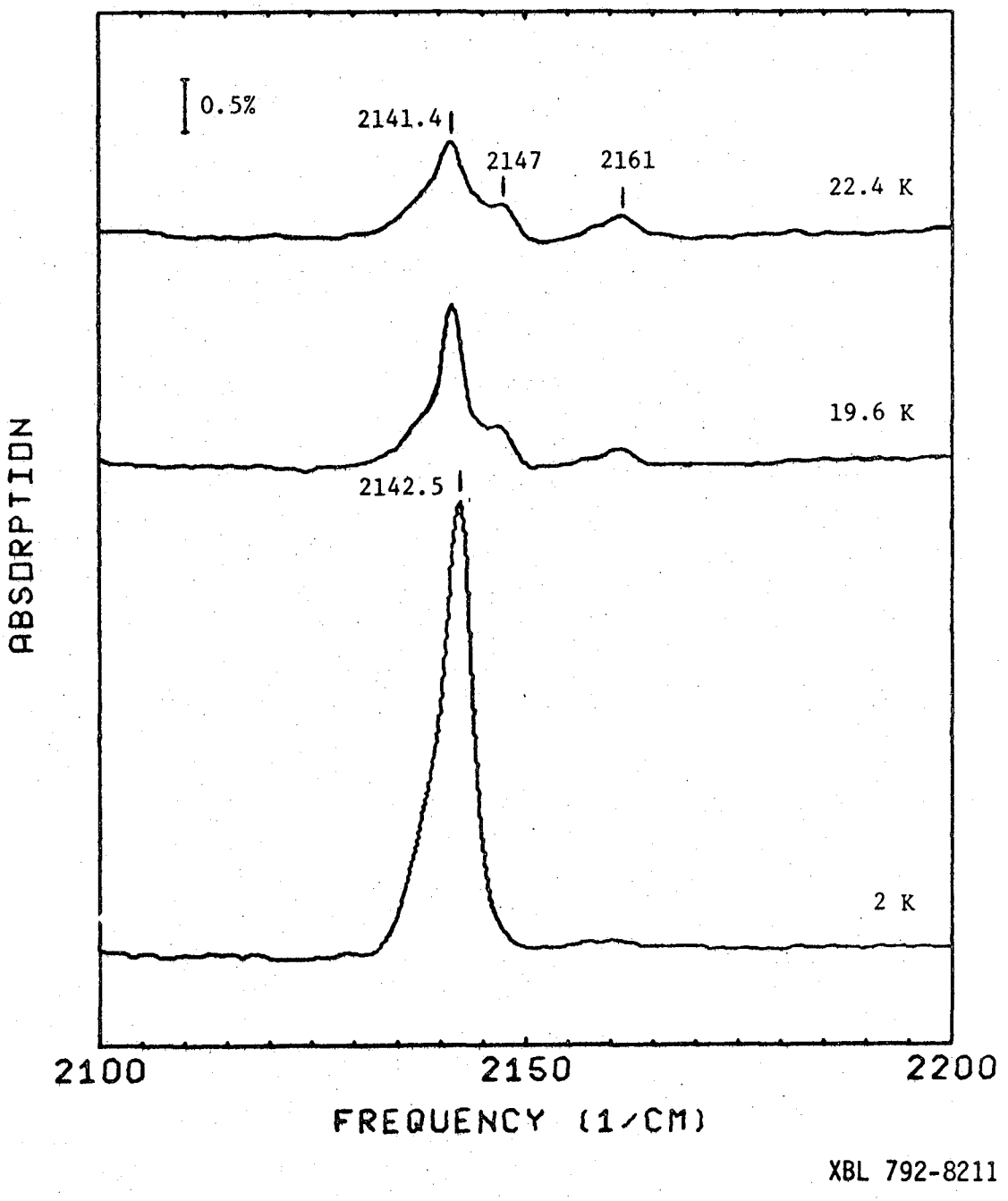

Fig. 18. Spectra of a thin layer of CO physically adsorbed at 2 K and then heated to 19.6 K and 22.4 K.

into three weaker lines after heating the sample to 19.6 K and 22.4 K for one minute intervals. Approximately 2.5 monolayers of physically adsorbed CO are formed during the low temperature exposure if all the incident molecules stick to the cold surface. The concentration of molecules in a monolayer is taken as $7.6 \times 10^{14}/cm^2$ which is the two thirds power of the measured volume density of $2.2 \times 10^{22}/cm^3$ for solid CO.

The absorption lines in Fig. 18 are shifted from the frequency of the unperturbed C-O vibration due to the weak interactions between the adsorbed molecules. Negative frequency shifts of 4 to 5 cm^{-1} have been observed for CO diluted in solid N_2, Ar, and CH_4.[94] This solvent shift does not depend strongly on the nature of the host lattice. Molecules with the same vibrational frequency are coupled by the dipole-dipole interaction which produces positive frequency shifts. In Chapter II it was shown that the magnitude of this shift is approximately 2.5 cm^{-1} for the molecules vibrating perpendicular to the surface. The net effect of the solvent shift and the dipole shift is to produce the absorption line at 2142.5 cm^{-1} for T = 2 K and at 2141.4 cm^{-1} for T = 22.4 K in Fig. 18. Because this line is the first to decrease in intensity when the sample is heated, we attribute it to the molecules in the second and third layers which are the first to desorb.

The physisorbed molecules which remain on the surface after heating to 22.4 K have several distinct absorption lines and must be bonded in different configurations to the layer of chemisorbed molecules which covers the nickel surface. The vibrational frequency may depend upon

whether the carbon or the oxygen atom of the CO molecule is nearest the surface. Another possibility, suggested by the spectra of chemisorbed molecules, is that linear and bridge adsorption sites on the underlying CO lattice may produce the different vibrational frequencies. The large frequency shifts associated with the lines at 2147 and 2162 cm^{-1} indicate that the surface bond may involve more than the simple van der Waals interaction. Larger positive frequency shifts have been observed for weakly bound carbon monoxide molecules adsorbed at room temperature on a variety of catalyst samples.[8] A chemical interaction involving the transfer of electrons from the CO molecule to the substrate has been proposed as the reason for these frequency shifts,[8,95] and this may also explain the additional lines seen in our spectra.

2. Multilayer Films

Figure 19 shows the spectra of a multilayer carbon monoxide film. A helium temperature nickel film sample was first heated to 300 K and cleaned by argon ion bombardment. Then it was cooled to 2 K and dosed with 1.5×10^{16} CO molecules/cm^2 producing a first layer of chemisorbed molecules plus approximately 18 layers of physisorbed molecules. The strong absorption at 2142 cm^{-1} first decreased in intensity and split into two components as the sample was heated to successively higher temperatures for two minute intervals. The weaker line at 2138 cm^{-1} maintained a nearly constant intensity. Further heating to 24.0 K caused the strong absorption to reappear and the spectrum resembles the one measured after the initial gas exposures. The final spectrum, obtained after heating to 29.3 K, shows that most of the physically

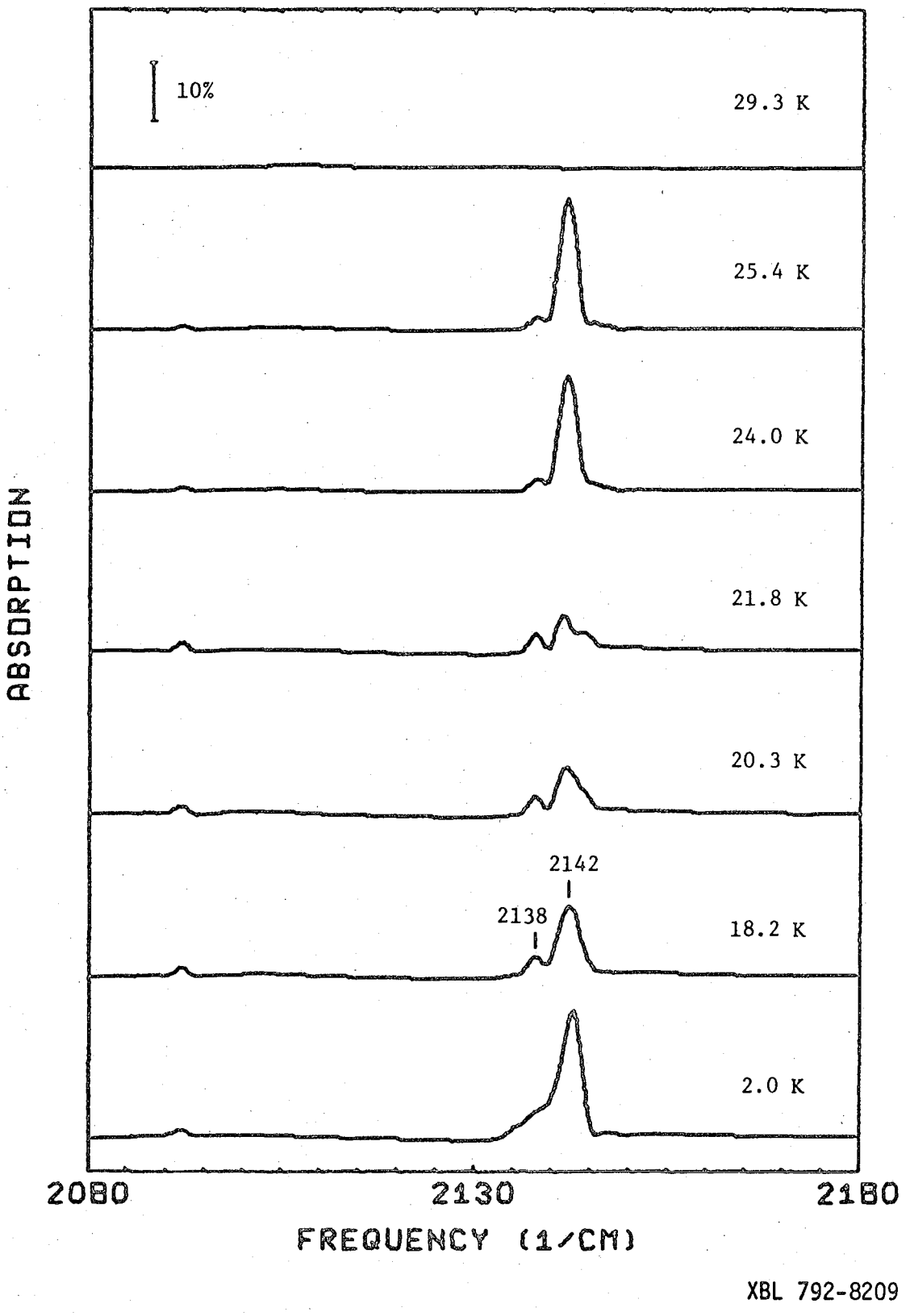

Fig. 19. Spectra of multilayer physically adsorbed CO film heated to successively higher temperatures.

adsorbed molecules have evaporated from the surface. This spectrum appears magnified in Fig. 16g where the absorptions due to the chemisorbed molecules are visible between 1850 and 2150 cm^{-1}. The remaining physisorbed molecules cause the lines labeled P in Fig. 16g. The line shapes differ from those of Fig. 18 because of the presence of a sharp absorption line at 2142 cm^{-1} in the spectrum of the radiation incident on the sample. Some of this radiation reflects off of the optical baffles (Fig. 9) before hitting the sample. Carbon monoxide molecules condensed on these baffles during the low temperature gas exposure absorb radiation at 2142 cm^{-1} and cause a sharp negative feature in the measured spectrum. This effect is not visible in Fig. 18 because a samller gas exposure was made in that experiment.

Figure 20 shows the spectrum of a different multilayer carbon monoxide film with a different thermal history. The three lines of the main absorption occur at 2137.8, 2141.3, and 2144.3 cm^{-1} and are more clearly resolved than in Fig. 19. For this sample a nickel evaporation and CO gas exposure of 5×10^{-6} torr were first made at 300 K. The surface was then dosed with 4.6×10^{16} CO molecules/cm^2 at 2 K and heated to 22.8 K for one minute. The strong line at 2092 cm^{-1}, which also appears in Fig. 19, and the weaker ones at 2088 and 2112 cm^{-1} arise from the CO isotopes $C^{13}O^{16}$, $C^{12}O^{18}$, and $C^{12}O^{17}$. The broad feature centered at 2200 cm^{-1} is caused by the simultaneous excitation of the CO stretching vibration and the various low frequency phonon modes of the crystal lattice. The dip in the absorption signal just below the frequency of the main CO resonance represents a decrease

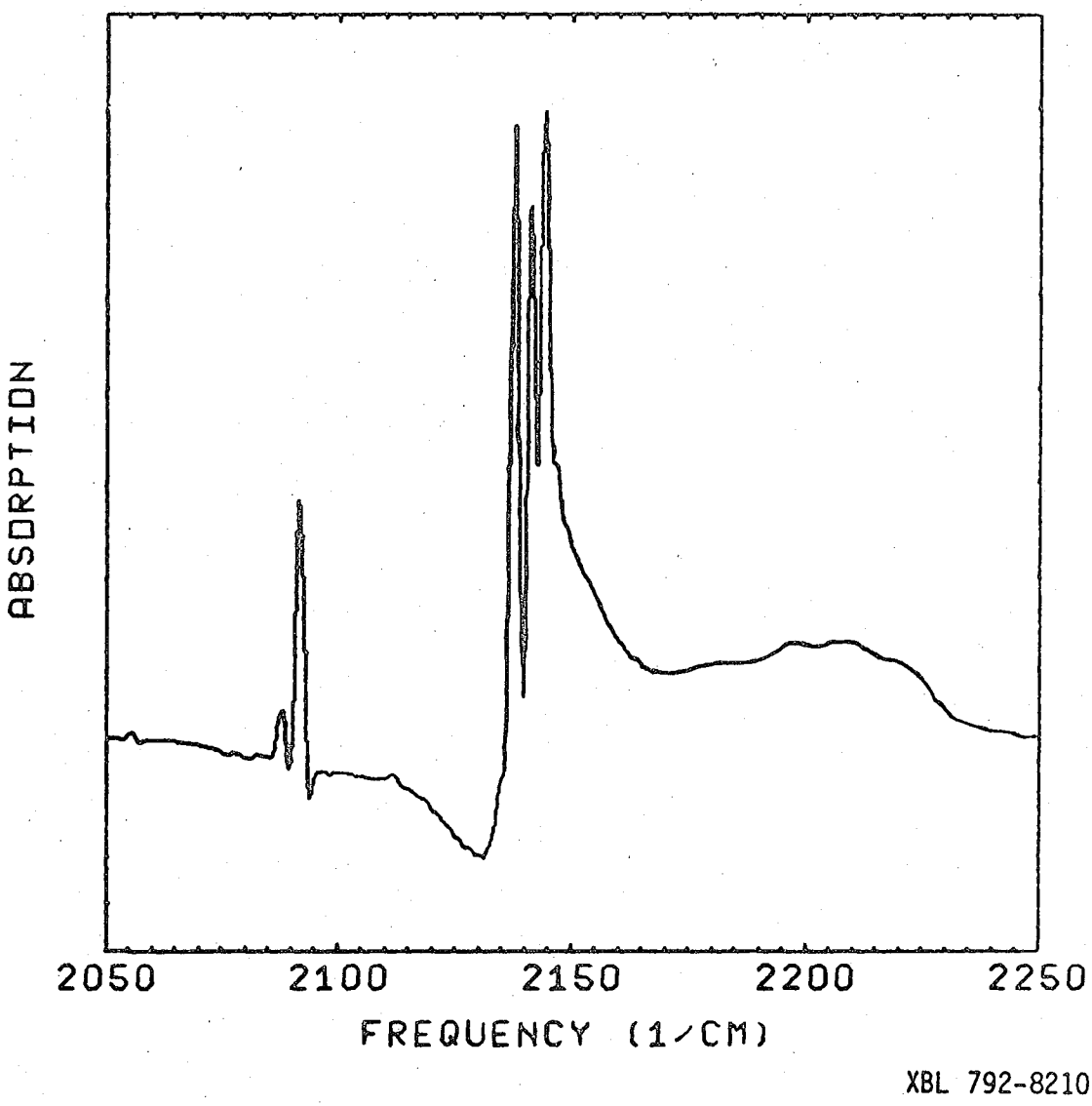

Fig. 20. Magnified spectrum of a multilayer CO film.

in the background absorption by the metal film. It is caused by the increased dielectric reflection from the carbon monoxide film as its resonant frequency is approached from below. Both the isotope and phonon modes have been observed previously in the transmission spectra of much thicker films.[48,94] The multiple line structure of the main resonance has not been seen before.

Of the four multilayer CO films which we studied, all showed the initial strong absorption at 2142 cm^{-1} with a weaker feature at 2138 cm^{-1} which sharpens after heating the sample. Only two of the CO films converted to the state with three weak absorptions. Only the film whose spectra appear in Fig. 19 converted back from the three peak state to the two peak state. Among the factors which could explain the variability of our results are differences in the sample temperatures, heating and cooling rates, the impurity content of the film, and the surface structure of the substrate.

Carbon monoxide crystallizes in an fcc lattice with four inequivalent molecules per cubic cell[96] and four modes of coupled molecular vibration. Fox and Hexter[97] show that the three modes which are optically active have the same frequency and an isotropic polarizability. We can therefore calculate the absorption spectrum using the isotropic dielectric constant of Eq. (6) and the Lorentz local field correction which is valid for a cubic crystal. Figure 21 shows the calculated frequency dependence of the absorption signal assuming a resonant frequency of 2143 cm^{-1} and linewidths ranging from 5.0 to 0.02 cm^{-1}. The film thickness of 18 layers, the angle of incidence

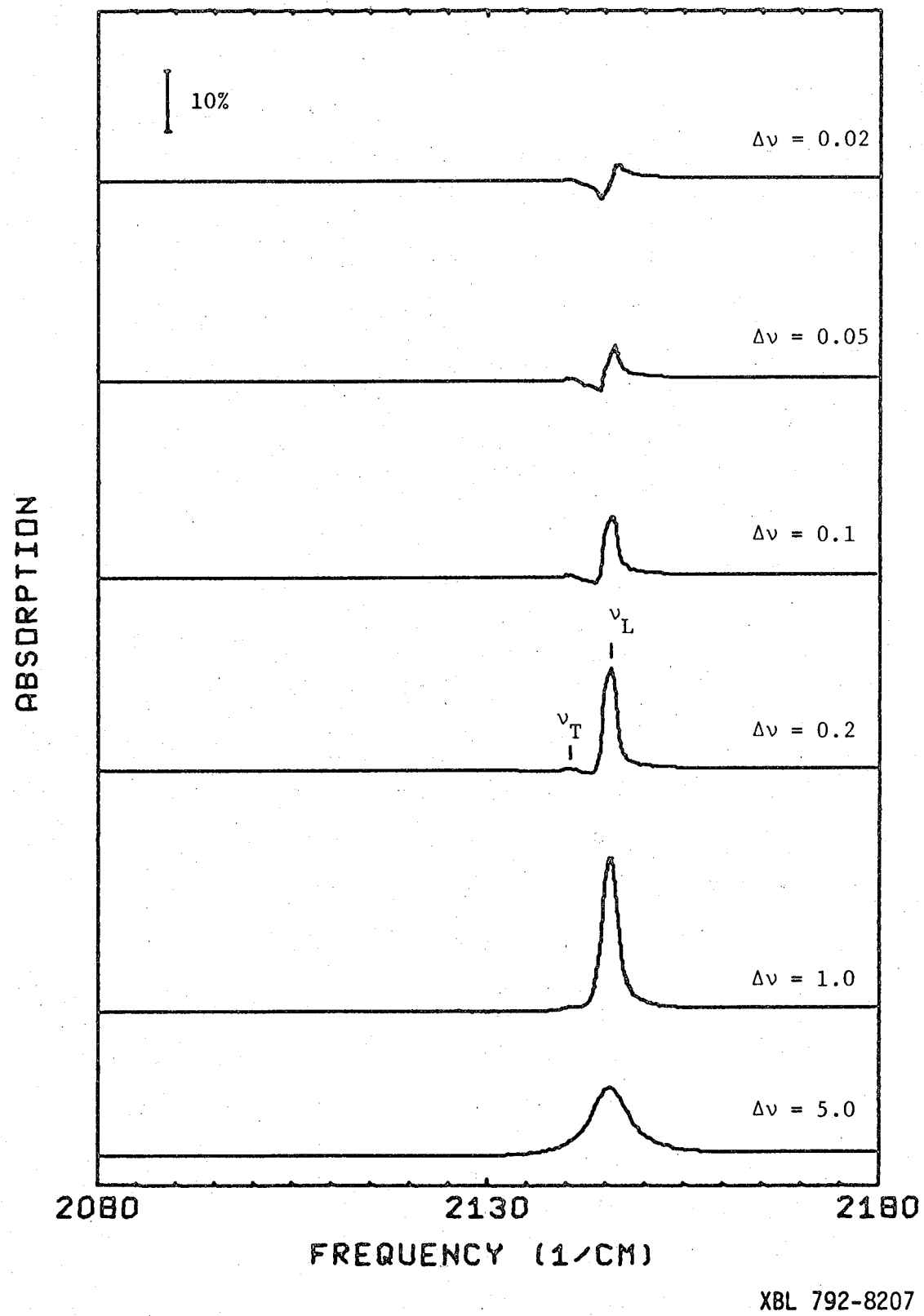

Fig. 21. Calculated spectra of multilayer CO films assuming different linewidths.

of 82°, and the optical constants of cold nickel taken from Table 1 were used to model as closely as possible the optical response of the sample whose measured spectra appear in Fig. 19. The calculated signal at each frequency is averaged over a 2 cm^{-1} band to simulate the effect of the finite resolution of the infrared spectrometer. The horizontal and vertical scales are the same in Fig. 19 and Fig. 21 to facilitate comparison.

The calculated absorption signal decreases in intensity as the width of the molecular resonance changes from 0.2 to 0.02 cm^{-1}. The reason is that for small linewidths the peak polarizability from Eq. (1) is so large that nearly all of the incident power polarized parallel to the plane of incidence is absorbed. Since the peak absorption has reached the saturation level and is independent of linewidth, the total absorbed power and the peak power at 2 cm^{-1} resolution must both increase with linewidth. By comparing the line strengths in the calculated and measured spectra, we conclude that disorder in the initial deposit of carbon monoxide produces an infrared linewidth of approximately 3 cm^{-1}. Annealing the film can improve the lattice order and reduce the linewidth to approximately 0.1 cm^{-1}. Heating the film to too high a temperature or perhaps cooling it too quickly is sufficient to restore the original disordered state.

The intense absorption at frequency ν_L = 2146 cm^{-1} in Fig. 21 is caused by oscillating dipoles oriented perpendicular to the plane of the film. The positive frequency shift from 2143 cm^{-1} is the same dipole shift encountered in the spectra of monolayer films. Dipoles

oriented parallel to the film produce an absorption at ν_T = 2140.5 cm^{-1} which is much weaker because at a metal surface the electric field components with this polarization are very small. The absorptions at ν_T and ν_L occur at the frequencies of the transverse optical (TO) and longitudinal optical (LO) phonon modes of the carbon monoxide lattice. Berreman's experiments on room temperature LiF films were the first to demonstrate that infrared absorptions can occur at both phonon frequencies.[98]

The peak absorptions in the calculated spectra appear approximately 4 cm^{-1} above the measured values in Fig. 19 because we did not include the solvent shift in our theoretical model. The measured splitting between ν_T and ν_L for the sample heated to 24.0 K is 4.1 cm^{-1} while the calculated value is 5.5 cm^{-1} for $\Delta\nu$ = 0.2 cm^{-1}. The agreement between the shapes of these two spectra would be better if a weak feature with a 5 cm^{-1} bandwidth were added to the calculated spectrum to account for residual disorder and surface effects.

The 3 cm^{-1} splitting of the LO absorption shown in Fig. 19 at T = 21.8 K and in Fig. 20 is inconsistent with our calculations. It suggests that, along with the narrowing of the spectral lines, there is a transition to a more complicated crystal structure. This could be either a cubic lattice with more than one set of TO and LO phonon modes or a noncubic lattice whose infrared spectrum would depend upon the orientation of the crystal axes relative to the plane of the film. Heat capacity[99] and x-ray diffraction measurements[96] show that solid carbon monoxide undergoes a phase transition from an fcc to an hcp

lattice structure when it is heated above 61.6 K. The infrared linewidth broadens from 1.5 to 14 cm^{-1} when this transition occurs.[25] Our spectra provide the only evidence of a second stable low temperature phase, and we can only speculate about its nature. Entropy measurements reveal that there is some residual disorder in the usual low temperature phase.[99] The magnitude of this effect suggests that the lattice does not distinguish between the carbon and oxygen atoms of the CO molecule and that the static dipole moment at each site may assume either of two allowed orientations with equal probability. There may exist another crystal structure in which these dipole moments form an ordered array. This could explain both the narrower linewidths and the additional splittings observed in some of our spectra.

3. Activation Energies

Our analysis of the chemisorption data in Section V-A-5 demonstrated that activation energies for various processes can be estimated by noting the temperatures at which they occur. A temperature of 27 K and a phonon frequency ν_R = 50 cm^{-1} in Eq. (20) yield an activation energy for desorption of the physically adsorbed molecules of 0.068 eV. This is consistent with the published value of 0.061 eV/molecule for the heat of vaporization.[100] A more interesting process is the conversion of physically adsorbed molecules to the more stable chemically adsorbed state. Magnified plots of the data in Fig. 19 (as shown in Fig. 16g) show a line at 2100 cm^{-1} from chemisorbed carbon monoxide even in the spectrum measured immediately after the initial gas exposure at 2 K. This means that no activation energy in excess of the kinetic

energy of the incident molecule is required to form a chemical bond with the nickel surface. The intensity of this 2100 cm^{-1} line grew by about 50 per cent in the final stages of sample heating as some of the physisorbed molecules converted to the chemisorbed state. The activation energy for this process is therefore comparable to the desorption energy. It is probably a measure of the repulsion by the chemisorbed molecules already present on the surface. This repulsion prevents physically adsorbed molecules from approaching nickel atoms and forming chemical bonds.

VI CONCLUSIONS

We have demonstrated that sensitive vibrational spectra of molecules adsorbed on metal surfaces can be measured by attaching a thermometer to the sample, cooling the assembly to liquid helium temperatures, and recording the temperature changes which occur when infrared radiation is absorbed. The sensitivity of our system is attributable to the low noise and reduced background signal achieved in the thermal detection scheme, to the ability of the rapid scan Fourier transform spectrometer to discriminate against low frequency noise and drift, and to the automated, computerized data acquisition electronics.

The data presented in Chapter V resulted from a series of exploratory measurements made in a few weeks when all the components of the apparatus first began to work at once. The spectra of chemisorbed molecules on evaporated nickel films give strong support for the picture of linear and bridge adsorption sites and show how the distribution of molecules among these sites changes when the coverage increases, and intermolecular forces become important. The spectra of physically adsorbed monolayers show three distinct bonding configurations while those of multilayer CO films give evidence of a new low temperature crystal phase with very narrow absorption lines. These measurements demonstrate that surface states formed over a broad range of temperatures can be studied in our helium temperature apparatus and that precise control over the temperature is useful in measuring activation energies for chemical changes.

The promise of our apparatus is its potential for detecting infrared absorptions smaller than one part in 10^4 of the incident radiation. This is the noise limit of our present system and is better than that of the best published reflection experiments. We have analyzed in detail in Chapters II and IV the theoretical and experimental aspects of our system which are important in optimizing its performance. We conclude that improvements in the optics, electronics, and thermometers may lead to 10 times better sensitivity. These performance levels can be achieved for single crystal samples as well as evaporated films and for infrared frequencies below 1000 cm^{-1} where measurements with other techniques have been difficult. With improved sensitivity it will be possible to make detailed studies of molecules other than carbon monoxide and to look for evidence of chemical reactions between different adsorbed molecules.

ACKNOWLEDGEMENTS

I would like to thank my thesis advisor, Prof. Paul L. Richards, for thinking up this experiment and for being encouraging and patient as it slowly progressed. Thanks are also due to a long list of students and staff members at Berkeley. Their advice and assistance contributed to the success of this research, and their friendship made it enjoyable.

This work was done under the auspices of the Division of Materials Science, Office of Basic Energy Sciences, Dept. of Energy.

REFERENCES

1. H. Ibach, H. Hopster, and B. Sexton, Appl. Surf. Sci. 1, 1 (1977).

2. J. Pritchard and T. Catterick, in Experimental Methods in Catalytic Research, Vol. III, R. B. Anderson and P. T. Dawson, ed. (Academic Press 1976) Chapter 7.

3. J. Pritchard, in Modern Methods of Surface Analysis, Dechema Monographs, Vol. 78 (Dechema, Frankfurt 1975) p. 231.

4. K. Horn and J. Pritchard, Surf. Sci. 52, 437 (1975).

5. F. M. Hoffman and A. M. Bradshaw, in Proc. 3rd Intern. Conf. on Solid Surfaces (Vienna, 1977) p. 1167.

6. R. Gomer, ed., Interactions on Metal Surfaces (Springer, 1975). H. Ibach, ed., Electron Spectroscopy for Surface Analysis (Springer, 1977). G. A. Somorjai, Principles of Surface Chemistry (Prentice-Hall, 1972).

7. R. P. Eischens, S. A. Francis, and W. A. Plisken, J. Phys. Chem. 60, 194 (1956). R. P. Eischens and W. A. Pliskin, Adv. Catalysis 10, 1 (1958).

8. M. L. Hair, Infrared Spectroscopy in Surface Chemistry (Dekker, 1967). L. H. Little, Infrared Spectra of Adsorbed Species (Academic Press, 1966). L. H. Little, in Chemisorption and Reactions on Metal Films (Academic Press, 1971) p. 490.

9. H. G. Tompkins and R. G. Greenler, Surf. Sci. 28, 194 (1971).

10. I. Ratajczykowa, Surf. Sci. 48, 549 (1975). R. A. Shigeishi and D. A. King, Surf. Sci. 62, 379 (1977).

11. A. A. Lucas and S. Sunjic, in Progress in Surface Science, Vol. 2 (Pergamon, 1972) p. 75. E. Evans and D. L. Mills, Phys. Rev. B5, 4126 (1972).

12. H. Ibach, Surf. Sci. 66, 56 (1977).

13. J. E. Demuth, H. Ibach, and S. Lehwald, Phys. Rev. Lett. 40, 1044 (1978).

14. H. H. Madden, J. Vac. Sci. Technol. 13, 228 (1976).

15. R. W. Stobie, B. Rao, and M. J. Dignam, Surf. Sci. 56, 334 (1976).

16. A. J. McQuillan, P. J. Hendra, and M. Fleischman, J. Electroanal. Che. 65, 933 (1975). S. Efrima and H. Metiu, J. Chem. Phys. (to be published).

17. M. J. Adams, B. C. Beadle, G. F. Kirkbright, and K. R. Menon, Appl. Spect. 32, 430 (1978).

18. K. Bhasin, D. Bryan, R. W. Alexander, and R. J. Bell, J. Chem. Phys. 64, 5019 (1976).

19. D. A. Pinnow and T. C. Rich, Appl. Optics 12, 984 (1973).

20. R. C. Jones, J. Opt. Soc. Am. 43, 1 (1953). F. J. Low, J. Opt. Soc. Am. 51, 1300 (1961). F. J. Low and A. P. Hoffman, Appl. Optics 2, 649 (1963).

21. N. Nishioka, D. Woody, and P. L. Richards, Appl. Optics 17, 1562 (1978).

22. R. R. Joyce and P. L. Richards, Phys. Rev. Lett. 24, 1007 (1970).

23. R. G. Greenler, J. Chem. Phys. 44, 310 (1966).

24. J. D. E. McIntyre, in Optical Properties of Solids: New Developments, B. O. Seraphin, ed. (North Holland, 1976).

25. G. E. Ewing, J. Chem. Phys. 37, 2250 (1962).

26. R. A. Toth, R. H. Hunt, and E. K. Plyler, J. Mol. Spect. 32, 85 (1969).

27. J. D. Jackson, Classical Electrodynamics (Wiley, 1962) p. 602.

28. M. Born and E. Wolfe, Principles of Optics, 4th ed. (Pergamon, 1970) p. 98.

29. C. Kittel, Introduction to Solid State Physics, 4th ed. (Wiley, 1971) p. 454.

30. J. H. de Boer, Adv. Catalysis 8, 118 (1956).

31. J. R. MacDonald and C. A. Barlow, J. Chem. Phys. 39, 412 (1963).

32. Reference 27, p. 112.

33. J. Topping, Proc. Roy. Soc. Lond. A114, 67 (1927).

34. D. V. Sivukhin, J. Exptl. Theoret. Phys. (USSR) 21, 367 (1951). D. V. Sivukhin, Soviet Phys. JETP 3, 269 (1956).

35. G. A. Bootsma and F. Meyer, Surf. Sci. 14, 52 (1969).

36. Reference 28, p. 625.

37. J. R. Beattie and G. K. T. Conn, Phil. Mag. 46, 989 (1955).

38. I. N. Shkliarevskii and V. G. Padalka, Opt. and Spect. 6, 45 (1959).

39. A. B. Pippard, in Advances in Electronic and Electron Physics, L. Marton, ed. (Academic Press, 1954) p. 1.

40. Reference 28, p. 611.

41. T. Holstein, Phys. Ref. 96, 535 (1954).

42. Reference 28, p. 62.

43. J. Pritchard and M. L. Sims, Trans. Faraday Soc. 66, 427 (1970).

44. R. A. Shigeishi and D. A. King, Surf. Sci. 58, 379 (1976).

45. J. T. Yates, R. G. Greenler, I. Ratajczykowa, and D. A. King, Surf. Sci. 36, 739 (1973).

46. A. Crossley and D. A. King, Surf. Sci. 68, 528 (1977).

47. M. Moskovits and J. E. Hulse, Surf. Sci. 78, 397 (1978).

48. G. E. Ewing and G. C. Pimentel, J. Chem. Phys. 35, 925 (1961).

49. S. Dushmand and J. M. Lafferty, Scientific Foundations of Vacuum Technique (Wiley, 1962) p. 90.

50. Ref. 49, p. 14.

51. R. Bakish and S. S. White, Handbook of Electron Beam Welding (Wiley, 1964).

52. F. Rosebury, Electron Tube and Vacuum Techniques, (Addison-Wesley, 1965) p. 3.

53. Reference 52, p. 68.

54. R. J. Bell, Introductory Fourier Transform Spectroscopy (Academic Press, 1972).

55. P. R. Griffiths, Chemical Infrared Fourier Transform Spectroscopy (Wiley, 1975).

56. D. H. Chenery and N. Sheppard, Appl. Spect. 32, 79 (1978).
D. R. Mattson, Appl. Spect. 32, 335 (1978).

57. P. R. Griffiths, H. J. Sloane, and R. W. Hannah, Appl. Spect. 31, 485 (1977).

58. Reference 29, p. 262.

59. NBS Circular 556, Thermal Conductivity of Metals and Alloys at Low Temperatures (1954) p. 20.

60. R. A. Smith, F. E. Jones, and R. P. Chasmar, The Detection and Measurement of Infrared Radiation (Oxford University Press, 1968) Chapter 5.

61. Instruction Manual, Model 185 Preamplifier (Princeton Applied Research, 1972) p. IV-5.

62. J. Kleefeld, B. Pratt and A. A. Hirsch, J. of Crystal Growth 19, 141 (1973).

63. H. E. Grenga, K. R. Lawless, and L. B. Garmon, J. Appl. Phys. 42, 3629 (1971).

64. A. M. Bradshaw and F. M. Hoffman, Surf. Sci. 72, 513 (1978).

65. J. Corner, Proc. Roy. Soc. Lond. A58, 737 (1946). E. A. Mason and W. E. Rice, J. Chem. Phys. 22, 843 (1954).

66. Reference 54, p. 157.

67. A. R. H. Cole, Tables of Wavenumbers for the Calibration of Infrared Spectrometers (Pergamon, 1977).

68. J. Pritchard, in Surface and Defect Properties of Solids, (Chemical Society, 1972) p. 222.

69. M. Primet, J. A. Dalmon, and G. A. Martin, J. of Catalysis 46, 25 (1977).

70. R. Van Hardeveld and F. Hartog, Adv. in Catalysis 22, 75 (1972).

71. C. E. O'Neill and D. J. C. Yates, J. Phys. Chem. 65, 901 (1961).

72. E. F. McCoy and R. St. C. Smart, Surf. Sci. 39, 109 (1973). H. C. Eckstrom, G. G. Possley, and S. E. Hannum, J. Chem. Phys. 52, 5435 (1970).

73. G. Apai, P. S. Wehner, R. S. Williams, J. Stöhr, and D. A. Shirley, Phys. Rev. Lett. 37, 1497 (1976). C. L. Allyn, T. Gustafsson, and E. W. Plummer, Chem. Phys. Lett. 47, 127 (1977).

74. J. E. Hulse and M. Moskovits, Surf. Sci. 57, 125 (1976).

75. G. Blyholder, J. Phys. Chem. 68, 2772 (1964).

76. W. Erley and H. Wagner, Surf. Sci. 74, 333 (1978).

77. S. Andersson, Solid State Commun. 21, 75 (1977).

78. G. Doyen and G. Ertl, Surf. Sci. 43, 197 (1974).

79. D. W. Bullett and M. L. Cohen, Solid State Commun. 21, 157 (1977).

80. J. C. Tracy, J. Chem. Phys. 56, 2736 (1972).

81. S. Andersson and J. B. Pendry, Surf. Sci. 71, 75 (1978).

82. J. C. Bertolini, G. Dalmai-Imelik, and J. Rousseau, Surf. Sci. 68, 539 (1977).

83. J. C. Campuzano and R. G. Greenler, J. Vac. Sci. Technol. 16, (1979).

84 M. Primet, J. M. Basset, M. V. Mathieu, and M. Prettre, J. Catalysis 29, 213 (1973).

85. T. L. Einstein and J. R. Schrieffer, Phys. Rev. B7, 3629 (1973). T. B. Grimley and f. Torrini, J. Phys. C 6, 868 (1973).

86. J. V. Sanders, in Chemisorption and Reactions on Metallic Films (Academic Press, 1971) p. 1.

87. R. Suhrman, R. Gerdes, and G. Wedler, Zeit. Naturforschung 18, 1212 (1963). R. W. Hoffman in Thin Films (American Society for Metals, 1964) p. 100.

88. S. R. Logan and C. Kembal, Trans. Far. Soc. 56, 144 (1960).

89. O. Beeck, A. E. Smith, A. Wheeler, Proc. Roy. Soc. Lond. A177, 62 (1940).

90. J. R. Anderson and B. G. Baker, J. Phys. Chem. 66, 482 (1962).

91. T. A. Clarke, I. D. Gay, and R. Mason, Surf. Sci 50, 137 (1975).

92. K. Christman, O. Schober, and G. Ertl, J. Chem. Phys. 60, 4719 (1974).

93. Reference 29, p. 700.

94. A. G. Maki, J. Chem. Phys. 35, 931 (1961).

95. R. A. Gardner and R. H. Petrucci, J. Am. Chem. Soc. 82, 5051 (1960).

96. R. W. G. Wyckoff, Crystal Structures, Vol. I (Wiley, 1963) p. 185.

97. D. Fox and R. M. Hexter, J. Chem. Phys. 41, 1125 (1964).

98. D. W. Berreman, Phys. Rev. 130, 2193 (1963).

99. J. Clayton and W. Giaque, J. Am. Chem. Soc. 54, 2610 (1932).

100. Natl. Bur. Standards Circ. No. 500.

TECHNICAL INFORMATION DEPARTMENT
LAWRENCE BERKELEY LABORATORY
UNIVERSITY OF CALIFORNIA
BERKELEY, CALIFORNIA 94720